学位論文

Theoretical Study on Nonlocal Effects in Resonant X-Ray Emission Spectra of Strongly-Correlated Systems

強相関電子系の共鳴X線発光スペクトルにおける非局所効果の理論的研究

平成11年12月 博士（理学）申請

東京大学大学院理学系研究科
物理学専攻

井手　剛

学位論文

Theoretical Study on Nonlocal Effects in Resonant X-Ray Emission Spectra of Strongly-Correlated Systems

強相関電子系の共鳴X線発光スペクトルにおける
非局所効果の理論的研究

平成11年12月 博士（理学）申請

東京大学大学院理学系研究科
物理学専攻

井手 剛

Thesis

Theoretical Study on Nonlocal Effects in Resonant X-Ray Emission Spectra of Strongly-Correlated Systems

Department of Physics, Faculty of Science,
The University of Tokyo

December, 1999

IDÉ Tsuyoshi

Contents

1 General Introduction 1
- 1.1 Historical Survey on High-Energy Spectroscopies . . . 1
- 1.2 Resonant Scattering . . . 13
- 1.3 Some Aspects on Spectral Functions . . . 20
- 1.4 Model Hamiltonians and Their Implications . . . 26
- 1.5 Exact Diagonalization Techniques . . . 32
- 1.6 Scope . . . 35

2 A Model Study on Cluster Size Effects of Resonant X-Ray Emission Spectra 37
- 2.1 Introduction . . . 37
- 2.2 Formulation . . . 39
- 2.3 Calculated Results . . . 42
- 2.4 Discussion . . . 45
- 2.5 Conclusions . . . 52

3 Interplay between Raman and Fluorescence-Like Components in Degenerate d^0 and d^1 Systems 56
- 3.1 Introduction . . . 56
- 3.2 Formulation . . . 59
- 3.3 Calculated Results I: Band Insulators . . . 62
- 3.4 Calculated Results II: Mott-Hubbard Insulators . . . 68
- 3.5 Discussion . . . 78
- 3.6 Conclusions . . . 80

4 Local and Nonlocal Excitations in Cu $4p$-$1s$ Resonant X-Ray Emission Spectra of Nd_2CuO_4 82
- 4.1 Introduction . . . 82
- 4.2 Formulation . . . 84
- 4.3 Analysis with Impurity Anderson Model . . . 89

4.4 Analysis with Multi-Cu Models 95
4.5 Conclusions 102

5 Polarization and Momentum Dependence of Charge Transfer Excitations in Nd_2CuO_4 103
5.1 Introduction 103
5.2 Formulation 105
5.3 Polarization Dependence 107
5.4 Incident Energy Dependence 113
5.5 Momentum Transfer Dependence 117
5.6 Conclusions 119

6 Concluding Remarks 120

Chapter 1

General Introduction

In this chapter, a brief survey is given of the ideas that lie at the basis of the other chapters in this thesis. We first explain the historical background of this study. Next we derive scattering cross section of second order optical process, and explain its general properties. Model Hamiltonians, the Zhang-Rice singlet, core excitons and numerical techniques are sketched in the rest of this chapter. We finally summarize our motivation of this thesis.

1.1 Historical Survey on High-Energy Spectroscopies

1.1.1 Core-level spectroscopies

The idea of investigation into the microscopic world by using a light as a probe had existed before the birth of quantum mechanics. In fact, the Schrödinger equation in the differential form, or the Heisenberg equation in the matrix form was acknowledged as the basic equation by reproducing the experimentally observed optical spectra such as the Balmer series of hydrogen [1]. The discovery of the spin degrees of freedom is also associated with spectroscopic experimental facts such as the Zeeman effect or the Pashen-Back effect [2]. In this sense, spectroscopies were a cradle of the quantum mechanics. Atomic theory of spectroscopy had been completed before the end of the World War II by the famous papers by Slater [3], and by Racah [4], all of which were accidentally titled "theory of complex spectra". It was Racah who introduced the idea of a spherical tensor. In those papers, they classified eigenstates of an atom containing many electrons according to SO(3) group, and clarified its selection rule in an optical transition. Since deep enough core orbitals in molecules or solids nearly exactly keep the SO(3) symmetry, their theories often appear as a leitmotiv in core-level spectroscopy (CLS) studies at present.

The development of many-body physics promoted application of CLS to solid state.

Let us concentrate our attention to that in the X-ray regime. Apart from an academic trend of research such as Fermi edge singularity, it was Siegbahn and co-workers who stated the significance of CLS in material science of solid states. They named X-ray photoemission spectroscopy ESCA (Electron Spectroscopy for Chemical Analysis), and had carried out extensive studies on ESCA since their first publication of their review in 1967 [5]. With their systematic analysis, Siegbahn won the Nobel Prize in 1981. Because of the recent development of synchrotron light sources, and the establishment of modern theory of CLS as will explained in the next subsection, CLS forms a huge research field in material science today.

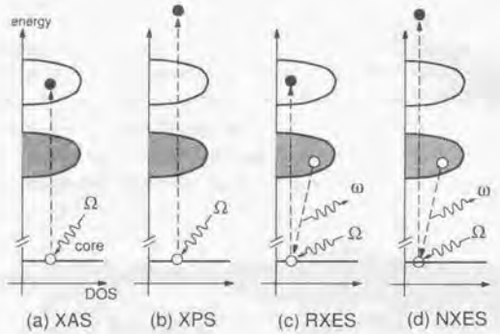

Figure 1.1: Schematic explanation of various core-level spectroscopies in an insulator. The horizontal and vertical axes schematically represent the energy and density of states of one-electron state, respectively. There are an empty upper band and a filled valence band in the system. The core level is represented with the horizontal bar. XAS and XPS are classified into the first-order optical process, whereas RXES and RXES are into the second-order optical process. See the explanation in the text.

Figure 1.1 shows a number of modes of CLS for an insulator. In X-ray absorption spectroscopy (XAS), a core electron is photoexcited by an incident X-ray with energy Ω into an empty valence state. Roughly speaking, the density of states (DOS) of unoccupied band would reflect on an XAS spectrum. In the case of X-ray photoemission spectroscopy (XPS), a core electron is photoexcited into a high-energy continuum. The energy of the photoelectron is simply that of the core level if there were no core-valence Coulomb interaction. However, the existence of valence fluctuation in a class of materials and strong Coulomb interaction gives rise to complicated spectra. XAS and

XPS are classified into first-order optical processes, where "first-order" means that they can be described within a first-order perturbation theory of electron-photon interaction.

Resonant X-ray emission spectroscopy (RXES) is a second-order optical process, where a core electron is resonantly photoexcited to an empty valence level, then a valence electron makes a radiative transition to emit an X-ray with energy ω. In contrast to XAS and XPS, there is no deep core hole in the final state, and the number of electrons in the final state is the same as that of the ground state. Thus its spectra are directly compared to those of valence level experiments, *e.g.*, optical conductivity. RXES, however, has several advantages over other spectroscopies. *First*, it is a site- and shell-selective experiment. For example, one can separately excite a Cu $2p$ orbital or an O $1s$ orbital in a CuO_2 plane of high-T_c cuprates, by tuning incident photon energy Ω at an appropriate range. This is a common feature of CLS, and it makes CLS free from overlapping effects between, *e.g.*, the Cu $3d$ and O $2p$ orbitals in the CuO_2 plane in valence spectroscopies.

The *second* advantage of RXES as a photon-in and photon-out experiment is bulk-sensitivity, which owes the long escape depth of X-rays. Generally, the escape depth of X-rays is hundreds of times longer than that of a photoelectron, which is of order of at most a few ten Å [6, 7]. The *third* advantage of RXES is due to its resonance behavior. By tuning Ω at a specific structure of XAS, one can choose the corresponding excited state "by hand" in the final state. This freedom is quite useful to study a gap structure. Besides, it is possible in principle that RXES sensitively reflects electron dynamics associated with variety of relaxation processes after the creation of a core hole, through resonant selection of an intermediate state. The *fourth* advantage of RXES is due to its selection rule. As will be explained with its explicit spectral function in § 1.2, RXES obeys selection rules of a local point group such as dipole selection rule, as well as of the translational group of a whole crystal. This duality is extremely suitable for strongly correlated systems, where local as well as itinerant nature of electrons is realized.

Let us turn our eyes to other spectroscopies again. Figure 1.1 (d) shows "normal" X-ray emission spectroscopy (NXES), where a core electron is photoexcited into a high-energy continuum, not into a valence state. Evidently, its intermediate state is the same as the final state of XPS, whereas the intermediate state of RXES is the same as that of XAS. Despite the apparent resemblance, NXES is quite different from RXES in at least two respects. First, the emitted photon energy ω is independent of the incident photon energy Ω in principle; ω roughly reflects DOS of the filled valence band. Second, apart from the photoelectron, the number of electrons in the final state decreases by one from that of the initial state. Accordingly, one has to use a spectral function considerably different from that of RXES in order to calculate NXES spectra.

Figure 1.2 (a) shows valence photoemission spectroscopy (v-PES or simply PES),

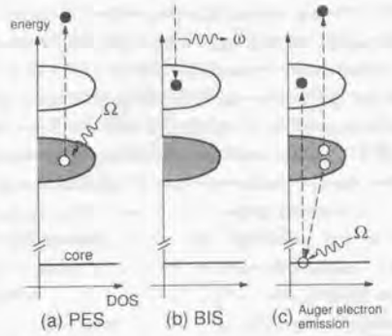

Figure 1.2: Schematic explanation of valence spectroscopies and Auger electron emission process in an insulator. See the caption in Fig. 1.1 and the explanation in the text.

where a valence electron is photoexcited into a high energy continuum, so that the valence band information is directly obtained. Figure 1.2 (b) shows a radiative process caused by a fast electron beam. As expected from the figure, it roughly reflects DOS of the unoccupied band. This spectroscopy is called inverse photoemission spectroscopy (IPES) or Bremsstrahlung Isocromat Spectroscopy (BIS). Although these valence spectroscopies have subtle things such as surface-sensitivity and charging effects for insulators, experimental resolution in the latest high-resolution PES is still higher than that of RXES at present, where the resolution of order of a few hundred meV is reported at best. Recent improvements in experimental apparatus [8], however, would make possible higher resolution for RXES in the near future.

Figure 1.2 (c) shows an Auger decay process. After a core hole is photocreated, electronic correlation between electrons can give rise to a nonradiative decay involving a simultaneous creation of an unbound electron. Mathematically, this is due to a term such as

$$U_{\rm A} c^\dagger_{\boldsymbol{r}} \beta^\dagger_\varepsilon a_{\boldsymbol{r}1} a_{\boldsymbol{r}2} \tag{1.1}$$

in the Hamiltonian, where $U_{\rm A}$ represents Coulomb interaction energy, and $c^\dagger_{\boldsymbol{r}}$ is a creation operator of a core electron at a given site $\boldsymbol{r}$. $a_{\boldsymbol{r}1}$ and $a_{\boldsymbol{r}2}$ are annihilation operators of different kind of valence orbitals, respectively. $\beta^\dagger_\varepsilon$ is a creation operator of an unbound state with energy ε. We discuss a role of the Auger effect in RXES in the next section.

1.1.2 Origin of impurity models

The effects of impurity atoms on the properties of a metal is of considerable physical interest, because of its singular behavior beyond uniform Fermi liquid theory [9]. A typical example is the resistance minimum, which is observed in such metals as Cu and Al doped with a small amount of Fe or Ni. In 1961, Anderson proposed the following model [10], the Anderson model, to discuss the magnetic moment of the impurities,

$$H_{\rm And} = \sum_{\boldsymbol{k},\sigma} \varepsilon_{\boldsymbol{k}} a^\dagger_{\boldsymbol{k},\sigma} a_{\boldsymbol{k},\sigma} + \sum_\sigma \varepsilon_d d^\dagger_\sigma d_\sigma + \frac{1}{\sqrt{N}} \sum_{\boldsymbol{k},\sigma} \left(V_{\boldsymbol{k}} a^\dagger_{\boldsymbol{k},\sigma} d_\sigma + \text{H.c.} \right) + U_{dd} d^\dagger_\uparrow d_\uparrow d^\dagger_\downarrow d_\downarrow, \tag{1.2}$$

where $a^\dagger_{\boldsymbol{R},\sigma}$ is a creation operator of a conduction electron of the host metal with wave number $\boldsymbol{k}$ and a spin component σ. Similarly, $d^\dagger_\sigma$ is a creation operator of the impurity $3d$ orbital. $\varepsilon_{\boldsymbol{k}}$ and ε_d are one-electron energies of the conduction band and the impurity orbital, respectively. U_{dd} is the Coulomb interaction of the impurity orbital. $V_{\boldsymbol{k}}$ is the hybridization energy between conduction electron and the impurity orbital. N is the number of atoms of the host metal. In the limit of $|V_{\boldsymbol{k}}/U_{dd}| \ll 1$, $H_{\rm And}$ is transformed into the $\boldsymbol{sd}$ model through Schrieffer-Wolff transformation [11], the model with which Kondo gives a clear-cut explanation for the long-standing challenge of the resistance minimum in 1964 [12].

Since the middle of the 1960s, the impurity model had been applied to the Fermi edge problem of X-ray spectra. To discuss XAS or XPS spectra of simple metals [1], a localized core orbital was introduced in place of d_σ in $H_{\rm And}$, and the Coulomb interaction U_c between conduction and core orbitals were added,

$$H_{\rm MND} = \sum_{\boldsymbol{k},\sigma} \varepsilon_{\boldsymbol{k}} a^\dagger_{\boldsymbol{k},\sigma} a_{\boldsymbol{k},\sigma} - U_c \sum_\sigma a^\dagger_{\boldsymbol{0},\sigma} a_{\boldsymbol{0},\sigma} n_c + \varepsilon_c (1 - n_c), \tag{1.3}$$

where n_c is the number of core holes at a given site, say, the origin $\boldsymbol{0}$. n_c is 0 for the initial state, 1 for the final state. $a^\dagger_{\boldsymbol{0},\sigma}$ is a creation operator of the conduction electron at the site $\boldsymbol{0}$. This is often called Mahan-Nozières-DeDominicis (MND) model [13]. Based on this Hamiltonian, Nozières and De Dominicis (ND) completely disclosed the origin of the Fermi edge singurarity [14], with elaborate techniques in those days [15].

Subsequently to their celebrated work, Kotani and Toyozawa (KT) dealt with core level spectra of metals with incomplete shells [16]. They added a localized orbital f to the MHD model,

$$H_{\rm KT} = \sum_{\boldsymbol{k}} \varepsilon_{\boldsymbol{k}} a^\dagger_{\boldsymbol{k}} a_{\boldsymbol{k}} + \varepsilon_f f^\dagger f + \varepsilon_c (1 - n_c) - U_{fc} f^\dagger f n_c + \frac{V}{\sqrt{N}} \sum_{\boldsymbol{k}} \left(a^\dagger_{\boldsymbol{k}} f + \text{H.c.} \right), \tag{1.4}$$

with which they explained a satellite structure of La $3d$-XPS of La metal [17]. Figure 1.3 schematically shows their theory. In the ground (initial) state, La metal takes a

[1] While X-ray emission spectra had been also discussed in those days, it was regarded as a first order optical process, i.e. neither resonant nor normal X-ray emission processes.

f^0 configuration because the energy of La $4f$ level ε_f is high enough from the Fermi energy ε_F. In the final state, however, the strong core hole potential U_{fc} pulls down the $4f$ level, so that "well-screened" $4f^1$ and "poorly-screened" $4f^0$ states are realized. The former involves the infinite number of electron-hole pairs near the Fermi level to exhibit a divergent line shape at the threshold. The f^0 state can be regarded as a virtual bound state occupied by a conduction electron, with a Lorentzian-broadened line shape. The KT theory is the first recognition that dynamic *screening* processes due to the local perturbation give rise to the variety of line shapes of core-level spectra, and in this sense it opened a door to the modern theory of CLS.

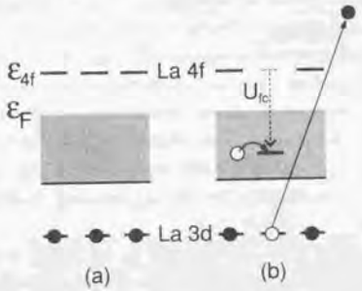

Figure 1.3: Schematic explanation of Kotani-Toyozawa theory, reprinted from Ref. [17] with unessential modifications. (a) In the ground state, La $4f$ orbitals are above the Fermi level ε_F, and $3d$ core orbitals are far below ε_F and filled. (b) A final state of La $3d$-XPS, where a core electron is photoexcited into high-energy continuum. The strong core hole potential U_{fc} pulls down the $4f$ level below ε_F. A conduction electron screens the core hole through a finite value of hybridization between $4f$ and conduction electrons.

From a viewpoint of theoretical physics, the KT theory can be regarded as an epitaph on the ND theory, one of the most brilliant theories in the 1960s. Their framework has provided some topics ever since, such as a renormalization group study on the KT model [18] and a revisit of the ND theory in the context of Tomonaga-Luttinger theory [19].

The next remarkable development in CLS was done by Gunnarson and Schönhammer (GS) in 1983 [20]. They applied the KT model to valence-fluctuated systems. For $CePd_3$ or CeO_2, the $4f$ occupation number in the ground state takes a given value from 0 to 1 in contrast to the La metal, where the $4f^0$ weight is predominant

in the ground state. If one goes along the KT theory, it is expected that three peaks with mainly $4f^0$, $4f^1$ and $4f^2$ configurations are observed in Ce 3d-XPS spectra. As will be explained in § 1.4.1, GS extended the KT model to include the degeneracy of $4f$ orbital and the Coulomb interaction between $4f$ electrons, and showed a systematic way to calculate XAS, XPS and BIS. One can say that GS led the KT theory to its complete form within the impurity problem. The GS model is now referred to also as impurity Anderson model. We will use the word "impurity model" for the GS-type model hereafter.

1.1.3 Mott-Hubbard vs charge-transfer insulator

It is not surprising that the direction of studies on CLS turned toward application to material science after the establishment of the basic concept. This trend was motivated by successful works on the classification of insulators such as NiO by Fujimori-Minami [21] and Zaanen-Sawatzky-Allen (ZSA) [22].

Ti_2O_3, V_2O_3, NiO, etc. have been well-known insulators, where the Coulomb interaction U_{dd} plays an essential role [23]. In fact, they would be metals according to the simple band theory if U_{dd} were missing. *Prior to* the works by Fujimori-Minami and ZSA, the lowest charge excitation in these compounds were believed to be made by an inter-site d-d charge transfer:

$$(d^n)_i(d^n)_j \rightarrow (d^{n-1})_i(d^{n+1})_j,$$

where n is the nominal occupation number of a material considered, i and j label transition metal sites. This process gives a charge gap of order of U_{dd}, and this type of insulators have been called a Mott-Hubbard (MH) insulator after pioneer works by Mott [24] and their mathematical sophistication by Hubbard [25].

Using a NiO_6^{-10} octahedral cluster model, Fujimori-Minami discussed photoemission spectra of NiO, and they concluded from their calculation that the charge gap is realized by a transition to a metal $3d$ site from its surrounding oxygen $2p$ orbitals. They estimated the value of Δ_f=4.0 and U_{dd}=7.5 for NiO, where charge-transfer (CT) energy Δ_f is defined by the energy difference

$$\Delta_f \equiv E(d^{n+1}\underline{L}) - E(d^n), \tag{1.5}$$

where $\underline{L}$ stands for a ligand hole [2]. ZSA, on the other hand, performed systematic estimation of charge gaps in transition metal compounds with the GS theory. They classified the insulators into three groups according to relative value between Δ_f and U_{dd}: MH type, CT type and their intermediate type. Standing on their classification, one can regard NiO as a CT insulator because of $U_{dd} > \Delta_f$.

[2] One should average over all irreducible representations to evaluate the energy.

In this connection, a while after their works, Uozumi performed extensive calculations on $2p$-XPS of M_2O_3-type transition metal oxides with a MO_6 cluster model for M=Ti, V, Cr, Mn and Fe including full multiplet [26, 27]. While he obtained parameter values that $\Delta_l > U_{dd}$ for Ti and V, and $\Delta_l < U_{dd}$ for others, he concluded that Ti, V, Cr and Mn sesquioxides should be classified into the intermediate type insulator because of large values of metal-ligand hybridization. His results are summarized in Fig. 1.4. This conclusion was supported by Bocquet *et al.*, who also discussed $2p$-XPS for various transition metal oxides [28]. These studies are representative of application of CLS to investigation of electronic structure for strongly-correlated insulators. The site-selectivity encourages us to use the impurity models for a quantitative analysis of core-level spectra. While CLS's need additional parameters such as core-valence interaction, it is possible to estimate them to satisfactory accuracy with the standard atomic Hartree-Fock procedure [26, 27]. With contemporary numerical diagonalization techniques and new generation synchrotron radiation sources, a comparative study of this kind between theory and experiment in CLS has established reputation of being one of the most reliable tools to investigate correlated systems.

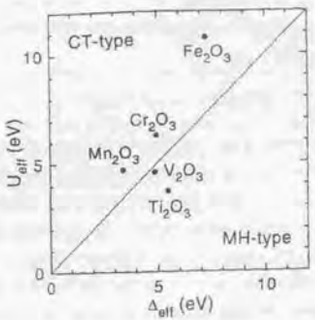

Figure 1.4: The ZSA diagram by Uozumi *et al.* [27]. Ti_2O_3, V_2O_3, Cr_2O_3 and Mn_2O_3 are located in the intermediate region between CT- and MH-insulators, whereas Fe_2O_3 is classified as a CT-type insulator.

1.1.4 Nonlocal screening

As is the case of the theories of Fujimori-Minami or Uozumi *et al.*, theoretical studies with impurity models are based on an assumption that a broken translational symmetry

calculation is, as far as transition metal ions are considered, a good approximation for transition metal compounds. An exact calculation in principle should include also the translational symmetry of the transition metal ions. Since d-band dispersion width have been believed to be usually very small compared to U_{dd} or Δ_l, it has been expected that neglect of this would only cause small errors in calculated insulating gaps, and would not change the physics unless perhaps if the gaps also turn out to be very small [22].

The discovery of high-T_c compounds [29], however, provided a new viewpoint on this assumption, and thus on interpretation of core-level spectra. The traditional BCS theory states that Cooper pair creation at the Fermi surface gives rise to superconductivity [30]. The high-T_c superconductivity is, however, caused by carrier doping into an insulating phase. In the insulating parent compounds such as La_2CuO_4, the stoichiometry leads to a d^9 configuration for Cu^{2+} ions. Since these compounds with such incomplete filled d band would be metals if strong U_{dd} were absent, it is clear that the Coulomb correlation prevents the motion of electrons. There is a consensus that the parent compounds are located in the CT regime. Upon doping, by replacing a few percent of La with Sr in the case of La_2CuO_4 for instance, a dopant hole mainly goes into the O $2p$ orbitals, keeping away from energetically unfavorable d^8 configuration. Experimental evidence of this negligible d^8 weight was given by valence PES results by Fujimori *et al.* [31] and other groups [32]. Subsequently, experimental studies on O $1s$-XAS [33] and Cu $2p$-XAS [34, 35] conclusively demonstrated their conclusion, making full use of the advantages of CLS such as the site-selectivity and dipole-selectivity. These are also worth referring to as an example for application of CLS to material science.

The high-T_c systems were impressive for the fresh interplay between localized (insulating) and itinerant (superconducting) natures. Analogous to these systems, it was natural for van Veenendaal and co-workers to anticipate doping dependence on Ni $2p$-XPS of $M_xNi_{1-x}O$ (M=Li, Na). Extending the NiO_6 cluster model of Fujimori-Minami to include a "reservoir" Ni, they showed that a description beyond an atomic multiplet calculation is required [36]. Subsequently, they discussed influence of superexchange interaction [37, 38] on isotropic Ni $2p$-XAS in NiO [39] with the reservoir model, and reported that spin-spin correlation has a direct effect on the spectra [40]. Encouraged by these results, they performed a calculation on Ni $2p$-XPS of NiO with a Ni_7O_{36} cluster model, where only $3d$ e_g orbitals and the σ-bonding O $2p$ orbitals are taken into account [41]. Thereby they pointed out that an experimentally observed shoulder structure in the main manifold of $2p$-XPS originates from a CT screening process from a neighboring NiO_6 unit, not only from the oxygen orbitals adjacent to the photoexcited Ni site. This is the first discovery of nonlocal screening effects.

Their results are shown in Fig. 1.5 in comparison with a result with NiO_6 cluster.

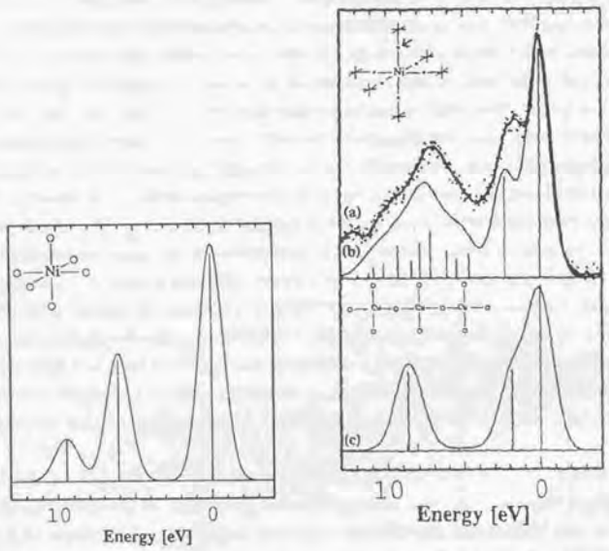

Figure 1.5: The discovery of nonlocal screening effect in Ni $2p$-XPS of NiO and cuprates [41]. Left: Calculated Ni $2p$-XPS spectrum with a NiO_6 cluster model as described in the inset. Right: (a) Experimental spectrum of Ni $2p$-XPS [42]. (b) Calculated Ni $2p$-XPS spectrum with a Ni_7O_{36} cluster model as described in the inset. (c) Calculated Cu $2p$-XPS spectrum of a Cu_3O_{10} cluster model as described in the inset.

where three peaks mainly due to $\underline{c}3d^9\underline{L}$, $\underline{c}3d^8$ and $\underline{c}3d^{10}\underline{L}^2$ weight are observed (left figure). $\underline{c}$ and $\underline{L}$ represent a hole at a core orbital and a ligand orbital, respectively. In the right figure, the curve (b) exhibits a clear shoulder structure beside the main peak at zero. This is the contribution of the nonlocal screening.

More surprisingly, they disclosed that the *main* peak of Cu $2p$-XPS of CuO and high-T_c cuprates also originates from a nonlocal screening process, where a hole is pushed out by a strong intra-atomic Cu $2p$-$3d$ interaction into the neighboring CuO_4 units to form a Zhang-Rice singlet [43]. The calculated curve in Fig. 1.5 (c) shows their result, where the main peak at zero is the Zhang-Rice singlet peak. The shoulder at about 2 eV and the satellite at about 9 eV are attributed to contributions mainly of $\underline{c}3d^{10}\underline{L}$ and $\underline{c}3d^9$, respectively. These two peaks have been known from analysis based on impurity models.

Do these striking results mean that all theoretical studies on CLS to date based on the impurity models should be thrown away? The clear answer has not been known so far. Although a systematic study on CLS of transition metal compounds with such "large"-cluster models beyond the impurity limit is clearly desirable, the limitation of memory size of computers prevents us from investigation with realistic models. In fact, the inclusion of orbital degeneracy in a multi-metal-ion cluster is extremely difficult within exact diagonalization methods. To the author's knowledge, the only attempt is a full-multiplet calculation of valence spectra with a Cu_3O_{10} cluster by Tanaka and Jo [44]. This kind of calculation for d^n materials with $2 \leq n \leq 8$ is far from the ability of the present supercomputers. Now clear that a model study to grasp the essential physics is needed.

At least for metal $2p$-XPS of NiO and high-T_c cuprates, the reason why the nonlocal screening effect plays the severe role is that each material has a specific stabilization mechanism such as the Zhang-Rice singlet formation in cuprates. In this respect, van Veenendaal *et al.* demonstrated in their analysis on Ni $2p$-XPS [41] that the doubly-peaked structure disappears when raising the d orbital energies on sites other than the photoexcited Ni atom, because of the absence of d orbitals in the valence band region. The strong nonlocal contribution on $2p$-XPS in NiO and CuO or high-T_c cuprates may be related to their character as a typical CT-type insulator [45].

1.1.5 A new aspect of nonlocal effects

Recent development of synchrotron radiation sources shed a light on nonlocal effects of CLS from another side. As explained, RXES, whose experimental resolution was drastically improved with such high-brilliance light sources, has the remarkable feature that it reflects local as well as itinerant natures of electronic systems. Thus, it is expected that nonlocal effects emerge in a specific manner different from XAS or XPS.

Recent experiments on metal $3d$-$2p$ RXES of transition metal oxides clearly suggest this sign. Tezuka *et al.* first reported strange excitation energy (Ω) dependence of RXES spectra in a d^0 compound TiO_2 [46]. Figure 1.6 shows Ti $3d$-$2p$ RXES of a d^0 compound $FeTiO_3$ measured by Butorin *et al.* [47], exhibiting a similar feature to that of TiO_2. We see that there is a broad spectrum at about 450 eV for nearly all Ω as if emitted photon energy (ω) had little dependence on Ω. We call these spectra fluorescence-like component hereafter. On the other hand, there are observed Ω-dependent spectra which move nearly in parallel to Ω, keeping their energy distance from the elastic line constant. If we arrange the same spectra with Raman shift, which is defined by $\omega - \Omega$, they will stand in a line at a value of Raman shift. Hence, we call them simply Raman component hereafter. This double-component feature in metal $3d$-$2p$ RXES is observed in various transition metal oxides [48] in addition to these compounds.

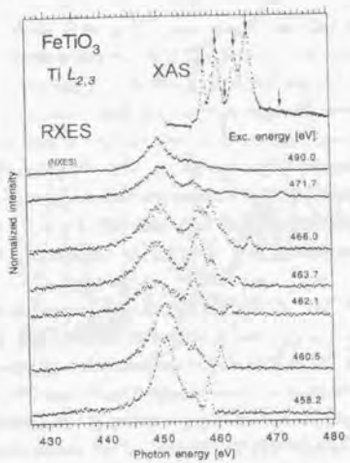

Figure 1.6: Experimental XAS, NXES and RXES spectra of $FeTiO_3$ [47]. The arrows attached to the XAS spectrum indicate the excitation energy. The NXES spectrum is at the top of the array of RXES spectra for excitation energy well above the absorption threshold (490.0 eV). A small but relatively sharp peak at the highest emitted photon energy in each of excitation energy is the elastic line. The fluorescence-like spectra are clearly observed.

The fluorescence-like spectra are not understandable from a viewpoint of impurity

models. XAS and XPS spectra of TiO_2 are extremely well reproduced with a TiO_6 cluster model [49]. Thus it is expected that a dominant class of intermediate state when Ω is tuned at the absorption threshold is fairly localized in a photoexcited TiO_6 unit, and that final states left after an X-ray emission process from these intermediate states should be described within local CT excitations, being strongly dependent on the well- or poorly-screened natures of the intermediate states. In other words, the intermediate state keeps full memory of the incident X-ray, and the corresponding final state should depend on Ω accordingly. Since energy scale of local CT excitations is determined by Δ_f or $V_{\rm eff}$ (see § 1.4), which has the value of order of at most 10 eV, the energy conservation rule

$$\omega = E_g - E_f + \Omega$$

never predicts the fluorescence-like spectra over whole range of the absorption threshold. E_g and E_f being electronic energies of the ground state and a final state, respectively. It rather predicts only the existence of the Raman component.

The fluorescence-like spectra suggest a dynamical *dissipation* process of the photoexcited electron, which results in loss of the memory of the photoexcited site. If the dissipation from the photoexcited site to the surrounding reservoir system completely occurs in the intermediate state, an X-ray emission process necessarily resembles NXES, resulting in the fluorescence-like spectra. Hence, we consider the double-component spectra to be a direct consequence of interplay between local and itinerant excitations of an electronic system. This is a new kind of nonlocal effect in CLS, which might bring about a new understanding as to the local-itinerant duality of $3d$ systems. Together with the "traditional" nonlocal effect van Veenendaal *et al.* have demonstrated, the main theme of this thesis is to study how the nonlocal effects appear in RXES spectra.

1.2 Resonant Scattering

1.2.1 Quantum theory of radiation

The classical radiation field is governed by the following reduced Maxwell equations for the vector potential $\boldsymbol{A}$ under the radiation (Coulomb) gauge [50]:

$$\left(\nabla\cdot\nabla - \frac{1}{c^2}\frac{\partial^2}{\partial t^2}\right)\boldsymbol{A} = 0 \tag{1.6}$$

$$\nabla\cdot\boldsymbol{A} = 0. \tag{1.7}$$

We adopt the MKSA rationalized unit throughout this section. The magnetic field $\boldsymbol{B}$ and electronic field $\boldsymbol{E}$ are derived from $\boldsymbol{A}$:

$$\boldsymbol{B} = \nabla\times\boldsymbol{A} \tag{1.8}$$

$$\boldsymbol{E} = \frac{\partial \boldsymbol{A}}{\partial t}. \tag{1.9}$$

Multiplying Eq. (1.6) by $\partial \boldsymbol{A}/\partial t$, we have

$$\frac{1}{2}\frac{\partial}{\partial t}\left[\frac{1}{c^2}\left(\frac{\partial \boldsymbol{A}}{\partial t}\right)^2 + (\nabla \times \boldsymbol{A})^2\right] = \nabla \cdot \left[\frac{\partial \boldsymbol{A}}{\partial t} \times (\nabla \times \boldsymbol{A})\right], \tag{1.10}$$

where the transversality condition Eq. (1.7) and mathematical identities that

$$\nabla \times (\nabla \times \boldsymbol{A}) = \nabla(\nabla \cdot \boldsymbol{A}) - (\nabla \cdot \nabla)\boldsymbol{A}$$

and

$$\nabla \cdot \left[(\nabla \times \boldsymbol{A}) \times \frac{\partial \boldsymbol{A}}{\partial t}\right] = \frac{\partial \boldsymbol{A}}{\partial t} \cdot [\nabla \times (\nabla \times \boldsymbol{A})] - (\nabla \times \boldsymbol{A}) \cdot \left(\nabla \times \frac{\partial \boldsymbol{A}}{\partial t}\right)$$

have been used. The right side of Eq. (1.10) vanishes according to the Gauss' divergence theorem when integrated over the total volume, so that

$$\mathcal{H}_r \equiv \frac{1}{2}\int \mathrm{d}^3\boldsymbol{x}\left(\varepsilon_0 \boldsymbol{E}^2 + \frac{1}{\mu_0}\boldsymbol{B}^2\right) \tag{1.11}$$

is a time-independent constant. μ_0 and ε_0 are the magnetic permeability and dielectric constant of the vacuum, respectively. The integrand of the above equation has the unit of energy density, because the units of $\boldsymbol{E}$ and ε_0 are $[\mathrm{NC}^{-1}]$ and $[\mathrm{C}^2\mathrm{Nm}^{-2}]$, respectively. Hence, one can interpret $\mathcal{H}_r$ as the total energy function of the radiation field.

The quadratic form in Eq. (1.11) suggests Fourier decomposition as

$$\boldsymbol{A}(\boldsymbol{x}, t) = \frac{1}{2\sqrt{V}}\sum_{\boldsymbol{q},\boldsymbol{\epsilon}} \boldsymbol{\epsilon}\left[a^*_{\boldsymbol{q},\boldsymbol{\epsilon}}(t)\mathrm{e}^{\mathrm{i}\boldsymbol{q}\cdot\boldsymbol{x}} + a_{\boldsymbol{q},\boldsymbol{\epsilon}}(t)\mathrm{e}^{-\mathrm{i}\boldsymbol{q}\cdot\boldsymbol{x}}\right], \tag{1.12}$$

from which we have

$$\boldsymbol{E}(\boldsymbol{x}, t) = -\frac{1}{2\sqrt{V}}\sum_{\boldsymbol{q},\boldsymbol{\epsilon}} \boldsymbol{\epsilon}\left[\dot{a}^*_{\boldsymbol{q},\boldsymbol{\epsilon}}(t)\mathrm{e}^{\mathrm{i}\boldsymbol{q}\cdot\boldsymbol{x}} + \dot{a}_{\boldsymbol{q},\boldsymbol{\epsilon}}(t)\mathrm{e}^{-\mathrm{i}\boldsymbol{q}\cdot\boldsymbol{x}}\right] \tag{1.13}$$

$$\boldsymbol{B}(\boldsymbol{x}, t) = \frac{1}{2\sqrt{V}}\sum_{\boldsymbol{q},\boldsymbol{\epsilon}} \mathrm{i}\boldsymbol{\epsilon} \times \boldsymbol{q}\left[a^*_{\boldsymbol{q},\boldsymbol{\epsilon}}(t)\mathrm{e}^{\mathrm{i}\boldsymbol{q}\cdot\boldsymbol{x}} - a_{\boldsymbol{q},\boldsymbol{\epsilon}}(t)\mathrm{e}^{-\mathrm{i}\boldsymbol{q}\cdot\boldsymbol{x}}\right]. \tag{1.14}$$

The polarization vector $\boldsymbol{\epsilon}$ is restricted within the plane perpendicular to $\boldsymbol{q}$ according to the transversality condition. Each Fourier component satisfies the condition $a^*_{-\boldsymbol{q},\boldsymbol{\epsilon}} = a_{\boldsymbol{q},\boldsymbol{\epsilon}}$. By substituting with them, Eq. (1.11) reads

$$\mathcal{H}_r = \frac{\varepsilon_0}{2}\sum_{\boldsymbol{q},\boldsymbol{\epsilon}}\left(\dot{a}_{-\boldsymbol{q},\boldsymbol{\epsilon}}\dot{a}_{\boldsymbol{q},\boldsymbol{\epsilon}} + c^2\boldsymbol{q}^2 a_{-\boldsymbol{q},\boldsymbol{\epsilon}} a_{\boldsymbol{q},\boldsymbol{\epsilon}}\right) \tag{1.15}$$

after some algebra. In the free radiation field, this function is regarded as the Langangian $\mathcal{L}$ for canonical coordinates $\{a_{\boldsymbol{q},\boldsymbol{\epsilon}}\}$. Following the standard procedure in classical mechanics [51], we define canonical momentum $p_{\boldsymbol{q},\boldsymbol{\epsilon}}$ as

$$p_{\boldsymbol{q},\boldsymbol{\epsilon}} \equiv \frac{\partial \mathcal{L}}{\partial \dot{a}_{\boldsymbol{q},\boldsymbol{\epsilon}}} = \frac{1}{2}\varepsilon_0 \dot{a}_{-\boldsymbol{q},\boldsymbol{\epsilon}}.$$

Now we introduce quantized canonical variables by postulating quantization conditions

$$[a_{-\boldsymbol{q},\boldsymbol{\epsilon}}, p_{\boldsymbol{q}',\boldsymbol{\epsilon}'}] = \mathrm{i}\hbar\delta_{\boldsymbol{q},\boldsymbol{q}'}\delta_{\boldsymbol{\epsilon},\boldsymbol{\epsilon}'}$$

$$[a_{\boldsymbol{q},\boldsymbol{\epsilon}}, a_{\boldsymbol{q}',\boldsymbol{\epsilon}'}] = [p_{\boldsymbol{q},\boldsymbol{\epsilon}}, p_{\boldsymbol{q}',\boldsymbol{\epsilon}'}] = 0,$$

where square brackets represent the commutator, and the deltas represent the Kronecker's delta functions. Additional conditions $a^\dagger_{\boldsymbol{q},\boldsymbol{\epsilon}} = a_{-\boldsymbol{q},\boldsymbol{\epsilon}}$ and $p^\dagger_{\boldsymbol{q},\boldsymbol{\epsilon}} = p_{-\boldsymbol{q},\boldsymbol{\epsilon}}$ are naturally assumed. In addition, we introduce the Bose operators as

$$b^\dagger_{\boldsymbol{q},\boldsymbol{\epsilon}} = \sqrt{\frac{\varepsilon_0\omega_{\boldsymbol{q}}}{2\hbar}}a_{-\boldsymbol{q},\boldsymbol{\epsilon}} + \mathrm{i}\sqrt{\frac{2}{\hbar\varepsilon_0\omega_{\boldsymbol{q}}}}p_{\boldsymbol{q},\boldsymbol{\epsilon}},$$

so that the classical Hamiltonian $\mathcal{H}_r(\{a_{\boldsymbol{q},\boldsymbol{\epsilon}}, p_{\boldsymbol{q},\boldsymbol{\epsilon}}\})$ is associated with quantum mechanical Hamiltonian H_r

$$H_r = \sum_{\boldsymbol{q},\boldsymbol{\epsilon}} \hbar\omega_{\boldsymbol{q}} b^\dagger_{\boldsymbol{q},\boldsymbol{\epsilon}} b_{\boldsymbol{q},\boldsymbol{\epsilon}}, \tag{1.16}$$

where we denote $c|\boldsymbol{q}|$ by $\omega_{\boldsymbol{q}}$. Equation (1.16) encourages us to interpret the Bose operator $b^\dagger_{\boldsymbol{q},\boldsymbol{\epsilon}}$ as the creation operator of a photon with the polarization vector $\boldsymbol{\epsilon}$ and wave number vector $\boldsymbol{q}$. After all, $\boldsymbol{A}$ is quantized in terms of the boson operators as

$$\boldsymbol{A}(\boldsymbol{x}) = \sqrt{\frac{\hbar}{2\epsilon_0\omega_{\boldsymbol{q}}V}}\sum_{\boldsymbol{q},\boldsymbol{\epsilon}} \boldsymbol{\epsilon}\left(b^\dagger_{\boldsymbol{q},\boldsymbol{\epsilon}}\mathrm{e}^{\mathrm{i}\boldsymbol{q}\cdot\boldsymbol{x}} + b_{\boldsymbol{q},\boldsymbol{\epsilon}}\mathrm{e}^{-\mathrm{i}\boldsymbol{q}\cdot\boldsymbol{x}}\right). \tag{1.17}$$

1.2.2 Electron-photon interaction

The electron-photon interaction is given by [52]

$$H_{\mathrm{ep}} = \int \mathrm{d}^3\boldsymbol{x}\Psi(\boldsymbol{x})^\dagger\left[\frac{e}{m_e}\boldsymbol{A}\cdot(-\mathrm{i}\hbar\nabla)\right]\Psi(\boldsymbol{x}), \tag{1.18}$$

where $\Psi(\boldsymbol{x})^\dagger$ represents the creation operator of the electron field at $\boldsymbol{x}$. The charge and mass of an electron are represented as e and m_e, respectively. We postulate that $\Psi(\boldsymbol{x})^\dagger$ and $\Psi(\boldsymbol{x})$ obey the anticomutation relations (quantization condition)

$$\{\Psi(\boldsymbol{x}), \Psi(\boldsymbol{x}')^\dagger\} = \delta^3(\boldsymbol{x} - \boldsymbol{x}')$$

$$\{\Psi(\boldsymbol{x}), \Psi(\boldsymbol{x}')\} = \{\Psi(\boldsymbol{x})^\dagger, \Psi(\boldsymbol{x}')^\dagger\} = 0,$$

where $\delta^3(\boldsymbol{x} - \boldsymbol{x}')$ is the three-dimensional version of Dirac's delta function. Since we are only interested in physics near absorption edges, the Thomson term $(e\boldsymbol{A})^2/2m_e$ is omitted from Eq. (1.18). In XAS and RXES, one can usually assign principal and

angular quantum numbers of core and valence orbitals by tuning the excitation energy Ω at the appropriate absorption edge [3]. Now $\Psi(\boldsymbol{x})^\dagger$ is expanded as

$$\Psi(\boldsymbol{x})^\dagger = \sum_{\boldsymbol{R}\sigma}\left[\sum_m \phi_m(\boldsymbol{x}-\boldsymbol{R})^* l^\dagger_{\boldsymbol{R}m\sigma} + \sum_{m_c}\psi_{m_c}(\boldsymbol{x}-\boldsymbol{R})^* c^\dagger_{\boldsymbol{R}m_c\sigma}\right], \tag{1.19}$$

where ϕ_m and ψ_{m_c} are Wannier functions with atomic quantum numbers of (n,l,m) and (n_c,l_c,m_c), respectively. $l^\dagger_{\boldsymbol{R}m\sigma}$ creates a valence electron with σ-component of spin at $\boldsymbol{R}$ site, and $c^\dagger_{\boldsymbol{R}m_c\sigma}$ is the same operator for the core electrons. Substituting the above equation and Eq. (1.17) into Eq. (1.18), $H_{\rm ep}$ is expressed as the summation of the following operators

$$T_{\rm a} = \frac{1}{\sqrt{N}}\sum_{\boldsymbol{R}} \mathrm{e}^{\mathrm{i}\boldsymbol{q}_1\cdot\boldsymbol{R}} T^{\rm a}_{\boldsymbol{\epsilon}}(\boldsymbol{R}) \tag{1.20}$$

$$T_{\rm e} = \frac{1}{\sqrt{N}}\sum_{\boldsymbol{R}} \mathrm{e}^{-\mathrm{i}\boldsymbol{q}_2\cdot\boldsymbol{R}} T^{\rm e}_{\boldsymbol{\epsilon}'}(\boldsymbol{R}), \tag{1.21}$$

where N is the number of the unit cell of the electronic system, and

$$T^{\rm a}_{\boldsymbol{\epsilon}}(\boldsymbol{R}) = \sum_{m,m_c}\sqrt{\frac{\hbar e^2}{2\varepsilon_0 V_0 m_e^2\omega_{\boldsymbol{q}_1}}}(nlm|\mathrm{e}^{-\mathrm{i}\boldsymbol{q}_1\cdot\boldsymbol{x}}\boldsymbol{\epsilon}\cdot\boldsymbol{p}|n_c l_c m_c) l^\dagger_{\boldsymbol{R}m\sigma} c_{\boldsymbol{R}m_c\sigma} \tag{1.22}$$

$$T^{\rm e}_{\boldsymbol{\epsilon}'}(\boldsymbol{R}) = \sum_{m,m_c}\sqrt{\frac{\hbar e^2}{2\varepsilon_0 V_0 m_e^2\omega_{\boldsymbol{q}_2}}}(n_c l_c m_c|\mathrm{e}^{\mathrm{i}\boldsymbol{q}_2\cdot\boldsymbol{x}}\boldsymbol{\epsilon}'\cdot\boldsymbol{p}|nlm) c^\dagger_{\boldsymbol{R}m_c\sigma} l_{\boldsymbol{R}m\sigma}. \tag{1.23}$$

Here we dropped the photon operators, assuming that a photon with $(\boldsymbol{q}_1,\boldsymbol{\epsilon})$ is absorbed into the electronic system, and a photon with $(\boldsymbol{q}_2,\boldsymbol{\epsilon}')$ is emitted from the electronic system. V_0=V/N is the volume of the unit cell. Obviously, $T^{\rm a}$ and $T^{\rm e}$ describes X-ray absorption and emission processes, respectively. The factor before the Fermi operators is defined as

$$(nlm|\mathrm{e}^{-\mathrm{i}\boldsymbol{q}_1\cdot\boldsymbol{x}}\boldsymbol{\epsilon}\cdot\boldsymbol{p}|n_c l_c m_c) = \int \mathrm{d}^3\boldsymbol{x}\ \phi_m(\boldsymbol{x})^* \mathrm{e}^{-\mathrm{i}\boldsymbol{q}_1\cdot\boldsymbol{x}}\boldsymbol{\epsilon}\cdot(-\mathrm{i}\hbar\nabla)\psi_{m_c}(\boldsymbol{x}). \tag{1.24}$$

In the hard X-ray regime, the wavelength of photon is of order of 1 Å, and is comparable to lattice constants of a crystal in consideration. Hence one must not neglect the exponential factor in Eqs. (1.20) and (1.21). The spatial extent of the core orbital, however, is expected to be much smaller than the lattice constants, so that we approximate the above equation as

$$(nlm|\boldsymbol{\epsilon}\cdot\boldsymbol{p}|n_c l_c m_c) \simeq \int \mathrm{d}^3\boldsymbol{x}\ \phi_m(\boldsymbol{x})^*\boldsymbol{\epsilon}\cdot(-\mathrm{i}\hbar\nabla)\psi_{m_c}(\boldsymbol{x}). \tag{1.25}$$

[3] We can easily extend the theory when a few orbitals with different angular momentum participate in the transition.

This is the nontrivial lowest approximation of the integral, and we refer to it as *atomic* dipole approxmation [4]. Note that $T_{\rm a}$ and $T_{\rm e}$ in Eqs. (1.20) and (1.21) become the form of Fourier summation of the atomic operators.

1.2.3 Perturbation Theory

Consider a direct product of the electronic ground state $|g\rangle$ by a one-photon state $|\boldsymbol{q_1}\boldsymbol{\epsilon}\rangle$, and Hilbert space spanned by such states $|g;\boldsymbol{q_1}\boldsymbol{\epsilon}\rangle$. The transition amplitude from $|I\rangle \equiv |g;\boldsymbol{q_1}\boldsymbol{\epsilon}\rangle$ to a final state $|F\rangle \equiv |f;\boldsymbol{q_2}\boldsymbol{\epsilon}'\rangle$ is given by the S-matrix [56] as

$$S_{FI} \equiv \langle F|U_i(\infty,-\infty)|I\rangle,$$

where $U_i(t,t')$ is the time-evolution operator of the whole electron-photon system from time t' to t in the interaction representation [57]. The total Hamiltonian is given by

$$H_{\rm tot} = H + H_r + (H_{\rm ep} + H_{\rm A}), \tag{1.26}$$

where $H_{\rm A}$ represents an electronic Hamiltonian of the Auger process containing the terms like Eq. (1.1). H is the Hamiltonian of the electronic system other than $H_{\rm A}$. We denote $H_{\rm ep}+H_{\rm A}$ by H' for a while. Apart from the case of F=I, the S-matrix is directly reduced to [58]

$$S_{FI} = -2\pi\mathrm{i}\langle F|H'U_i(0,-\infty)|I\rangle\,\delta(E_F-E_I),$$

from which the transition probability per time is obtained,

$$w_{FI} = \frac{2\pi}{\hbar}\left|\langle F|H'U_i(0,-\infty)|I\rangle\right|^2\delta(E_F-E_I). \tag{1.27}$$

We here introduce the T-matrix as

$$\langle F|H'U_i(0,-\infty)|I\rangle = \langle F|T|I\rangle.$$

The standard Lippman-Schwinger theory shows that the T-operator obeys equations such that [58]

$$T = H' + H'GH' \tag{1.28}$$

$$G = G_0 + G_0H'G, \tag{1.29}$$

where G and G_0 are resolvent operators which are defined as $(E_I - H_{\rm tot}+\mathrm{i}0)^{-1}$ and $(E_I-H+\mathrm{i}0)^{-1}$, respectively. Counting the number of states within a region $\mathrm{d}^3\boldsymbol{q}_2$, and dividing Eq. (1.27) by the incident flux c/V, we have differential cross section as

$$\sigma(F;I) = \left(\frac{Vq_2}{2\pi c\hbar}\right)^2|\langle F|T|I\rangle|^2 \tag{1.30}$$

[4] The quadrupole transition is experimentally observed, for example, as a prepeak in K-XAS of transition metal oxides [53, 54, 55], where the intensity ratio of dipole and quadrupole transition is of order of 100.

for a transition from I to F such that $E_F = E_I$.

Now we proceed to a perturbation theory with respect to H'. In general, electron-photon interaction is much weaker than interaction among electrons. Hence we are allowed to evaluate the T-matrix within the second order of $H_{\rm ep}$ for RXES, whereas electron-electron interaction should be taken to the infinite order. Let us consider the contribution of the Auger effect in the context of perturbation theory. To the second order of $H_{\rm ep}$, we have

$$\langle F|T|I\rangle = \langle F|H_{\rm ep}\tilde{G}H_{\rm ep}|I\rangle, \tag{1.31}$$

where $\tilde{G}$ satisfies

$$\tilde{G} = G_0 + G_0H_{\rm A}G_0 + G_0H_{\rm A}G_0H_{\rm A}\tilde{G}. \tag{1.32}$$

This is nothing but Eq. (1.29) in the $H_{\rm ep} \to 0$ limit. Note that the first term of Eq. (1.28) is not contribute to the T-matrix, and that $H_{\rm A}|F\rangle$=$H_{\rm A}|I\rangle$=0, because both F and I have no core hole to decay.

Exact evaluation of Eq. (1.31) is generally a tough task. To avoid mathematical complications, we introduce Feynman diagrams to represent the series of the T-matrix in Fig. 1.7. If we project out high energy transient states that have Auger electrons more than one, only diagrams (b), (c), ... contribute to give a renormalized intermediate state. Assuming

$$\langle r|H_{\rm A}G_0H_{\rm A}|r'\rangle = \langle r|H_{\rm A}G_0H_{\rm A}|r\rangle\delta_{r,r'}$$

for simplicity, where $|r\rangle$ and $|r'\rangle$ are some states with a core hole and no photon, we have

$$\langle r|\tilde{G}|r\rangle = \frac{1}{E_I - E_r + {\rm i}0}\left[1 + \langle r|H_{\rm A}G_0H_{\rm A}|r\rangle\langle r|\tilde{G}|r\rangle\right] \tag{1.33}$$

from Eq. (1.32), resulting in

$$\langle r|\tilde{G}|r\rangle = \frac{1}{E_I - E_r - \langle r|H_{\rm A}G_0H_{\rm A}|r\rangle}. \tag{1.34}$$

Corresponding to the "open oyster" diagram [59] in Fig. 1.7 (b) or (c), we have "proper" self-energy [60] due to the Auger effect as

$$\begin{aligned}\Sigma^\star_{\rm A}(r) &= \langle r|H_{\rm A}G_0H_{\rm A}|r\rangle \\ &= \sum_m \frac{|\langle m|H_{\rm A}|r\rangle|^2}{E_I - E_m + {\rm i}0} \\ &= \wp\sum_m \frac{|\langle m|H_{\rm A}|r\rangle|^2}{E_I - E_m} - {\rm i}\pi\sum_m |\langle m|H_{\rm A}|r\rangle|^2\delta(E_I - E_m)\end{aligned} \tag{1.35}$$

as depicted in Fig. 1.7 (d). $\wp$ denotes Cauchy's principal value.

Although the energy and r-dependence of the imaginary part of $\Sigma^\star_{\rm A}(r)$ considerably contributes to relatively shallow core level photoemission spectra, for example Ni $3p$-XPS of $NiCl_2$ [61] or $4d$-XPS of heavy rare-earth elements [62], we take it as a given

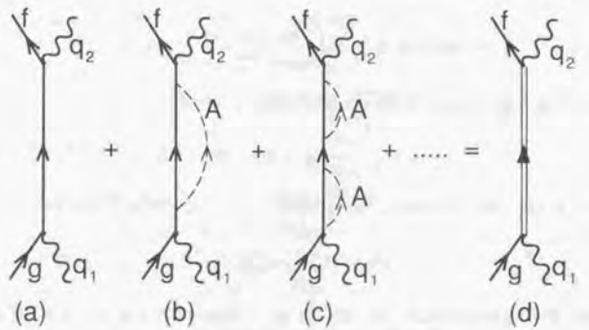

Figure 1.7: Feynman diagrams of the T-matrix expansion. The solid and wavy lines represent the propagation of electronic and photon states, respectively. (a) The ground state $|g\rangle$ absorbs a photon with a wave vector $\boldsymbol{q}_1$, then the intermediate state emits a photon with a wave vector $\boldsymbol{q}_2$, resulting in a final state $|f\rangle$. (b) The same as (a), but an Auger electron "A" is created once in the intermediate state. (c) The same as (a), but an Auger electron is created twice in the intermediate state. The transient states with two Auger electrons are out of the summation. (d) The Auger effect renormalizes the intermediate state.

constant Γ for each system in consideration in this thesis. The real part of $\Sigma_\Lambda^\star(r)$ is regarded to have been included in observed energies. Together with Eq. (1.30), we have

$$\sigma(F;I) = \left(\frac{Vq_2}{2\pi\epsilon\hbar}\right)^2 \left|\langle F|H_{\rm ep}\frac{1}{E_I - H + {\rm i}\Gamma}H_{\rm ep}|I\rangle\right|^2, \tag{1.36}$$

where we have dropped a nonresonant term, which brings about two-photon intermediate states [50].

Substituting the explicit representations of $H_{\rm ep}$ into Eq. (1.36), we reach the final form of the differential cross section of RXES,

$$\sigma(f\boldsymbol{q_2}\boldsymbol{\epsilon}';g\boldsymbol{q_1}\boldsymbol{\epsilon}) = r_0^2\left(\frac{\omega\boldsymbol{q_2}}{\omega\boldsymbol{q_1}}\right)\left|\sum_{\boldsymbol{R}} {\rm e}^{{\rm i}\boldsymbol{q}\boldsymbol{R}} M_{\boldsymbol{\epsilon}'\boldsymbol{\epsilon}}(\boldsymbol{R})\right|^2, \tag{1.37}$$

where $\boldsymbol{q} = \boldsymbol{q_2} - \boldsymbol{q_1}$, and r_0 is the classical radius of electron

$$r_0 = \frac{e^2}{4\pi\varepsilon_0 m_e c^2} \simeq 2.8\times10^{-15}[\mathrm{m}].$$

We assume that the electronic Hamiltonian H is diagonal with respect to the core orbital, i.e.,

$$H_{\rm core} = \sum_{\boldsymbol{R}\xi\sigma} \varepsilon_c c^\dagger_{\boldsymbol{R}\xi\sigma} c_{\boldsymbol{R}\xi\sigma}, \tag{1.38}$$

and that all the core orbitals are filled in $|g\rangle$. ξ stands for a quantum number of the core orbital. Equation (1.38) means that the core orbitals are localized at each lattice site with no transfer to the neighboring sites, the assumption that would be justified in the soft and hard X-ray excitations. As a result, the nondimensional factor $M_{\boldsymbol{\epsilon}'\boldsymbol{\epsilon}}(\boldsymbol{R})$ is represented as

$$M_{\boldsymbol{\epsilon}'\boldsymbol{\epsilon}}(\boldsymbol{R}) = \frac{1}{m_e}\sum_{m,m',m_c,\sigma} (n_c l_c m_c|\boldsymbol{\epsilon}'\cdot\boldsymbol{p}|nlm')(nlm|\boldsymbol{\epsilon}\cdot\boldsymbol{p}|n_c l_c m_c)\times \langle f|c^\dagger_{\boldsymbol{R}m_c\sigma} l_{\boldsymbol{R}m'\sigma} G_0(\Omega) l^\dagger_{\boldsymbol{R}m\sigma} c_{\boldsymbol{R}m_c\sigma}|g\rangle, \tag{1.39}$$

where $G_0(\Omega)$ is re-defined as $(E_I - H + {\rm i}\Gamma)^{-1}$ with $E_I = E_g + \Omega$. We write hereafter the incident and emitted photon energies as Ω and ω, respectively. The local transition amplitude $M_{\boldsymbol{\epsilon}'\boldsymbol{\epsilon}}(\boldsymbol{R})$ obviously depends on Ω, although we did not write it explicitly.

1.3 Some Aspects on Spectral Functions

1.3.1 Momentum conservation law in RXES

Consider an electronic Hamiltonian with the translational symmetry, i.e.,

$$T_r(\boldsymbol{R}) H T_r(\boldsymbol{R})^{-1} = H$$

for any Bravais vector $\boldsymbol{R}$, where $T_r(\boldsymbol{R})$ is the translation operator of the electronic system. Its definition is given by

$$T_r(\boldsymbol{R}) \equiv \exp(\boldsymbol{P}\cdot\boldsymbol{R}/{\rm i}\hbar), \tag{1.40}$$

where $\boldsymbol{P}$ is the momentum operator

$$\boldsymbol{P} \equiv \int {\rm d}^3\boldsymbol{x}\Psi(\boldsymbol{x})^\dagger(-{\rm i}\hbar\nabla)\Psi(\boldsymbol{x}).$$

For the translational Hamiltonian, $|g\rangle$ and $|f\rangle$ can be simultaneous eigenstates of both H and T_r, so that, for $\forall\boldsymbol{R}$, real vectors $\boldsymbol{K}_g$ and $\boldsymbol{K}_f$ exist such that

$$T_r(\boldsymbol{R})|g\rangle = \exp(\boldsymbol{K}_g\cdot\boldsymbol{R}/{\rm i}\hbar)|g\rangle \tag{1.41}$$

$$T_r(\boldsymbol{R})|f\rangle = \exp(\boldsymbol{K}_f\cdot\boldsymbol{R}/{\rm i}\hbar)|f\rangle. \tag{1.42}$$

With these equations we have

$$\begin{aligned}&\langle f|c^\dagger_{\boldsymbol{R}m_c\sigma} l_{\boldsymbol{R}m'\sigma} G_0(\Omega) l^\dagger_{\boldsymbol{R}m\sigma} c_{\boldsymbol{R}m_c\sigma}|g\rangle\\ &= \langle f|T_r(\boldsymbol{R}) c^\dagger_{\boldsymbol{0}m_c\sigma} l_{\boldsymbol{0}m'\sigma} G_0(\Omega) l^\dagger_{\boldsymbol{0}m\sigma} c_{\boldsymbol{0}m_c\sigma} T_r(\boldsymbol{R})^{-1}|g\rangle\\ &= \langle f|c^\dagger_{\boldsymbol{0}m_c\sigma} l_{\boldsymbol{0}m'\sigma} G_0(\Omega) l^\dagger_{\boldsymbol{0}m\sigma} c_{\boldsymbol{0}m_c\sigma}|g\rangle \times \exp\left[{\rm i}(\boldsymbol{K_f} - \boldsymbol{K_g})\cdot\boldsymbol{R}\right],\end{aligned}$$

resulting in

$$M_{\boldsymbol{\epsilon}'\boldsymbol{\epsilon}}(\boldsymbol{R}) = M_{\boldsymbol{\epsilon}'\boldsymbol{\epsilon}}(\boldsymbol{0})\exp\left[{\rm i}(\boldsymbol{K_f} - \boldsymbol{K_g})\cdot\boldsymbol{R}\right]. \tag{1.43}$$

We have just used the fact $[G_0, T_r] = 0$. Now Eq. (1.37) reads

$$\sigma(f\boldsymbol{q_2}\boldsymbol{\epsilon}';g\boldsymbol{q_1}\boldsymbol{\epsilon}) = N^2 r_0^2\left(\frac{\omega\boldsymbol{q_2}}{\omega\boldsymbol{q_1}}\right)|M_{\boldsymbol{\epsilon}'\boldsymbol{\epsilon}}(\boldsymbol{0})|^2\,\delta_{\boldsymbol{q}+\boldsymbol{K_f},\boldsymbol{K_g}}, \tag{1.44}$$

where a well-known relation

$$\frac{1}{N}\sum_{\boldsymbol{R}} {\rm e}^{{\rm i}\boldsymbol{k}\cdot\boldsymbol{R}} = \delta_{\boldsymbol{k},\boldsymbol{0}} \tag{1.45}$$

is used. Equation (1.44) states that the cross section is zero unless $\boldsymbol{q} + \boldsymbol{K_f} = \boldsymbol{K_g}$ is satisfied. This is the wave vector conservation rule of RXES [63] [5]. Equation (1.44) shows an essential aspect of RXES. The origin of this conservation rule is the summation in Eq. (1.37), where the cross section is proportional to a factor quite similar to the definition of the structure factor [64, 65]. If we fixed a core hole to a particular site, the wave vector conservation rule does not hold. This means that the all core orbitals in the system participate in one scattering process, and we can say that the wave vector conservation rule is a result of spatial coherence of the crystal. Intuitively speaking, the electron wave created by a phtoexcitation survives without phase cancellation only

[5] We will briefly discuss an additional SU(2) selection rule in spin space in the next chapter.

when it "fits" to the lattice. In the case of first order optical processes such as XAS or XPS, however, we can calculate spectra by fixing the core hole site, as shown later. This feature makes impurity models, which breaks the translational invariance, appropriate to study the first-order spectra, but not the case in RXES.

On the other hand, $M_{\boldsymbol{\epsilon}'\boldsymbol{\epsilon}}(\mathbf{0})$ reflects an internal symmetry of an atom at the origin. In fact, first, it strictly obeys the dipole selection rule for both X-ray absorption and emission processes, as seen from Eq. (1.39). Second, it reflects a spatial direction of orbitals at $\mathbf{0}$ through the $\boldsymbol{\epsilon}'$- and $\boldsymbol{\epsilon}$-dependence. With these features, RXES should be one of the most useful tools to investigate strongly correlated systems, where interplay between itinerant and localized nature of electrons is realized.

1.3.2 Elastic-inelastic intensity ratio

We first prove a theorem on the elastic scattering.

Theorem 1 If $\boldsymbol{\epsilon}\cdot\boldsymbol{\epsilon}'=0$, then intensity of the elastic scattering such that $m{=}m'$ is zero within the atomic dipole approximation.

Note that the elastic scattering of a system with no electron in the l-shell always satisfies the condition $m{=}m'$. For example, any elastic scattering of $3d$-$2p$ RXES of d^0 compounds or Cu $4p$-$1s$ RXES of cuprates is forbidden when $\boldsymbol{\epsilon}\cdot\boldsymbol{\epsilon}'=0$ according to this theorem. For proof, we define a quantity

$$I_{\boldsymbol{\epsilon}',\boldsymbol{\epsilon}}(m',m)\equiv(n_c l_c m_c|\boldsymbol{\epsilon}'\cdot\boldsymbol{p}|nlm')(nlm|\boldsymbol{\epsilon}\cdot\boldsymbol{p}|n_c l_c m_c). \tag{1.46}$$

Note that $I_{\boldsymbol{\epsilon}',\boldsymbol{\epsilon}}(m',m)$ strictly obeys Wigner-Eckart's theorem [66] of SO(3). We take $\boldsymbol{\epsilon}{=}\boldsymbol{e}_z$ for simplicity, where $\boldsymbol{e}_z$ is the unit vector along z-axis fixed to the electronic system. Since $\boldsymbol{p}{\cdot}\boldsymbol{e}_z{=}p_z$ is the zero component of spherical tensor operators of rank one, the Wigner-Eckart theorem limits m to m_c. However, this condition is never satisfied when $\boldsymbol{\epsilon}\cdot\boldsymbol{\epsilon}'=0$, because $\boldsymbol{\epsilon}'{\cdot}\boldsymbol{p}$ in this case is 1 or -1 component of the spherical tensor operator. Hence $I_{\boldsymbol{\epsilon}',\boldsymbol{\epsilon}}{=}0$ follows in the case that $m{=}m'$. The condition $\boldsymbol{\epsilon}\cdot\boldsymbol{\epsilon}'=0$ is experimentally called "*depolarized*" configuration.

We see from Eq. (1.44) that the cross section is $\mathcal{O}(N^2)$ (order of N^2) as far as $I_{\boldsymbol{\epsilon}',\boldsymbol{\epsilon}}$ and $M_{\boldsymbol{\epsilon}'\boldsymbol{\epsilon}}(\mathbf{0})$ is $\mathcal{O}(1)$. Let us define a nondimensional quantity

$$J_{m'm}(\mathbf{0})\equiv\langle f|c^\dagger_{\mathbf{0}m_c\sigma}l_{\mathbf{0}m'\sigma}G_0(\Omega)l^\dagger_{\mathbf{0}m\sigma}c_{\mathbf{0}m_c\sigma}|g\rangle\times\Gamma,$$

and assume that $I_{\boldsymbol{\epsilon}',\boldsymbol{\epsilon}}$ is $\mathcal{O}(1)$. We first consider a local transition process, which will be realized when Ω is tuned at a state bound to the core hole at $\mathbf{0}$. This contains two cases. One is the elastic scattering process with $m{=}m'$, and the other is (inelastic) scattering involving an intra-site excitation such as intra-site $t_{2g}\to e_g$ excitation depicted in Fig. 1.8. Since the selected intermediate state should have the hole occupation number

of order 1 in the l_m orbital, and moreover the electron occupation number of order 1 in the $l_{m'}$ orbital, $|J_{m'm}(\mathbf{0})|\sim\mathcal{O}(1)$ obviously holds. We have $\mathcal{O}(N^2)$ scattering intensity in these cases thereby.

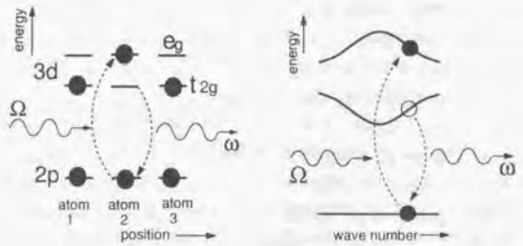

Figure 1.8: Left: Schematic picture of the intra-site excitation. The $2p$-$3d$-$2p$ RXES process is shown for instance. Right: RXES process in a band insulator. There are an empty conduction band, a filled valence band, and a filled core band in the ground state. For both diagrams, Ω and ω represent incident and emitted photon energies, respectively.

As will be explained in § 1.4.4, there are unbound states in the intermediate state even under a strong core hole potential U_c. Utilizing Fourier transformation

$$l^\dagger_{\boldsymbol{k}m\sigma}=\frac{1}{\sqrt{N}}\sum_{\boldsymbol{R}}e^{i\boldsymbol{k}\cdot\boldsymbol{R}}l^\dagger_{\boldsymbol{R}m\sigma}, \tag{1.47}$$

we have another expression of $J_{m'm}(\mathbf{0})$ as

$$J_{m'm}(\mathbf{0})=\frac{1}{N^2}\sum_{\boldsymbol{k}_1,\boldsymbol{k}_2}\langle f|c^\dagger_{\boldsymbol{k}_1 m_c\sigma}l_{\boldsymbol{k}_2 m'\sigma}G_0(\Omega)l^\dagger_{\boldsymbol{k}_2 m\sigma}c_{\boldsymbol{k}_1 m_c\sigma}|g\rangle\times\Gamma,$$

where the wave vector conservation and Eq. (1.38) are implicitly assumed. Since the photoexcited electron is considerably delocalized, we are allowed to neglect U_c in the intermediate state, so that wave number is good quantum number also in the intermediate state. Let us consider an insulator having nearly independent electrons. When the incident photon energy is assigned to make resonance at its absorption edge, $\Gamma G_0(\Omega)\sim -i$ follows, so that

$$J_{m'm}(\mathbf{0})\sim\frac{-i}{N}\sum_{\boldsymbol{k}}\langle f|l_{\boldsymbol{k}m'\sigma}l^\dagger_{\boldsymbol{k}m\sigma}|g\rangle,$$

where we used the fact that both initial and final states have a filled core band, and we implicitly assume a condition

$$\Gamma\ll W, \tag{1.48}$$

where W is a band width of an empty conduction band. For the elastic scattering such that f=g and $m = m'$, the matrix element equals the hole occupation number of l_m orbital in the ground state. Although other orbitals, especially ligand orbitals, strongly contribute to an upper band of the insulator in consideration, the matrix element is still expected to be $\mathcal{O}(1)$, resulting in $|J_{m'm}(\mathbf{0})| \sim \mathcal{O}(1)$.

For an inelastic scattering, there is one electron in a conduction band and one hole in a valence band in a typical final state, as shown in Fig. 1.8 (right), so that a final state $|f\rangle$ gives a nonzero matrix element for a few of $l_{\boldsymbol{k}m'\sigma}l^\dagger_{\boldsymbol{k}m\sigma}|g\rangle$. Consequently, $|J_{m'm}(\mathbf{0})| \sim \mathcal{O}(\frac{1}{N})$ for a specific final state of this kind. While this result leads to a cross section of $\mathcal{O}(1)$, the N dependence of density of states recovers spectral intensity of $\mathcal{O}(N)$. This is because final states of this kind are densely distributed in general in a region [6]. Hence we have N^2 intensity for the elastic scattering, whereas N intensity for nonlocally excited inelastic scattering in this case. The ratio of them diverges in the thermodynamic limit [67, 92].

Experimentally, never is observed the divergence. A part of the reason possibly comes from a finite coherent length of X-rays. If an incident photon is incomplete plain wave, the $N \to \infty$ limit is not realistic, and interference between "fragments" of plain wave may occur, resulting in finite elastic intensity. Another possible reason is associated with Eq (1.48). It is evident that the above estimation is forced to make modifications if $\Gamma \sim W$ or Γ has term-dependence. At any rate, quantitative estimation of the ratio is extremely difficult [7]. We will not discuss the elastic scattering hereafter.

1.3.3 Other spectral functions

Apart from a prefactor, the spectral function of RXES is now written as

$$F_{\mathrm{RXES}}(\omega;\Omega) = \frac{1}{N}\sum_f |\sigma(f\boldsymbol{q_2}\boldsymbol{\epsilon}';g\boldsymbol{q_1}\boldsymbol{\epsilon})|^2\delta(E_f+\omega-E_g-\Omega). \tag{1.49}$$

Similarly, the spectral function of XAS is written as

$$F_{\mathrm{XAS}}(\Omega) = \frac{1}{N}\sum_{m\boldsymbol{R}} |\langle m(\boldsymbol{R})|T^{\mathrm{a}}_{\boldsymbol{\epsilon}}(\boldsymbol{R})|g\rangle|^2\delta(\Omega-E_m+E_g). \tag{1.50}$$

where $|m(\boldsymbol{R})\rangle$ is a final state with a core hole at $\boldsymbol{R}$. Note the assumption Eq. (1.38). Under this assumption, we can delete the position degrees of freedom of a core hole

[6] Because of the assumption of insulator, the elastic line is isolated alone.

[7] Recently, Jiménez-Mier *et al.* reported an estimation of the ratio within a specific model on 3*d*-2*p* RXES of Ti compounds [68]. However, the estimated value sensitively depends in principle on what number of transition paths is taken into consideration. Since they made a drastic approximation that, e.g., the effect of core hole potential is completely disregarded, their statement on the ratio makes little sense.

from F_{XAS}. Since the core hole site is a good quantum number in the final state of XAS,

$$\begin{aligned}\langle m(\boldsymbol{R})|T^{\mathrm{a}}_{\boldsymbol{\epsilon}}(\boldsymbol{R})|g\rangle &= \langle m(\mathbf{0})|T_r(\boldsymbol{R})^\dagger T_r(\boldsymbol{R})T^{\mathrm{a}}_{\boldsymbol{\epsilon}}(\mathbf{0})T_r(\boldsymbol{R})^\dagger|g\rangle \\ &= \langle m(\mathbf{0})|T^{\mathrm{a}}_{\boldsymbol{\epsilon}}(\mathbf{0})|g\rangle \mathrm{e}^{-\mathrm{i}\boldsymbol{K_g}\boldsymbol{R}},\end{aligned}$$

leading the XAS spectral function to

$$F_{\mathrm{XAS}}(\Omega) = \sum_m |\langle m(\mathbf{0})|T^{\mathrm{a}}_{\boldsymbol{\epsilon}}(\mathbf{0})|g\rangle|^2\delta(\Omega-E_m+E_g). \tag{1.51}$$

Let us consider spectral functions of XPS, where a core hole is photoexcited to a high-energy continuum, as explained in § 1.1. Since interaction between the photoelectron and valence electrons is negligible, and the continuum states have nearly all kinds of symmetry, one does not need to handle the photoelectron degrees of freedom explicitly. Apart from a prefactor, we set the transition operator of XPS simply to be

$$T_{\mathrm{p}} = \sum_{\boldsymbol{R}} T^{\mathrm{p}}(\boldsymbol{R}) = \sum_{\boldsymbol{R},m_c,\sigma} c_{\boldsymbol{R}m_c\sigma},$$

leading to the XPS spectral function

$$F_{\mathrm{XPS}}(E_B) = \sum_\mu |\langle\mu(\mathbf{0})|T^{\mathrm{p}}(\mathbf{0})|g\rangle|^2\delta(E_B-E_\mu+E_g), \tag{1.52}$$

where E_B represents the binding energy, and the T_r manipulation as explained above has been used.

NXES is the second-order optical process where a core electron is excited by the incident photon to high-energy continuum well above the absorption edge. An energy interval of the continuum levels is so close that the momentum information of the system is hardly maintained through the NXES process. Therefore, final states with any wave number are allowed. This situation is mathematically realized by fixing the core hole site. The spectral function of NXES is then given by

$$\begin{aligned}F_{\mathrm{NXES}}(\omega) &= \frac{1}{N}\int \mathrm{d}\varepsilon D(\varepsilon)\sum_{f,\sigma}|\langle f|T^*_{\boldsymbol{\epsilon}'}(\mathbf{0})G_0(\Omega-\varepsilon)T^{\mathrm{p}}(\mathbf{0})|g\rangle|^2 \\ &\quad\times\delta(\omega+E_f+\varepsilon-\Omega-E_g),\end{aligned} \tag{1.53}$$

where $D(\varepsilon)$ is the density of states of the continuum level ε, and $G_0(\Omega-\varepsilon) = (E_g+\Omega-\varepsilon-H+\mathrm{i}\Gamma)^{-1}$. We will take $D(\varepsilon)$ as a given constant. Because of the integration over ε, the spectral shape of NXES does not depend on Ω.

1.4 Model Hamiltonians and Their Implications

1.4.1 Impurity Anderson model

The impurity Anderson model which GS proposed for a degenerate $4f$ system is written as

$$H_{\rm IAM} = \sum_{m,\sigma}\left[(\varepsilon_f - U_{fc}n_c)f^\dagger_{m\sigma}f_{m\sigma} + \sum_{\boldsymbol{k}}\left(V_{\boldsymbol{k}}\, f^\dagger_{m\sigma}a_{\boldsymbol{k}\sigma} + \text{H.c.}\right)\right] + U_{ff}\sum_{m>m',\sigma,\sigma'} f^\dagger_{m\sigma}f_{m\sigma}f^\dagger_{m'\sigma'}f_{m'\sigma'} + \sum_{\boldsymbol{k},\sigma}\varepsilon_{\boldsymbol{k}}a^\dagger_{\boldsymbol{k}\sigma}a_{\boldsymbol{k}\sigma} + \varepsilon_c(1-n_c), \quad (1.54)$$

where $f^\dagger_{m\sigma}$ creates a $4f$ electron with an orbital index m and spin component σ, and $a^\dagger_{\boldsymbol{k}\sigma}$ creates a conduction electron with wave number $\boldsymbol{k}$ and spin component σ. ε_f, $\varepsilon_{\boldsymbol{k}}$ and ε_c are one-electron energies for $4f$, conduction electron, and core orbitals, respectively. n_c is the number of core holes. $V_{\boldsymbol{k}}$ is the hybridization strength between $4f$ and conduction electrons. Note that this model exhibits a permutation symmetry such that $m \leftrightarrow m'$. Making full use of this fact implicitly, GS introduced a set of states which have the same permutation symmetry as $4f^0$ state, and successfully discussed core-level spectra of valence-fluctuated systems, as explained before.

To apply this model to transition metal compounds, one should include the anisotropy of orbitals, which breaks the permutation symmetry. A simplified model in which only the nearest-neighbor ligand orbitals are taken into account is often used. We refer to this model as impurity cluster model,

$$H_{\rm ICM} = \sum_{\gamma,\sigma}\left[\varepsilon_{d\gamma}d^\dagger_{\gamma\sigma}d_{\gamma\sigma} + \left(V_\gamma\, d^\dagger_{\gamma\sigma}p_{\gamma\sigma} + \text{H.c.}\right)\right] + \varepsilon_c\sum_{\xi,\sigma}c^\dagger_{\xi\sigma}c_{\xi\sigma} + U_{dd}\sum_{\gamma>\gamma',\sigma,\sigma'} d^\dagger_{\gamma\sigma}d_{\gamma\sigma}d^\dagger_{\gamma'\sigma'}d_{\gamma'\sigma'} - U_{dc}\sum_{\gamma,\xi,\sigma,\sigma'} d^\dagger_{\nu\sigma}d_{\nu\sigma}c^\dagger_{\xi\sigma'}c_{\xi\sigma'}, \quad (1.55)$$

where γ runs over irreducible representations around the impurity atom. $d^\dagger_{\gamma\sigma}$ and $p^\dagger_{\gamma\sigma}$ are creation operators of a d orbital and a ligand molecular orbital, respectively. $c^\dagger_{\xi\sigma}$ is a creation operator of the core orbital with a quantum number ξ. One-electron energies of $\varepsilon_{d\gamma}$ and ε_c are measured with respect to the one-electron energy of the p orbitals. In general, multipole part of Coulomb interaction and spin-orbit interaction are added to $H_{\rm ICM}$ or $H_{\rm IAM}$. Figure 1.9 shows a schematic picture of $H_{\rm ICM}$. We note that there is no transfer between different γ's, and only U_{dd} couples them.

This model describes at least two excitation modes in RXES spectra:

1. intra-site d-d excitations ($10Dq$),
2. CT excitations (Δ or $V_{\rm eff}$),

where we write representative energy scales for each excitation in the brackets. $10Dq$ is crystal field splitting, which is the energy difference typically between $3d(e_g)$ and

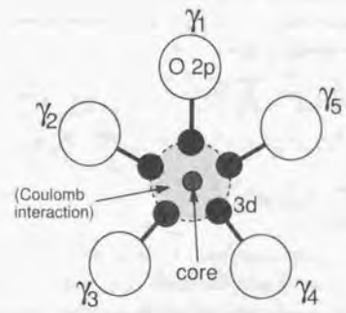

Figure 1.9: Schematic diagram of an impurity cluster model for transition metal insulators. The metal 3d orbital and oxygen 2p molecular orbitals are represented with closed and open circles, respectively. The darkly-shaded smaller circle at the center stands for the core orbital. The Coulomb interactions which correlate different symmetry γ_i each other are represented with the shaded area.

$3d(t_{2g})$ orbitals in a crystal of O_h symmetry. $V_{\rm eff}$ is the effective hybridization energy between metal and ligand molecular orbitals, and generally has a value of order of $\sqrt{N_d}V_\gamma$, where N_d is the number of unoccupied metal orbitals.

An example of intra-site d-d excitations has been shown in Fig. 1.8. Historically, the first theoretical prediction on the observation of intra-site d-d excitation with RXES was given by Tanaka and Kotani in 1993 for d^9 systems [69], which is also nominally d^1 configuration in the hole picture. It was the first theoretical study of RXES as a second-order optical process in the framework of many-body problem [70]. Very recently, Kuiper *et al.* measured Cu $3d$-$3p$ RXES of $Sr_2CuO_2Cl_2$, and observed the intra-site transition of a hole from $3d_{x^2-y^2}$ to $3d_{xy}$, and to $3d_{yz}$ and $3d_{yz}$ [71]. To distinguish between $3d_{xy}$ and $3d_{yz}$ (or $3d_{yz}$), they made use of the angular dependence of Eq. (1.46). This measurement is regarded as a quantitative experimental confirmation of the Tanaka-Kotani theory.

1.4.2 Periodic Anderson model

For systems in which nonlocal screening effects are expected, the relevant start point is the periodic Anderson model

$$H_{\rm PAM} = H_{\rm core} + H_{dp} + H_{dc}.$$

This is the Hamiltonian with which we will investigate core level spectra in this thesis. The first term has already defined in Eq. (1.38). Corresponding to Eq. (1.55), the second and third terms are defined as

$$
\begin{aligned}
H_{dp} &= \sum_{\boldsymbol{R},\nu} \varepsilon_{d\nu} d^\dagger_{\nu\boldsymbol{R}} d_{\nu\boldsymbol{R}} + \sum_{\boldsymbol{r},\mu} \varepsilon_{p\nu} p^\dagger_{\nu\boldsymbol{r}} p_{\nu\boldsymbol{r}} + \sum_{\langle \boldsymbol{r},\boldsymbol{r}'\rangle,\mu,\mu'} \left(T_{pp}\, p^\dagger_{\mu\boldsymbol{r}} p_{\mu'\boldsymbol{r}'} + \text{H.c.} \right) \\
&+ \sum_{\langle \boldsymbol{R},\boldsymbol{r}\rangle,\nu,\mu} \left(T_{pd}\, d^\dagger_{\nu\boldsymbol{R}} p_{\mu\boldsymbol{r}} + \text{H.c.} \right) + U_{dd} \sum_{\boldsymbol{R},\nu>\nu'} d^\dagger_{\nu\boldsymbol{R}} d_{\nu\boldsymbol{R}} d^\dagger_{\nu'\boldsymbol{R}} d_{\nu'\boldsymbol{R}} \qquad (1.56) \\
H_{dc} &= -U_{dc} \sum_{\boldsymbol{R},\nu,\xi} d^\dagger_{\nu\boldsymbol{R}} d_{\nu\boldsymbol{R}} c^\dagger_{\xi\boldsymbol{R}} c_{\xi\boldsymbol{R}}, \qquad (1.57)
\end{aligned}
$$

where $d^\dagger_{\nu\boldsymbol{R}}$ represents a creation operator of a d carrier with a quantum number ν at $\boldsymbol{R}$ site. Similarly, $p^\dagger_{\nu\boldsymbol{r}}$ creates a p carrier with $(\boldsymbol{r},\nu)$, and $c^\dagger_{\xi\boldsymbol{R}}$ a creation operator of a core hole with $(\boldsymbol{R},\xi)$. We denote spin and orbital quantum numbers together by Greek indices ν, μ and ξ. U_{dd} and U_{dc} are on-site Coulomb interaction for d-d and d-core, respectively. Notice the $d^\dagger_{\nu\boldsymbol{R}} p_{\mu\boldsymbol{r}}$ term, where orbitals with different local point group symmetry are no longer decoupled as the case in Eq. (1.55). It makes hard to calculate spectra for systems with an intermediate filling.

This model describes at least four excitation modes. In addition to those of the impurity model,

3. inter-site spin excitations (J),
4. inter-site d-d excitations (U_{dd}),

where J represents the superexchange interaction.

These modes appear in CLS in various phases, depending on filling and excitation process. Let us consider relatively simple cases: d^0 and d^1 fillings. For the former, valence excitations are mainly dominated by only CT excitations. Recall the fact RXES can strongly reflect charge dynamics due to core hole creation, and that its description would be hard within the impurity models. The relatively simple electronic structure of d^0 systems will be rather helpful to elucidate this side of spectra. This is the theme of Chap. 2.

For d^1 systems, all the modes are concerned in principle. In fact, we will show that intra- and inter-site d-d excitations as well as CT excitations are observed in calculated spectra with specific excitation energy dependence. It is interesting to reproduce interplay between intra- and inter-site effects. This subject will be discussed in Chap. 3. For the dependence of inter-site spin excitations in RXES, few studies have been done so far, and it is left for the future problem.

1.4.3 Zhang-Rice singlet

Soon after the spectroscopic methods revealed that dopant holes are primarily on oxygen sites in high-T_c cuprates, Zhang and Rice proposed a picture on the conductivity

in the doped cuprates: A dopant hole forms a local singlet on a CuO_4 square, then it moves over the whole CuO_2 plane [43].

To elucidate their idea, consider a two-hole singlet state, where one hole is localized at a $3d_i(x^2-y^2)$ orbital (i labels a Cu site), and the other is contained in the O $2p$ molecular orbital around the $3d_i$ site. These orbitals are described in the left figure in Fig. 1.10. The molecular orbital which couples with $3d_i$ orbital is

$$
L^\dagger_{i\sigma} = \frac{1}{2} \left(-p^\dagger_{i+\frac{\mathbf{a}}{2}\sigma} - p^\dagger_{i+\frac{\mathbf{b}}{2}\sigma} + p^\dagger_{i-\frac{\mathbf{a}}{2}\sigma} + p^\dagger_{i-\frac{\mathbf{b}}{2}\sigma} \right), \qquad (1.58)
$$

with which we can construct a singlet state

$$
|s_i\rangle = \frac{1}{\sqrt{2}} \left(d^\dagger_{i\uparrow} L_{i\downarrow} - d^\dagger_{i\downarrow} L_{i\uparrow} \right) |0\rangle,
$$

where $|0\rangle$ is the vacuum of holes. Operation of the two-hole spin operator $s^2 = (\boldsymbol{s}_d + \boldsymbol{s}_L)^2$ directly leads to $s^2|s_i\rangle = 0|s_i\rangle$. With rearrangement of a set of Wannier functions, Zhang and Rice derived an effective Hamiltonian, which describes the motion of this kind of singlet state, the Zhang-Rice singlet. Their Hamiltonian is now called the t-J model.

It is amusing that the motion of the Zhang-Rice singlet is directly observed in Cu $2p$-XPS of *undoped* cuprates. When an incident X-ray photon comes into the system, the Zhang-Rice singlet is formed with the following procedure: The photo-created core hole acts as a strong repulsive potential to a $3d$ hole at the same plaquette, then the $3d$ hole escapes from the singular plaquette. The slipped hole goes into another plaquette to form the Zhang-Rice singlet there. In contrast to the photo-doping in the case of valence photoemission, we can call this process "*potential doping*". This subject will be explored in Chap. 4.

1.4.4 Core exciton

In this section, we sketch the core exciton theory with an exactly solvable model. The aim is twofold. First, to supply a basis for the estimation of N-dependence of the RXES cross section under the core hole potential U_c. Second, to give an insight into the core hole effect especially in d^0 systems.

Let us consider a one-dimensional nondegenerate periodic Anderson model under d^0 filling in the limit of $U_{dd}/|\varepsilon_{d\nu} - \varepsilon_{p\mu}| \to \infty$ and $U_{dd}/|T_{pd}| \to \infty$. In this limit, the system is described with a spinless Fermion model without U_{dd}. As far as periodic systems are concerned, the Hamiltonian is decomposed according to wave number k via Fourier transform (Eq. (1.47)), $H = \sum_k h_k$. By diagonalizing each h_k, we have a band structure of the system. There are an empty conduction band and a filled valence band in the ground state under d^0 filling, as well as the filled core band with no energy

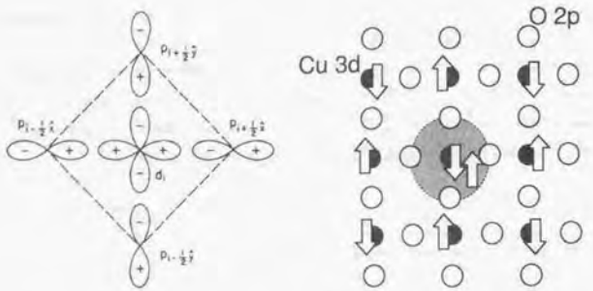

Figure 1.10: Left: Explanation of relative phases between O $2p$ and Cu $3d_{x^2-y^2}$ orbitals [43]. Right: Schematic picture of the hole-doped CuO_2 plane, where a dopant hole forms the Zhang-Rice singlet at the central plaquette. The open and closed circles represent O $2p$ and Cu $3d_{x^2-y^2}$ orbitals, respectively. The arrows represent holes.

dispersion, as shown in Fig. 1.8 (right). As a model of the conduction band, we assume a cosine-type one-dimensional band

$$\varepsilon_k = \eta_0 + 4\gamma \sin^2(k/2)$$

for the first Brillouin zone $-\pi < k \leq \pi$ with given energy constants η_0 and γ. Our spinless Fermion model is now written as

$$H = \sum_k \varepsilon_k a_k^\dagger a_k + H_v - U_c \sum_l a_l^\dagger a_l c_l^\dagger c_l,$$

where $a_k^\dagger$ creates a conduction electron with wave vector k. $a_l^\dagger$ and $c_l^\dagger$ create a conduction electron and a core hole at l site. H_v describes the filled valence band. The energy origin is defined with respect to the core level.

Let us consider the X-ray absorption process in this model. As shown in Eq. (1.51), the only core orbital at a site, say, the origin 0 is sufficient to calculate XAS spectrum. Accordingly, the above Hamiltonian is reduced to a MHD type model,

$$H = \sum_k \varepsilon_k a_k^\dagger a_k + H_v - U_c a_0^\dagger a_0 n_{c0}, \tag{1.59}$$

where n_{c0} is the number of core hole at the origin. Although the transition operator can not be generally written in terms of only $a_k^\dagger$'s, we treat a simplified operator

$$T_s = \sum_l a_l^\dagger c_l = \sum_k a_k^\dagger c_k$$

in place of Eq. (1.20) under the assumption that the polarization vector of the incident photon is parallel to the chain. The second equal sign is due to Fourier transformation. This transition operator creates only one conduction electron in XAS final state (n_e=1). Hence we can set a j-th eigenstate as

$$|\alpha_j\rangle = \sum_k A_{jk} a_k^\dagger |g\rangle$$

without loss of generality. Operating H to this state, we have the Schrödinger equation to determine the coefficients A_{jk} as

$$(\varepsilon_j - \varepsilon_k) A_{jk} = -\frac{U_c}{N} \sum_{k'} A_{jk'},$$

where N is the number of sites. Dividing the both sides by $(\varepsilon_j - \varepsilon_k)$, and summing over k, we have the eigenequation

$$\frac{1}{N} \sum_k \frac{1}{\varepsilon_j - \varepsilon_k} = -\frac{1}{U_c}, \tag{1.60}$$

which is transformed into

$$\int_{-\pi}^{\pi} \frac{dk}{2\pi} \frac{1}{\varepsilon_j - \varepsilon_k} = -\frac{1}{U_c}$$

in the thermodynamic limit. For $\varepsilon_j < \eta_0$, an analytic solution is obtained by using the residue theorem,

$$\varepsilon_0 = \eta_0 + 2\gamma - \sqrt{(2\gamma)^2 + {U_c}^2},$$

where we labeled this solution with $j = 0$. Substituting ε_j with ε_0, we have an eigenstate as

$$A_{0k} = \frac{1}{\sqrt{N}} \sqrt{\frac{U_c}{\lambda}} \left(\frac{U_c}{\lambda - 2\gamma \cos k} \right),$$

where $\lambda = \sqrt{(2\gamma)^2 + {U_c}^2}$. Note that $A_{0k} \to \frac{1}{\sqrt{N}}$ in the limit of $2\gamma/U_c \ll 1$, so that Fourier transformation in Eq. (1.47) shows

$$|\alpha_0\rangle \to a_0^\dagger |g\rangle, \tag{1.61}$$

i.e. a state bound to the core hole. The bound state $|\alpha_0\rangle$ is called *core exciton*.

A graphical representation of Eq. (1.60) shows that other eigenvalues which do not satisfy $\varepsilon_j < \eta_0$ are nearly the same as the unperturbed values ε_k, so that an eigenstate with $\varepsilon_j \simeq \varepsilon_k$ has large amplitude only for the k.

In summary, the XAS final states are classified into two types. One is the core exciton state, which is fairly localized around the core hole. The others are itinerant

states, whose wave functions are quite similar to those of the unperturbed states. As suggested by the formula of Fourier transformation

$$a_k^\dagger = \frac{1}{\sqrt{N}} \sum_l e^{ikl} a_l^\dagger, \tag{1.62}$$

Each of these states has amplitude of order of $\frac{1}{\sqrt{N}}$ at the core hole site.

Since the X-ray absorption process is the intra-site excitation, the more probability to find a conduction electron at the 0 site we have, the more absorption intensity we observe. Comparing Eq. (1.61) with Eq. (1.62), we can roughly estimate the intensity ratio between the above two states as $1 : \frac{1}{N}$, indicating the concentration of intensity at the exciton state. Figure 1.11 schematically shows the XAS spectrum. The same would be true for a more realistic model, although such analytic solution is possibly hard to obtain. This is the basis of the discussion on the N dependence of the RXES cross section in § 1.3.

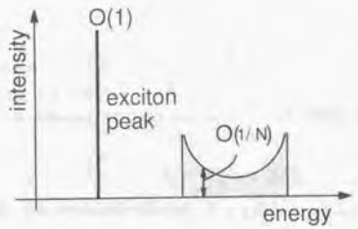

Figure 1.11: Schematic shape of the XAS spectrum. Generally, the continuum has a few sharp peaks due to the van Hove singularity.

1.5 Exact Diagonalization Techniques

1.5.1 Lanczos method

Throughout this thesis, the exact diagonalization method is used to calculate the optical spectral functions. As explained, we are interested in dynamical properties in large-cluster models. Other "less exact" numerical approaches such as Quantum Monte Carlo methods [72] are not suitable for extracting dynamical information.

The newly developed technique, the density matrix renormalization group (DMRG) approach [73], is a renormalization-group-like diagonalization method where the basis

set is optimized to well reproduce lower excited states as the cluster size is extended. DMRG is now accepted as a standard method to calculate static quantities of one-dimensional systems. Although a few attempts have done to extend DMRG to obtain dynamical correlation functions [74, 75], the exact approach based on Lanczos algorithm is currently the only reliable technique for evaluating the second-order spectral functions in higher dimensional systems involving charge excitations [8].

The Lanczos algorithm is a procedure to transform a Hermite matrix $\boldsymbol{H}$ into a tridiagonalized matrix $\boldsymbol{T}$ via a unitary transformation

$$\boldsymbol{T} = \boldsymbol{U}^\dagger \boldsymbol{H} \boldsymbol{U}.$$

We regard $\boldsymbol{H}$ as the Hamiltonian of a given system, and set the order of $\boldsymbol{H}$ to be N_H ($\sim$ a few million). Since the number of nonzero elements of $\boldsymbol{H}$ is much smaller than ${N_H}^2$ in many cases, we can make a subroutine in advance that returns $\boldsymbol{H}\boldsymbol{u}$ for a column vector $\boldsymbol{u}$, using, *e.g.*, JDS method [77].

The Lanczos iterative procedure is as follows: Prepare an arbitrary column vector $\boldsymbol{u}_1$ and $\boldsymbol{v}_1 = \boldsymbol{H}\boldsymbol{u}_1$. Repeat

$$\begin{aligned} a_i &= \boldsymbol{u}_i^\dagger \boldsymbol{v}_i \\ \boldsymbol{w}_i &= \boldsymbol{v}_i - a_i \boldsymbol{u}_i \\ b_{i+1} &= \sqrt{\boldsymbol{w}_i^\dagger \boldsymbol{w}_i} \\ \boldsymbol{u}_{i+1} &= \boldsymbol{w}_i / b_{i+1} \\ \boldsymbol{v}_{i+1} &= \boldsymbol{H}\boldsymbol{u}_{i+1}, \end{aligned}$$

then we have

$$\boldsymbol{T} = \begin{pmatrix} a_1 & b_2 & 0 & \cdots \\ b_2 & a_2 & b_3 & \cdots \\ 0 & b_3 & a_3 & \ddots \\ \vdots & \vdots & \ddots & \ddots \end{pmatrix}$$

and $\boldsymbol{U} = (\boldsymbol{u}_1, \boldsymbol{u}_2, \boldsymbol{u}_3, \cdots)$ [78]. By diagonalizing $\boldsymbol{T}$ to give an eigenvector $\boldsymbol{x}_i$, we have an eigenvector of $\boldsymbol{H}$ as $\boldsymbol{U}\boldsymbol{x}_i$. The eigenvalues of $\boldsymbol{T}$ and $\boldsymbol{H}$ are exactly the same because $\boldsymbol{U}$ is unitary. Note that the number of iteration N_i is often of order of only 100, much smaller than N_H, to obtain the lowest eigenvalue to a given accuracy, say, 0.0001%.

Generally, the limitation of memory size of computers forces us to repeat the whole Lanczos process twice to get the ground state vector $\boldsymbol{g}$. In the first Lanczos process, all of a_i and b_i's but none of $\boldsymbol{u}_i$'s are memorized. Then the tridiagonalized matrix $\boldsymbol{T}$

[8] Very recently, Tanaka developed a DMRG-like approach in a cell-perturbative manner to calculate electron removal spectra of one- or two-dimensional cuprates [76]. It would be possible in principle to extend his method to evaluate spectral functions of the second order processes.

is diagonalized with the Householder method [79] to give the ground state energy E_g and the corresponding eigenvector $\boldsymbol{x}_0 = ({x_0}^1, {x_0}^2, {x_0}^3, \cdots, , {x_0}^{N_i})^{\mathrm{T}}$, where T represents transposition. Then the second Lanczos process is started again with the same initial vector $\boldsymbol{u}_1$. With $\boldsymbol{u}_i$ in each step, we have the ground state as

$$\boldsymbol{g} = {x_0}^1 \boldsymbol{u}_1 + {x_0}^2 \boldsymbol{u}_2 + \cdots + {x_0}^{N_i} \boldsymbol{u}_{N_i}.$$

The Lanczos method is easily extended to obtain a spectral function. Consider to calculate the XPS spectral function. We prepare the ground state vector $\boldsymbol{u}_1 = \boldsymbol{g}$ with the eigenenergy E_g. The Lanczos procedure is carried out with a *final* state Hamiltonian for a given iteration number N_i to give the tridiagonalized matrix $\boldsymbol{T}$. Then $\boldsymbol{T}$ is diagonalized with the Householder method, resulting in a set of eigenvalues and eigenvectors

$$\{E_i, \boldsymbol{f}_i | i = 1, 2, \cdots, N_i\}.$$

To obtain transition amplitude $\boldsymbol{F}_i^{\dagger}\boldsymbol{g}$ for one of the final sates $\boldsymbol{F}_i$, we do not need to explicitly handle the vector $\boldsymbol{u}_i$. Since the transformation unitary matrix $\boldsymbol{U}$ is written as $\boldsymbol{U} = (\boldsymbol{u}_1, \boldsymbol{u}_2, \boldsymbol{u}_3, \cdots, \boldsymbol{u}_{N_i})$, the $\boldsymbol{F}_i$ is expressed as

$$\boldsymbol{F}_i = \boldsymbol{U}\boldsymbol{f}_i = \sum_j \boldsymbol{u}_j {f_i}^j,$$

where ${f_i}^j$ is the j-th element of $\boldsymbol{f}_i$. Hence the transition amplitude now reads $\boldsymbol{F}^{\dagger}\boldsymbol{g} = \boldsymbol{F}^{\dagger}\boldsymbol{u}_1 = ({f_i}^1)^*$, so that

$$F_{\mathrm{XPS}}(E_{\mathrm{B}}) = \sum_i |{f_i}^1|^2 \delta(E_{\mathrm{B}} - E_i + E_g). \tag{1.63}$$

By choosing the initial vector $\boldsymbol{u}_i$ as $T^{\mathrm{a}}|g\rangle$ or $T^{\mathrm{e}}G_0T^{\mathrm{a}}|g\rangle$, the spectral functions of other spectroscopies are numerically obtained in the same manner.

1.5.2 Conjugate gradient method

The other important algorithm to evaluate the spectral function of RXES and NXES is the BiCG (bi-conjugate gradient) algorithm [77, 80]. This is a procedure to evaluate a column vector $\boldsymbol{x}$ such that

$$\boldsymbol{x} = \boldsymbol{A}^{-1}\boldsymbol{b}$$

for a given column vector $\boldsymbol{b}$. The matrix $\boldsymbol{A}$ we are interested in is the type $\boldsymbol{A} = (E_g + \Omega + \mathrm{i}\Gamma)\boldsymbol{1} - \boldsymbol{H}$, which is not Hermite but transposed symmetric $\boldsymbol{A}^{\mathrm{T}} = \boldsymbol{A}$. The unit matrix is written as $\boldsymbol{1}$.

Now the BiCG procedure is as follows: For a given column vector $\boldsymbol{b}$ and an arbitrary column vector $\boldsymbol{x}_0$, set $\boldsymbol{r}_0 = \boldsymbol{b} - \boldsymbol{A}\boldsymbol{x}_0$ and $\beta_{-1} = 0$. Repeat

$$\boldsymbol{p}_n = \boldsymbol{r}_n + \beta_{n-1}\boldsymbol{p}_{n-1}$$

$$\alpha_n = \frac{\boldsymbol{r}_n^{\mathrm{T}}\boldsymbol{r}_n}{\boldsymbol{p}_n^{\mathrm{T}}\boldsymbol{A}\boldsymbol{p}_n}$$
$$\boldsymbol{x}_{n+1} = \boldsymbol{x}_n + \alpha_n \boldsymbol{p}_n$$
$$\boldsymbol{r}_{n+1} = \boldsymbol{r}_n - \alpha_n \boldsymbol{A}\boldsymbol{p}_n$$
$$\beta_n = \frac{\boldsymbol{r}_{n+1}^{\mathrm{T}}\boldsymbol{r}_{n+1}}{\boldsymbol{r}_n^{\mathrm{T}}\boldsymbol{r}_n}$$

for $n = 0, 1, 2, \cdots$ until $\boldsymbol{r}_{n+1}^{\dagger}\boldsymbol{r}_{n+1} \leq \varepsilon \boldsymbol{b}^{\dagger}\boldsymbol{b}$, where ε is a given small real number (usually of order of 10^{-6}), then the resultant vector $\boldsymbol{x}_{n+1}$ is an approximate solution of the equation $\boldsymbol{A}\boldsymbol{x} = \boldsymbol{b}$. Note the discrimination between $^{\mathrm{T}}$ and †. The latter means Hermite conjugate such that $\boldsymbol{r}_{n+1}^{\dagger} = (\boldsymbol{r}_{n+1}^{\mathrm{T}})^*$, where the star means complex conjugate. It is said that mathematically little has been known about convergence behavior of the BiCG algorithm [77]. To the author's experience, the iteration number gets much smaller when $\boldsymbol{A}$ is arranged so that all eigenvalues are positive definite.

To apply these iterative methods to large-clusters, it is essential to reduce the dimension of Hilbert space in advance by making full use of the space group of the whole system, as proposed by Fano, Ortolani and Parola [81]. The largest RXES calculation ever known was done by Tsutsui *et al.* for a 4×4 Hubbard model [82].

1.6 Scope

The motivation of this thesis is to clarify the role of nonlocal effects in RXES. It is roughly divided into two parts. The first part is associated with theoretical explanation of the appearance of the fluorescence-like component in M $3d$-$2p$ RXES of transition metal (M) oxides, which is one of the most important problem in the theoretical study on RXES. This subject is explored in Chaps. 2 and 3. The other part (Chaps. 4 and 5) describes some theoretical aspects of Cu $4p$-$1s$ RXES of cuprates with special attention to the nonlocal screening effect due to the Zhang-Rice singlet formation. The content of each chapter is described somewhat in detail below.

With the aid of numerical calculations with a simplified periodic Anderson model, we discuss the origin of the fluorescence-like component in d^0 systems in Chap. 2. A crucial role of the translational symmetry of the system, the momentum conservation law and electronic correlation is demonstrated. The reason why an analysis with an impurity Anderson model successfully explains the experimental spectra of an f^0 system is qualitatively clarified. This chapter is based on the first proposal of ours on the electronic-origin mechanism of the appearance of the fluorescence-like component [83].

The nondegenerate model calculations in Chap. 2 exhibit relatively weak Raman component for a TiO_2-like system. We demonstrate in Chap. 3 that the *coexistence* between fluorescence-like and Raman components is clearly shown by including orbital

degeneracy into the model. The calculated results well explain the latest experimental data on polarization-resolved Ti $3d$-$2p$ RXES of TiO_2 in spite of the simplicity of the model. Experimentally, the coexistence is observed also in MH systems. We also show in this chapter that the fluorescence-like component appears in the MH systems, and that orbital degeneracy is essential for it. The author believes that the electronic-origin mechanism of the interplay between fluorescence-like and Raman components is established by the investigation in Chaps. 2 and 3.

Chapter 4 is devoted to studying Cu $4p$-$1s$ RXES of Nd_2CuO_4. While the nonlocal screening effect due to the Zhang-Rice singlet formation is known in $2p$-XPS, no one has demonstrated its contribution to RXES so far. We quantitatively prove its essential role in Cu $4p$-$1s$ RXES in this chapter for the first time, and give a clear explanation in terms of spatial extent of CT excitations [84].

Theoretical study on newly-developed experimental techniques such as momentum- or angle-resolved RXES is another interesting theme. This point is discussed in Chap. 5 together with the latest experimental data on Cu $4p_\sigma$-$1s$ RXES of Nd_2CuO_4. We will show that a local transition operator is sufficient to describe the polarization and angular dependence of the "6 eV" CT excitation, and therefore impurity models would work well. We will also point out that RXES with hard X-rays provides momentum-resolved information on electronic structure in k-space.

In the final chapter, a brief summary of conclusions in this thesis is given, and future problems are presented.

Chapter 2

A Model Study on Cluster Size Effects of Resonant X-Ray Emission Spectra

Cluster size dependence of XAS, XPS, and RXES are theoretically studied with a one-dimensional periodic Anderson model, which qualitatively describes effects of the translational symmetry for nominally d^0 (or f^0) compounds such as TiO_2 (CeO_2). It is shown that RXES depends more sensitively on the cluster size than XAS and XPS, so that RXES is a useful probe in studying the duality between itinerant and localized characters of $3d$ or $4f$ electrons. From results calculated by changing the cluster size and parameter values such as d-p hybridization strength, d-d Coulomb interaction etc., it is explained why the experimental Ce $4f$-$3d$ RXES of CeO_2 is well reproduced by calculations with a single-cation impurity Anderson model, but the Ti $3d$-$2p$ RXES of TiO_2 is not well reproduced. [1]

2.1 Introduction

It has been accepted that one of the key concepts to understand electronic properties of strongly correlated systems involving $3d$ or $4f$ orbitals is the duality between localized and itinerant natures of electrons. High-energy spectroscopies have played vital roles to investigate these systems. It is reasonable that XPS and XAS of these systems are considerably well described with the impurity Anderson model including a single cation [6, 85], because a completely localized core electron is involved in these spectroscopies and the core hole acts as a localized attractive potential on the $3d$ or $4f$ electrons. However, since van Veenendaal *et al.* demonstrated importance of

[1] T. Idé and A. Kotani, J. Phys. Soc. Jpn. **67** (1998) 3621-3629.

nonlocal screening effects in analyses of metal $2p$ XPS for NiO [41] and high-T_c compounds [86, 87, 88], those phenomena in which the itinerant property of $3d$ electrons plays an essential role have attracted much attention in this field. As explained in the preceding chapter, it is likely that their itinerancy and their dynamics are well expressed with RXES. The main motivation of this chapter is to investigate how their itinerancy appears in the spectra. It necessarily needs an extended cluster model beyond the single-cation impurity limit.

Experimental data of RXES for graphite [89], Si [90] and diamond [91] have shown that the wave vector conservation rule, which is a mathematical consequence of the itinerancy of valence electrons, plays an important role in RXES spectra. Note that the wave vector conservation rule holds even when core hole effects exist [92]. As explained in the preceding chapter, for transition metal compounds such as TiO_2 [46] and $FeTiO_3$ [47] remarkable spectral features have been observed (Fig. 1.6): in addition to inelastic X-ray scattering peaks whose emitted photon energy moves in parallel with the incident photon energy, giant inelastic spectra are observed at nearly the same energy position for any incident photon energy, and they are connected smoothly to the line shape of NXES as the incident photon energy increases far above the absorption threshold. We named the former the Raman component, and the latter the fluorescence-like component.

A recent experimental and theoretical study on Ti $3d$-$2p$ RXES of gas-phase $TiCl_4$ [93] clearly suggest that the fluorescence-like feature, which is hard to understand with the single-cation impurity model, originates from the solid state effect. We would like to study how the translational symmetry of crystals modifies RXES spectra for the $3d$ system, and to give a physical picture of the X-ray emission process. On the other hand, Nakazawa *et al.* showed that Ce $4f$-$3d$ RXES of CeO_2, which have a $4f^0$ configuration, is well reproduced with an impurity Anderson model [94] despite the apparent similarity in electronic configuration between d^0 and f^0 systems. Their results is shown in Fig. 2.1 for readers' convenience. Now questions come arise: What systems do impurity models cover? Does the translational symmetry give a negligible effect for a system corresponding CeO_2? To study these questions, we adopt a one-dimensional periodic Anderson model without orbital degeneracies as a minimal model having explicit translational symmetry.

The structure of this chapter is as follows: in § 2.2 we explain the model used. In § 2.3 we give results of numerical calculations on XAS, XPS, RXES and NXES for TiO_2-like and CeO_2-like systems. In § 2.4 physical interpretations for these spectra are presented with special attention to role of the wave vector conservation rule. In the last section, we will give a brief summary of the present study.

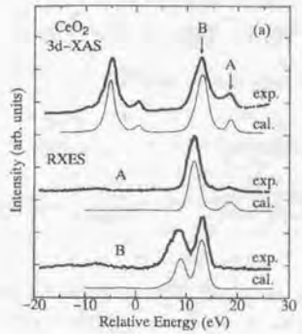

Figure 2.1: Theoretical and experimental XAS and RXES spectra of CeO_2. The thin solid curves and dotted thick curves represent calculated and experimental results, respectively [94]. The calculation was based on an impurity Anderson model. The experimental spectra were measured by Butorin *et al.* [95]. The agreement between calculated and experimental results is good.

2.2 Formulation

We consider a one-dimensional (1D) version of the periodic Anderson model:

$$H = H_{dp} + H_{dc} + H_{\rm core}, \tag{2.1}$$

where

$$\begin{aligned} H_{dp} &= \sum_{l,\sigma} \left[(\Delta + \varepsilon_p)\, d^\dagger_{l\sigma} d_{l\sigma} + \varepsilon_p\, p^\dagger_{l\sigma} p_{l\sigma} \right] \\ &+ \sum_{\langle i,j \rangle} \sum_{\sigma} \left[v\, d^\dagger_{i\sigma} p_{j\sigma} + \text{H.c.} \right] + U_{dd} \sum_{l} d^\dagger_{l\uparrow} d_{l\uparrow} d^\dagger_{l\downarrow} d_{l\downarrow}, \end{aligned} \tag{2.2}$$

$$H_{dc} = -U_{dc} \sum_{l} \left(\sum_{\sigma} d^\dagger_{l\sigma} d_{l\sigma} \right) \left(\sum_{\sigma'} c_{l\sigma'} c^\dagger_{l\sigma'} \right), \tag{2.3}$$

and

$$H_{\rm core} = \sum_{l,\sigma} \varepsilon_c\, c^\dagger_{l\sigma} c_{l\sigma}. \tag{2.4}$$

In the above equations, $d^\dagger_{l\sigma}$ ($p^\dagger_{l\sigma}$) is a creation operator of an electron of σ ($\uparrow$ or $\downarrow$) spin on the d (p) site in l-th unit cell, Δ is the charge-transfer energy between d and p orbitals, U_{dd} is the on-site d-d Coulomb correlation energy, and U_{dc} is the intra-atomic

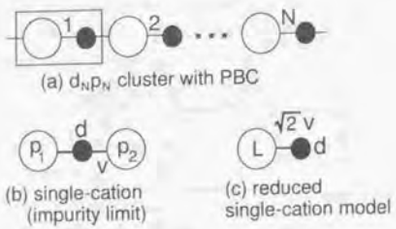

Figure 2.2: Geometry of the system. The closed circles represent d and core orbitals, and the open circles represent p orbitals. (a) The multi-cation $d_N p_N$ system with periodic boundary condition. The rectangle indicates a unit cluster of the system. (b) The single-cation ($d_1 p_2$) model with *open* boundary condition. This is used as a reference system representing the smallest cluster with a single cation. (c) The reduced single-cation model, where L is a linear combination of the two p orbitals in (b) such as $L^\dagger_\sigma = (p^\dagger_{1\sigma} + p^\dagger_{2\sigma})/\sqrt{2}$, resulting in the value $\sqrt{2}v$ of d-L transfer energy.

core hole potential. One-electron energy of the p orbitals is represented with ε_p. $c^\dagger_{l\sigma}$ ($c_{l\sigma}$) is a creation (annihilation) operator of a core electron with one-electron energy ε_c. Geometry of the system is shown in Fig. 2.2. We set the number of valence electrons in the ground state as $2N$ for $d_M p_N$ system, and assume the z-component of the total spin S_z to be zero. Note that our model explicitly comprises both U_{dd} and U_{dc}, which are essential to have realistic discussion on *both* XAS and RXES [49].

The $d_1 p_2$ cluster with *open* boundary condition (Fig. 2.2 (b)) is used as a reference system representing the smallest cluster with a single cation (or the impurity Anderson model), and large-cluster effects are studied using $d_N p_N$ clusters with the *periodic* boundary condition (Fig. 2.2 (a)) by comparing the results calculated with different N (also with the $d_1 p_2$ system).

The second term in Eq. (2.2) describes nearest-neighbor d-p hopping processes. Although the present model does not explicitly include orbital degeneracies, we take them into account by estimating the d-p hopping energy v as

$$v = \frac{1}{2}\sqrt{4V(e_g)^2 + 6V(t_{2g})^2}, \tag{2.5}$$

where $V(e_g)$ and $V(t_{2g})$ are hybridization strengths of the TiO_6 cluster model [49], so that we have the same bonding-antibonding separation in the final state of RXES as that of the TiO_6 cluster model. We explain the derivation in Appendix.

Okada and Kotani [49] used parameter values $V(e_g)$=3.0 and $V(t_{2g})$=−1.5, from

which we have v=3.5 (in units of eV). Other parameters are chosen to be the same as their estimation: Δ=4.0, U_{dd}=4.0 and U_{dc}=6.0 (in eV). These will be referred to as "TiO_2-like" parameters.

We have regarded the d, p and core orbitals as Ti $3d$, O $2p$ and Ti $2p$ orbitals. The Hamiltonian described above can also be used for Ce $4f$-$3d$ RXES spectra of a "CeO_2-like" system by regarding d, p and c as Ce $4f$, O $2p$ and Ce $3d$ orbitals, respectively. Since the impurity Anderson model with local SO(3) symmetry has well reproduced Ce $3d$ XAS spectra [94, 96], the f-p hybridization strength mapped onto 1D Hamiltonian should be simply given by $v = \sqrt{14}V/2$, where 14 is the degeneracy of $4f$ state. Considering the results by Jo and Kotani [96] and Nakazawa *et al.* [94], for "CeO_2-like" calculations we use a parameter set of Δ=1.5, U_{ff}=10.0, U_{fc}=13.0, and v= 1.5 eV.

For our 1D model, the transition operators of the photon absorption and emission process in the dipole approximation are quite simplified as

$$T_{\rm a} = \sum_l e^{iq_1 l} \sum_\sigma d^\dagger_{l\sigma} c_{l\sigma} \tag{2.6}$$

and

$$T_{\rm e} = \sum_l e^{-iq_2 l} \sum_\sigma c^\dagger_{l\sigma} d_{l\sigma} \tag{2.7}$$

in place of Eqs. (1.22) and (1.23). q_1 is the wave number of an incident photon and q_2 an emitted photon [2]. Since we are interested in core level spectra in the soft X-ray regime, the photon wave numbers q_1 and q_2 are taken approximately as zero.

With these operators, the transition operator of RXES is given by

$$\begin{aligned} T(\Omega) &\equiv T_{\rm e} G_0(\Omega) T_{\rm a} \\ &= \sum_{l\sigma} c^\dagger_{l\sigma} d_{l\sigma} G_0(\Omega) d^\dagger_{l\sigma} c_{l\sigma}, \end{aligned} \tag{2.8}$$

where $G_0(\Omega)$ is the resolvent operator defined by $G_0(\Omega) = (\Omega + E_g - H + i\Gamma)^{-1}$, E_g being the energy of the ground state $|g\rangle$. Now the transition amplitude of the RXES process from $|g\rangle$ to a final state $|f\rangle$ is given by

$$U_{g\to f}(\Omega) = \sum_l \sum_{n=0,1} \langle f | T_r(l) (P_s)^n c^\dagger_{0\sigma} d_{0\sigma} G_0(\Omega) d^\dagger_{0\sigma} c_{0\sigma} | g \rangle \times K_g(l) (P_{s,g})^n, \tag{2.9}$$

where $K_g(l)$ is the eigenvalue of the ground state for the translation operator $T_r(l)$ defined in Eq. (1.40). P_s is the spin-flip operator defined by

$$P_s d_{l\uparrow} P_s^{-1} = d_{l\downarrow}$$

[2] We have disregarded the geometrical (angular dependent) factor. In realistic three-dimensional systems, it is quite important for understanding experimental RXES spectra. For effects of the angular dependence on RXES, see, *e.g.*, Ref. [97]. We will explore angular and polarization dependence of RXES in Chap. 5.

etc., and $P_{s,g}$ is its eigenvalue of the ground state. Since T_τ and P_s commute with H, and moreover they commute each other, one can always take the ground state as an eigenvector of these operators. T_τ and P_s are also commute with $T(\Omega)$, so that the eigenvalue of each operators is conserved between $|g\rangle$ and $|f\rangle$. To evaluate the amplitude numerically, one needs to carry out the operation of T_τ and P_s in Eq. (2.9). The former is associated with the wave vector conservation rule, which reflects a spatial coherence of crystal [98], as explained in § 1.3. The latter is associated with the well-known SU(2) rotational symmetry in *spin* space [99], the degrees of freedom to choose the quantization axis of spin. Note that the SU(2) selection rule limits the final state more stringently than the simple S_z conservation rule does. This fact is easily understood by considering a two-site d-p model with two electrons. Within $S_z = 0$, we have a triplet state

$$\frac{1}{\sqrt{2}}\left(d_\uparrow^\dagger p_\downarrow^\dagger + d_\downarrow^\dagger p_\uparrow^\dagger\right)|0\rangle,$$

and one of singlet states

$$\frac{1}{\sqrt{2}}\left(d_\uparrow^\dagger p_\downarrow^\dagger - d_\downarrow^\dagger p_\uparrow^\dagger\right)|0\rangle,$$

as well as trivial singlet states $d_\uparrow^\dagger d_\downarrow^\dagger|0\rangle$ and $p_\uparrow^\dagger p_\downarrow^\dagger|0\rangle$. The triplet state has an eigenvalue of $P_s = 1$, whereas all the singlet states $P_s = -1$. Hence the omission of P_s in Eq. (2.9) generally leads to a breakdown of the conservation rule as to P_s, and therefore causes incorrect spectra which do not satisfy the SU(2) selection rule.

After all, RXES spectral function is calculated with the transition amplitude Eq. (2.9) as

$$F_{\mathrm{RXES}}(\Omega,\omega) = \frac{1}{N}\sum_{f\neq g}|U_{g\to f}(\Omega)|^2\delta(\omega-\Omega+E_f-E_g), \tag{2.10}$$

where ω is the emitted photon energy and we introduce the normalization factor $1/N$ in order to compare systems of different cluster size.

2.3 Calculated Results

2.3.1 XPS spectra

We show XPS spectra for various cluster sizes with the TiO_2-like and the CeO_2-like parameters in Fig. 2.3. The calculated line spectra are convoluted with a Lorentzian function of width 1.0 eV (HWHM) corresponding to the lifetime broadening of the core hole, as well as experimental resolution.

The XPS spectra for the TiO_2-like parameters shown in Fig. 2.3 (a) have roughly two-peak structure with a strong main peak and a weak satellite. For larger cluster sizes, we observe that a few very weak peaks come arise between them. In the impurity

limit (d_1p_2), the main peak corresponds to the bonding state between $\underline{c}d^0$ and $\underline{c}d^1\underline{L}$ configurations [49], where $\underline{L}$ and $\underline{c}$ represent core and ligand holes, respectively. The satellite peak corresponds to the antibonding state. The small cluster-size dependence suggests that the main and satellite peaks could be characterized by the above local charge-transfer excitation also for larger cluster sizes.

On the other hand, clear three peaks are observed in the XPS spectra for the CeO_2-like parameters (Fig. 2.3 (b)), corresponding to three configurations of $\underline{c}f^0$, $\underline{c}f^1\underline{L}$ and $\underline{c}f^2\underline{L}^2$. The three-peaked structure is experimentally observed in Ce $3d$-XPS [101], and well reproduced with impurity Anderson models [94, 96]. The striking difference between the TiO_2-like and CeO_2-like systems originates from, first, the smaller values of v/U_{ff} and v/U_{fc}, and second, the negative value of $\Delta + U_{ff} - U_{fc}$ [94]. As the cluster size increases, we have slightly broader and more asymmetric shapes for the peaks in the lowest and the second-lowest binding energies. However, the global structure is considerably well reproduced with the single-cation cluster f_1p_2.

2.3.2 XAS, RXES and NXES spectra for TiO_2-like parameters

Figures 2.4 (a)-(c) show XAS, NXES and RXES spectra for the TiO_2-like parameters in d_1p_2, d_3p_3 and d_6p_6 clusters. The value of Γ for NXES and RXES is taken as 0.4 eV [3], and the Lorentzian convolution with width 1.0 eV (HWHM) is made for all the spectra, as in the case of XPS. To compare RXES spectra for various Ω's, each of original calculated spectra is magnified by a rate indicated as " $\times$ 10" in the figure.

In the case of the d_1p_2 system, we see two-inelastic peaks, each of which moves in parallel with the incident photon energy Ω, i.e. exhibits only the Raman component. The first (higher ω) peak corresponds to a single-electron charge-transfer excitation, whereas the second one to a two-electron charge transfer state with dominant $d^2\underline{L}^2$ weight. It is rather appropriate to call the former the antibonding state between d^0 and $d^1\underline{L}$ configurations, because its energy separation from the elastic line is not ruled by Δ but mainly v. These inelastic peaks are necessarily *local* charge transfer excitations, and there is no room for fluorescence-like components.

In going from the d_1p_2 to d_3p_3 clusters, however, we find some inelastic scattering peaks which do not follow the change of the incident photon energy Ω. For the d_6p_6 cluster, the energy ω of main RXES peaks does not follow Ω but is rather constant, and it oscillates around the constant energy with the change of Ω, exhibiting the fluorescence-like behavior.

The line shape of NXES also shows, in Fig. 2.4, considerable dependence on the

[3] We have explicitly related Γ to the Auger decay process in Eq. (1.35). In addition, we have to consider at least two factors to evaluate Γ: The experimental resolution of the incident X-ray, and finite energy interval of eigenstates due to finite cluster size.

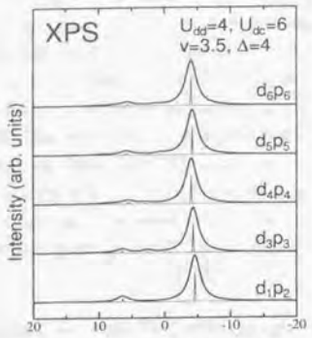

(a) TiO_2-like parameters

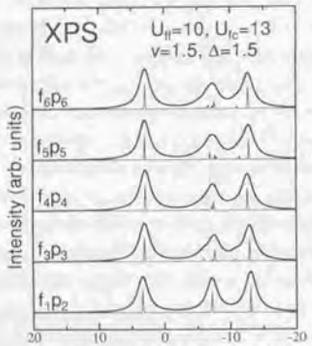

(b) CeO_2-like parameters

Figure 2.3: XPS spectra calculated with various cluster sizes for (a) TiO_2-like and (b) CeO_2-like parameters.

cluster size: A single peak is observed for the NXES of the d_1p_2 cluster, but it splits into two peaks for the d_3p_3 cluster, and the relative intensity of the two peaks changes for the d_6p_6 cluster.

2.3.3 XAS, RXES and NXES spectra for CeO_2-like parameters

Figures 2.5 (a)-(c) show XAS, RXES and NXES spectra with the CeO_2-like parameters for various sizes of the cluster. We see that the XAS spectra have two-peak structure. The main and satellite peaks correspond to the bonding and anti-bonding states, respectively, between $\underline{c}f^1$ and $\underline{c}f^2\underline{L}$ configurations. The cluster size dependence of XAS is quite small, and we only recognize, with increasing cluster size, a slight increase of the spectral intensity in the region between the main peak and the satellite.

The cluster size dependence of RXES for the CeO_2-like system is much smaller than that of the TiO_2-like system, and the energy of the main inelastic scattering feature follows the change of Ω even in the case of large clusters. Apart from the incident photon energy 1, the single-cation model calculation shows a strong inelastic peak, which corresponds to a single charge-transfer excitation. This peak shifts in parallel with Ω, exhibiting the Raman component. With increasing cluster size, the corresponding line spectrum shows a fine spectral splitting into some line spectra, so that this inelastic structure is broadened. Comparing the results calculated with f_1p_2 and f_6p_6 clusters, we see that the single-cation model is a good approximation for describing the RXES except for the incident photon energy 1, for which we will give some discussion in the next section.

The NXES spectrum with f_1p_2 cluster has two peaks, corresponding to the bonding and anti-bonding states between $f^0\underline{L}$ and $f^1\underline{L}^2$ configurations in the final state. With increasing cluster size, the lower energy peak is more broadened, but we observe much smaller dependence on the cluster size compared with the TiO_2-like system.

2.4 Discussion

2.4.1 Applicability of the single-cation model

According to Fig. 2.3, it is found that the cluster size dependence is extremely small for the calculated XPS spectra of both the TiO_2-like and CeO_2-like systems. While the XAS spectra shown in Figs. 2.4 and 2.5 depend on the cluster size slightly more than XPS, the dependence is still extremely small. This fact suggests that the single-cation model can well describe XPS and XAS, which are typical examples of the first-order optical process. Thereby we justify previous theoretical analyses of Ti $2p$-XPS and $2p$-XAS of TiO_2 [49], as well as Ce $3d$-XPS and $3d$-XAS of CeO_2 [94, 96], with im-

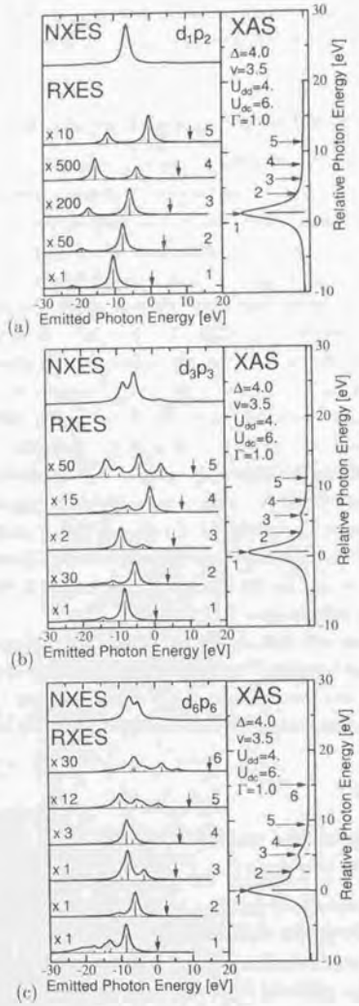

Figure 2.4: Calculated XAS and RXES spectra for the TiO_2-like parameters with (a) d_1p_2, (b) d_3p_3 and (c) d_6p_6 clusters. NXES spectra are also shown on the top of the RXES curves. The arrows indicate energy positions of the incident photon.

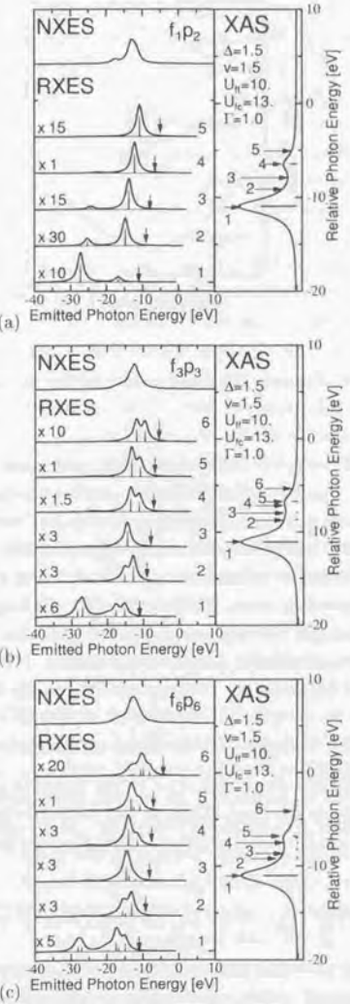

Figure 2.5: XAS and RXES spectra for the CeO_2-like parameters with (a) f_1p_2 (upper), (b) f_3p_3 (lower left) and (c) f_6p_6 (lower right) clusters. See the caption for Fig. 2.4.

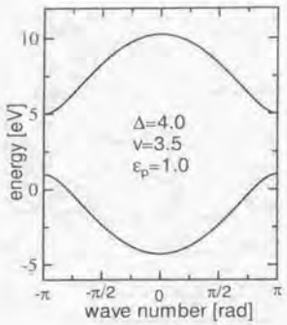

Figure 2.6: One electron energy dispersion in the absence of U_{dd} and U_{dc}. Parameters used are indicated in the panel.

purity models. In addition, for RXES and NXES, it is shown that the single-cation model works as a good model for the CeO_2-like system, where only the Raman component appears. However, it is demonstrated that the cluster size dependence is greatly important for the TiO_2-like system. While the experimentally observed fluorescence-like spectra in d^0 systems[46, 47] are by no means reproduced with the single-cation model, we observe the fluorescence-like behavior with the large-cluster model. This result definitely means that the appearance of the fluorescence-like spectra is a direct consequence of the translational symmetry of the system. Detailed discussion on the origin of the cluster size dependence of RXES will be given in the next subsections.

2.4.2 Fluorescence-like spectra in large cluster models

In order to understand the cluster size effect in the TiO_2-like system, it is instructive to study the situation in the limit of $U_{dd} = U_{dc} = 0$. In this case, the initial and final states of RXES are described exactly with one-electron Bloch states with energy dispersion (Fig. 2.6):

$$\varepsilon^{\pm}(k) - \varepsilon_p = \frac{\Delta}{2}\left(1 \pm \sqrt{1 + (4v/\Delta)^2 \cos^2(k/2)}\right). \tag{2.11}$$

Figure 2.7 shows XAS and RXES spectra for the d_6p_6 cluster in the limit of U_{dd}=U_{dc}=0. The number of k-points in the first Brillouin zone of the d_6p_6 system is six, i.e. $\{0, \pm\pi/3, \pm 2\pi/3, \pi\}$, and the number of the excited electron energies is four. In accordance with these four points, the XAS spectrum displays four lines.

The Ω-dependence of RXES spectra in Fig. 2.7 (solid curves), which is unlike the Raman behavior, is a consequence of the k-conservation rule. Close inspection shows that the inelastic spectrum for any excitation energy consists of three lines. These correspond to states with an electron-hole pair in $\{0, \pm\pi/3, \pm 2\pi/3\}$, from lower to higher energy. When Ω is tuned to 2, for example, a conduction electron at $k = \pm 2\pi/3$ is resonantly selected in the intermediate state. Then the resultant final state has an electron-hole pair at $k = \pm 2\pi/3$ according to the k-conservation rule. Similarly, Ω at 3 (4) leads to an electron-hole pair at $k = \pm\pi/3$ ($k = 0$) in the final state. The valence (conduction) band at $k = \pi$ is of pure p (d) character as suggested by Eq. (2.11). Hence the final state with an electron-hole pair in π has no contribution to the RXES spectra within the intra-atomic transition model as shown in Eq. (2.7), and the inelastic scattering process is necessarily virtual one for the incident photon energy 1.

If we fix a core hole site in the intermediate state, the k-conservation rule breaks down. RXES spectra calculated with a fixed core hole site are shown in Fig. 2.7 with dashed curves. In this case, the spectral shape of RXES is the same as that of NXES. This is because the excited conduction electron has no contribution to the RXES spectral shape, so that the situation is the same as NXES.

These results suggest the origin of the cluster size effect in the TiO_2-like system. If the cluster size is small, an excited conduction electron is necessarily localized and makes an active contribution to the X-ray emission process. In this case, the emitted photon energy shifts in parallel with the incident photon energy. However, when the cluster size is large, we have some intermediate states in which the excited conduction electron state is extended in space as in the case of U_{dd}=U_{dc}=0. Thereby the photoexcited electron can be dissipated from the unit cluster with a core hole to the surrounding system. If this dissipation completely occurs in the intermediate state, the X-ray emission process necessarily resembles NXES, then the fluorescence-like spectra come arise. The dependence of the fluorescence-like spectra on Ω is expected to come from the k-conservation rule within the present model (see §2.4.3).

Effects of finite values of U_{dd} and U_{dc} are also important in the TiO_2-like system. In order to see the effect of U_{dc}, calculated RXES spectra with U_{dd}=0 but U_{dc}=6.0 eV are shown in Fig. 2.8. In the XAS spectrum we observe a strong main peak 1, which corresponds to a bound state between the core hole and an electron excited from the core level, i.e. the core exciton [4]. Comparison of Fig. 2.7 and Fig. 2.8 shows that the RXES spectra are more broadened and exhibit new fine structures because of U_{dc}, which causes excitations with more than one electron-hole pairs in the final state, although the final state Hamiltonian is independent of U_{dc}. However, the RXES spectra of 2, 3 and 4 in Fig. 2.8 are found to resemble those in Fig. 2.7, and this suggests that

[4] See the discussion in § 1.4.4. For an original paper, see Ref. [100].

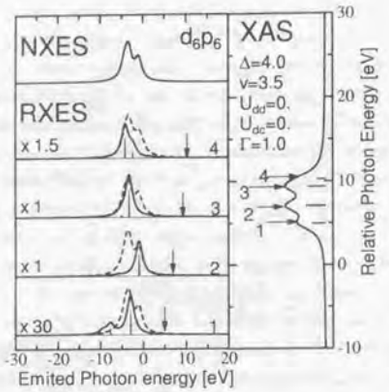

Figure 2.7: RXES spectra in the free electron limit $U_{dd} = U_{dc}$=0 (solid line). Parameters other than U_{dd} and U_{dc} are the same as the TiO_2-like ones. The dashed curves represent core-fixed RXES spectra. See the caption for Fig. 2.4.

these intermediate states have somewhat common characters with spatially extended conduction electron states.

It appears that a weak peak located at the highest energy ω shifts in parallel with Ω, but this occurs as a result of the finite size N [5].

When we introduce a finite value of U_{dd}, occurrence of doubly occupied orbital states is considerably suppressed, and then the RXES in Fig. 2.8 is changed to that in Fig. 2.4 (c). The RXES spectral broadening in Fig. 2.8 is somewhat suppressed in Fig. 2.4 (c), because of the suppression of more than one electron hole pairs in the final state. However, the effect of U_{dd} is not very strong except for the case of 1, because the occupation number of d electrons is small in most states of the TiO_2-like system.

Compared with the TiO_2-like system, the cluster size dependence of RXES in CeO_2-like system is much smaller because of the smaller value of the hybridization v.

[5]Although the statement that a finite cluster size is likely to excessively highlight this peak is true within the present model, it may be questionable whether or not it holds in realistic systems having orbital degeneracy. The experimentally observed Raman component involves nonbonding states (see § 2.4.4) as well as the antibonding state, and the intensity ratio between the Raman and fluorescence-like components strongly depends on how many states we have in a unit cluster, as will be discussed in the next chapter.

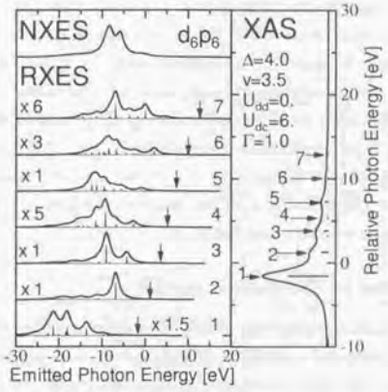

Figure 2.8: Role of the core hole potential U_{dc} in RXES spectra. Parameters other than U_{dd} are the same as the TiO_2-like ones. See the caption for Fig. 2.4.

2.4.3 Role of the k-conservation rule

To study effects of the k-conservation rule in TiO_2-like and CeO_2-like systems, we calculate RXES spectra by fixing the core orbital on a single site and compare them with those including the translational symmetry of core orbitals (denoted as "coherent spectra"). The results are shown in Fig. 2.9. The TiO_2-like spectra in Fig. 2.9 (a) show clear difference between the fixed core-site and coherent spectra. The fixed core-site spectra are considerably broader than the coherent ones for the incident photon energy of 2, 3 and 4. This is clearly attributed to the *k-non*conserving nature of the fixed core-site model. Thus, the role of the k-conservation rule is (1) to narrow the inelastic peak width, and (2) to fluctuate their peak position around that of NXES spectra.

Note that the RXES spectral shape depends on the incident photon energy even with the core-fixed k-nonconserving model. This is in strong contrast to the case of U_{dd}=U_{dc}=0 (Fig. 2.7). Because of finite values of U_{dd} and U_{dc}, the photo-excited conduction electron in the intermediate state cannot be a single Bloch state, and some rearrangement between the conduction and valence electron states occurs in going from the intermediate to the final states. Therefore, the origin of the dependence of the fluorescence-like spectra on the incident photon energy is partly the effect of the k-conservation rule and partly the effect of U_{dd} and U_{dc} [6].

[6]We discuss the contribution of crystal field splitting in the next chapter.

According to Fig. 2.9 (b), there is little difference between the fixed core-site and coherent RXES spectra for the CeO_2-like parameters, although close inspection shows that we have slightly broader spectral shapes with the fixed core-site model. For the CeO_2-like system, the quasi-particle bandwidth is of the same order as the lifetime in the final state. Furthermore the small value of v/U_{fc} makes the intermediate state almost localized. Then clear cluster size effects are not observed. The fact that the fixed core-site and coherent spectra are almost the same demonstrates the reason why the analyses of Ce $4f$-$3d$ RXES with the impurity Anderson model have successfully reproduced the experimental result [94].

2.4.4 Limitation of the present model

We have discussed qualitatively the cluster size effect of RXES in TiO_2 and CeO_2. In order to make a quantitative study, it is necessary to improve the model. Firstly, the atomic arrangement should be developed from the 1D chain to a 3D model that is more realistic. Secondly, the orbital degeneracies of d (or f) and p states should be taken into account. As shown in Appendix, we have introduced the effective hybridization v, in which effects of orbital degeneracies on the hybridization between d^0 and $d^1\underline{L}$ are taken into account. With this effective hybridization, however, effects of orbital degeneracies on the hybridization between $\underline{c}d^1$ and $\underline{c}d^2\underline{L}$ configurations in the intermediate state cannot be well described. Furthermore, the effects of orbital degeneracies are essential in the calculation of RXES for the incident photon energy tuned to the main XAS peak. As shown by Nakazawa *et al.* [94], the main inelastic RXES spectra in resonance with the XAS main peak of CeO_2 originate from the nonbonding $f^1\underline{L}$ final states, instead of the antibonding state between f^0 and $f^1\underline{L}$ configurations. The nonbonding final states occur only by taking explicitly into account the orbital degeneracies. The situation is also the same for TiO_2. In this sense, the present calculation of RXES for the case I is not realistic. In the next chapter, we will discuss the cluster size dependence with degenerate models to remove this limitation.

2.5 Conclusions

We have numerically studied large-cluster effects on XPS, XAS, NXES and RXES spectra. The model we have used is a one-dimensional nondegenerate periodic Anderson model, which is a minimal model having the explicit translational symmetry. It qualitatively describes those spectra of d^0 and f^0 compounds. Following results have been obtained.

Firstly, we showed that the cluster size dependence is extremely suppressed for the first order optical process, XPS and XAS. It suggests that an impurity model is

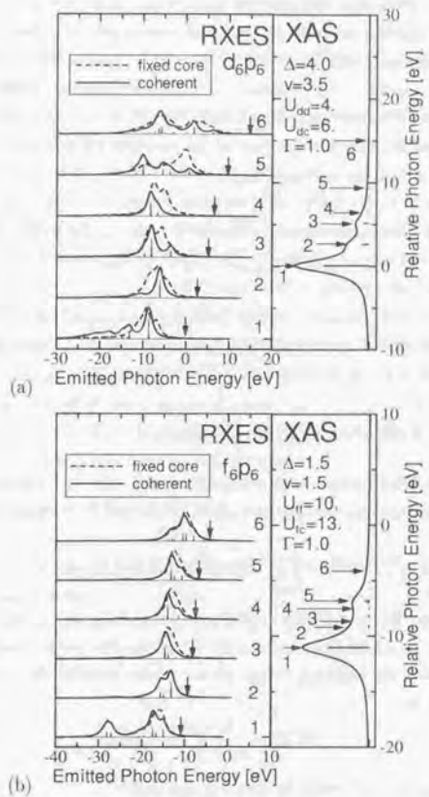

Figure 2.9: Comparison between fixed core-site and coherent calculations of RXES spectra for the (a) TiO_2-like and (b) CeO_2-like systems with six unit clusters. The fixed core-site spectra are represented with dashed lines, and the coherent ones with solid lines. See the caption for Fig. 2.4.

applicable to analyses of these spectra, in contrast to the second-order optical process, RXES and NXES.

Secondly, for TiO_2-like systems, we numerically demonstrated the occurrence of fluorescence-like spectra because of the large-cluster effect. Their behavior is qualitatively consistent with the Ti $3d$-$2p$ RXES experiment of TiO_2. The origin of the fluorescence-like spectra is the existence of spatially extended states of a conduction electron in the intermediate state.Apart from the effects due to orbital degeneracy, the dependence of fluorescence-like spectra on the incident photon energy originates from the k-conservation rule, as well as from the effects of U_{dd} and U_{dc}.

Thirdly, for the CeO_2-like system we have shown that the large-cluster effects in RXES spectra are fairly suppressed, compared with the TiO_2-like system, because of the smaller hybridization strength v. The effect of the translational symmetry is the broadening of inelastic peaks.

Finally we pointed out that explicit orbital degeneracies should be taken into account to describe RXES spectra in resonance with the XAS main peak in d^0 and f^0 systems. This subject will be discussed in the next chapter.

Appendix: Effective Hybridization

In a TiO_6 cluster model with local O_h symmetry and with full orbital degeneracies, the Hamiltonian of hybridization between Ti $3d$ orbitals and O $2p$ ligand molecular orbitals is given by

$$H_1' = \sum_{\Gamma,m,\sigma} \left[V(\Gamma)\, d^\dagger_{\Gamma m\sigma} p_{\Gamma m\sigma} + \text{H.c.} \right], \tag{2.12}$$

where Γ runs over two irreducible representations of O_h, i.e. e_g and t_{2g}, and m distinguishes the 2- or 3-fold degeneracies of them. On the other hand, in the impurity limit (Fig. 2.2 (b)), the hopping energy of our model satisfies $2v = \langle d^0|H|d^1\underline{L}\rangle$, where $|d^0\rangle = L^\dagger_\uparrow L^\dagger_\downarrow|0\rangle$ and

$$|d^1\underline{L}\rangle = \frac{1}{\sqrt{2}} \sum_\sigma d^\dagger_\sigma L_\sigma |d^0\rangle.$$

The ligand orbital $L^\dagger_\sigma$ is defined by (see Fig. 2.2 (c))

$$L_\sigma = \frac{1}{\sqrt{2}}(p_{1\sigma} + p_{2\sigma}).$$

$|0\rangle$ denotes the state which has no valence electrons but has filled core levels.

Now we map the hybridization strength of TiO_6 cluster onto 1D d-p model. It is quite natural to define our v as

$$2v \equiv \max\{\langle d^0|H_1'|d^1\underline{L}\rangle\}, \tag{2.13}$$

where $|d^1\underline{L}\rangle$ is a linear combination such as

$$|d^1\underline{L}\rangle = \sum_{\Gamma,m,\sigma} \alpha_{\Gamma m\sigma} d^\dagger_{\Gamma m\sigma} p_{\Gamma m\sigma} |d^0\rangle, \tag{2.14}$$

and the coefficients $\{\alpha_{\Gamma m\sigma}\}$ are chosen to maximize $\langle d^0|H_1'|d^1\underline{L}\rangle$ under the normalization condition $\sum_{\Gamma,m,\sigma} \alpha^2_{\Gamma m\sigma} = 1$.

It is easy to solve the extremum problem and show that the effective hybridization defined by Eq. (2.13) is given by

$$v = \frac{1}{2}\sqrt{4V(e_g)^2 + 6V(t_{2g})^2} \tag{2.15}$$

for

$$\alpha_{\Gamma m\sigma} = \frac{V(\Gamma)}{\sqrt{6V(t_{2g})^2 + 4V(e_g)^2}}. \tag{2.16}$$

Within so-called two-configuration approximation, bonding and antibonding states in the final state of RXES are defined as lower and higher energy eigenstates, respectively, of the 2×2 Hamiltonian spanned by $|d^0\rangle$ and $|d^1\underline{L}\rangle$. By definition, the bonding-antibonding separation of the present single-cation model with the effective v is exactly the same as that of the TiO_6 cluster model.

In the case of the CeO_2-like system, we can take

$$H_1' = V \sum_{m,\sigma} \left[f^\dagger_{m\sigma} p_{m\sigma} + \text{H.c.} \right] \tag{2.17}$$

with SO(3) symmetry and 7-fold degeneracy of l=3 orbital. Therefore, the effective hybridization v is given by

$$v = \frac{\sqrt{14}}{2} V. \tag{2.18}$$

Chapter 3

Interplay between Raman and Fluorescence-Like Components in Degenerate d^0 and d^1 Systems

XAS, NXES and RXES spectra are theoretically studied with a doubly-degenerate one-dimensional periodic Anderson model under d^0 and d^1 fillings. This is a simplified model of band insulators such as TiO_2, and Mott-Hubbard insulators such as Ti_2O_3. Comparing with nondegenerate model calculations, we point out the important role of orbital degeneracy in reproducing experimental excitation energy dependence of RXES. The calculated results exhibit interplay between Raman and fluorescence-like components in both band insulator and Mott-Hubbard insulator. The former and latter components reflect the local point symmetry and the translational symmetry of the system, respectively. Our results qualitatively well explain Ti $3d$-$2p$ RXES of TiO_2 and Ti_2O_3. [1]

3.1 Introduction

In this chapter, we discuss M $3d$-$2p$ RXES (M being a transition metal ion) for d^0 and d^1 insulators with multi-M cluster models including *orbital degeneracy*. We have proposed a mechanism of electronic origin in the preceding chapter for the experimentally observed fluorescence-like spectra in Ti $3d$-$2p$ RXES [46, 47] (see Fig. 1.6). The key point of our picture is the existence of extended states *against* the strong U_{dc} in the intermediate state, although such extended states may have almost negligible weight in the XAS spectrum. When Ω (incident photon energy) is tuned there, an electron excited to a $3d$ orbital can escape to the neighboring site (Fig. 3.1 (b)) because of a finite

[1] T. Idé and A. Kotani, submitted.

valence band width and finite electronic relaxation time of the core hole. Consequently, RXES spectra roughly reflect the valence band density of states. This transition process resembles NXES, which is schematically described in Fig. 3.1 (a), in the sense that a core electron is excited to a continuum state in the both cases. Thus, one can call this RXES spectrum NXES-like one, which has naturally less Ω-dependence.

For the Ω-dependence of RXES spectra, Minami and Nasu [102] stressed the role of phonon degrees of freedom. Using a model including the electron-phonon coupling but any Coulomb interaction, they insist that the origin of the fluorescence-like component, "luminescence" component in their terminology, is attributed to the full phonon relaxation of electronic momentum in the intermediate state. The Raman component is, on the other hand, attributed to the zero-phonon process, and thus described with the simple band theory. Note that the Raman component in their sense comes from delocalized Bloch states, being completely different from our theory, where local charge-transfer excitations give rise to the Raman component. Making a comparison between the phonon relaxation time τ_p and lifetime of the core hole τ_R, they concluded that the "luminescence" component due to the phonon relaxation contributes comparably to the Raman component in Ti $3d$-$2p$ RXES of TiO_2. No essential change in this conclusion has been made in their sequel theory including core and valence exciton effects within that approximation which takes only one electron-hole pair into account [103]. Experimental spectra, however, clearly show the comparable spectral weight of the two components even in the case of late transition metal oxides [104], which should be classified into Raman-dominant materials according to their theory. Hence it may well be questioned whether the phonon relaxation really governs the appearance of the fluorescence-like component in transition metal oxides, although the phonon coupling might play some role in materials either with a long τ_R and high Debye temperature such as diamond [105].

While our model successfully explained the origin of the fluorescence-like spectra, the lack of internal structure of atoms prevents us from discussing features of local origin such as polarization dependence in RXES. Very recently, Harada *et al.* observed polarization dependence of Ti $3d$-$2p$ RXES of TiO_2, where a drastic resonant enhancement occurs when Ω is tuned at a satellite peak of XAS [106], and Matsubara *et al.* pointed out that it is explained in terms of the selection rule of the local point group [107]. It is the purpose of the present chapter to extend the previous model to include orbital degeneracies, and show that calculated spectra represent coexistence of the fluorescence-like and Raman components, the latter being qualitatively consistent to the experimental polarization dependence.

Another purpose of this chapter is to study the RXES spectra in a Mott-Hubbard (MH) insulator. If an inter-site charge-transfer process crucially contributes to RXES

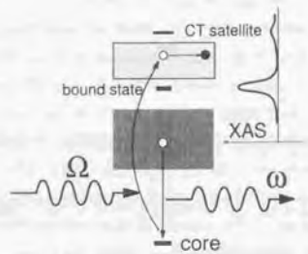

(b) fluorescence-like resonant emission

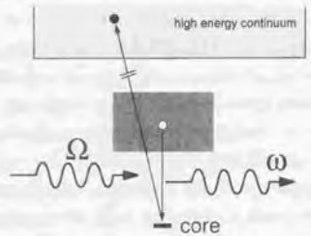

(a) normal X-ray emission

Figure 3.1: Schematic diagram of (a) the normal X-ray emission process and (b) the fluorescence-like resonant emission in $3d$-$2p$ RXES of d^0 compounds. In (a), a core electron is excited by an incident X-ray with energy Ω to a high-energy continuum far from the valence level, so that the spectrum of the emitted X-ray ω is related to the density of states of the filled valence band (darkly-shaded area). In (b), a core electron is resonantly excited to an extended valence state located between the main and CT satellite peaks of XAS. Then the electron escapes from the core hole site, with probability involving $3d$-ligand hopping integral and relaxation time $\tau_{\rm R}$ of the intermediate state. After that, the X-ray emission process resembles the case (a).

spectra in appearance of the fluorescence-like component, it is interesting to study how RXES spectra are suffered from change in character of insulating gaps upon going from a band insulator to a MH insulator. Although effective hopping energy seems to be considerably reduced by d-d on-site Coulomb interaction, experimental data on Ti $3d$-$2p$ RXES of Ti_2O_3 [108], which is often referred to as a typical MH insulator, show a clear fluorescence-like component. In the subsequent sections, we show that orbital degeneracy is essential in appearance of the fluorescence-like spectra in MH systems, and we sketch interplay between the fluorescence-like component and intra- or inter-site d-d excitations in RXES spectra.

The layout of the present chapter is as follows: In the next section, the models used are explained. As a minimal model with both translational symmetry and orbital degeneracies, a doubly-degenerate one-dimensional (1D) model is introduced. In § 3.3 and § 3.4, main features of calculated results are discussed in detail for d^0 and d^1 systems, respectively, with special attention to the role of orbital degeneracy and translational symmetry of the system. In § 3.5, the aforementioned coexistence and relation with experimental data are discussed. In § 3.6, a brief summary is given.

3.2 Formulation

We use a 1D doubly-degenerate periodic Anderson model, which is topologically equivalent to the system schematically described in Fig. 3.2 (a). The Hamiltonian is written as follows:

$$H = H_0 + V + H_{dd} + H_{dc}, \tag{3.1}$$

where the first two terms describe one-electron part, the third one $3d$-$3d$ Coulomb interaction, and the forth one $3d$-core intra-atomic Coulomb interaction.

H_0 and V are defined as

$$\begin{aligned} H_0 &= \sum_{l,\sigma}\Big[\varepsilon_0\, Q^\dagger_{l\sigma}Q_{l\sigma} + \varepsilon_0\, q^\dagger_{l\sigma}q_{l\sigma} + \varepsilon_c\, c^\dagger_{l\sigma}c_{l\sigma} \\ &+ (\Delta+\varepsilon_0)\, D^\dagger_{l\sigma}D_{l\sigma} + (\Delta - 10Dq + \varepsilon_0)\, d^\dagger_{l\sigma}d_{l\sigma}\Big], \end{aligned}$$

$$\begin{aligned} V &= \sum_{l,\sigma}\Big\{d^\dagger_{l\sigma}[v_1(q_{l\sigma}+q_{l+1\sigma}) + u_1(Q_{l\sigma}+Q_{l+1\sigma})] \\ &+ D^\dagger_{l\sigma}[v_2(Q_{l\sigma}-Q_{l+1\sigma}) + u_2(q_{l\sigma}-q_{l+1\sigma})]\Big\} + \text{H.c.} \end{aligned}$$

In the above equations, $d^\dagger_{l\sigma}$ and $D^\dagger_{l\sigma}$ represent creation operators of two $3d$ orbitals with spin σ at l-th unit cell, respectively. $q^\dagger_{l\sigma}$ and $Q^\dagger_{l\sigma}$ are creation operators of oxygen $2p$ orbitals with one-electron energy ε_0. Δ and $10Dq$ are the CT energy and the crystal

field splitting energy between the two $3d$ orbitals. $c^\dagger_{l\sigma}$ is a creation operator of a core electron with one-electron energy ε_c.

The interaction terms are defined as

$$H_{dd} = U_{d1} \sum_l \left(d^\dagger_{l\uparrow} d_{l\uparrow} d^\dagger_{l\downarrow} d_{l\downarrow} + D^\dagger_{l\uparrow} D_{l\uparrow} D^\dagger_{l\downarrow} D_{l\downarrow} \right) + U_{d2} \sum_l \left(\sum_\sigma d^\dagger_{l\sigma} d_{l\sigma} \right) \left(\sum_{\sigma'} D^\dagger_{l\sigma'} D_{l\sigma'} \right)$$

and

$$H_{dc} = -U_{dc} \sum_{l,\sigma,\sigma'} \left(d^\dagger_{l\sigma} d_{l\sigma} + D^\dagger_{l\sigma} D_{l\sigma} \right) c_{l\sigma'} c^\dagger_{l\sigma'}, \tag{3.2}$$

where U_{d1} (U_{d2}) is the on-site d-d or D-D (d-D) Coulomb correlation energy, and U_{dc} is the intra-atomic core-$3d$ interaction. Exchange and spin-orbit couplings are omitted for simplicity.

The d-p hopping energies are represented with $\{v_1, v_2, u_1, u_2\}$. Depending on their relative phases and values, there are some ways to include orbital degeneracy into this model. The single-metal-ion cluster limit of our model is described in Fig. 3.2 (b). We consider that the single-M cluster is an effective model of an MO_6 cluster. In the case of a MO_6 cluster with O_h symmetry, a subsystem having $d(e_g)$ orbitals and ligand orbitals with e_g symmetry is coupled with a subsystem having $d(t_{2g})$ orbitals and ligand orbitals with t_{2g} symmetry through d-d Coulomb interaction (cf. Fig. 1.9). If there were no Coulomb interaction, the subsystems would be completely decoupled. Considering this fact, we set $v_1 = u_1$ and $v_2 = u_2$, then the ligand orbitals are separated into two orthogonal molecular orbitals as

$$p_\sigma \equiv \frac{1}{2}(q_{0\sigma} + q_{1\sigma} + Q_{0\sigma} + Q_{1\sigma}) \tag{3.3}$$

and

$$P_\sigma \equiv \frac{1}{2}(q_{0\sigma} - q_{1\sigma} + Q_{0\sigma} - Q_{1\sigma}). \tag{3.4}$$

Consequently, the single-M cluster is reduced to that in Fig. 3.2 (c). Now we can regard the d-p unit as an effective subsystem of the $d(t_{2g})$-$L(t_{2g})$ one, and the D-P unit as an effective subsystem of the $d(e_g)$-$L(e_g)$ one, where L stands for ligand molecular orbital [2].

To evaluate hopping energies, we apply the effective hybridization theory separately to e_g and t_{2g} orbitals. For t_{2g} (d) orbitals, the starting point is the equation

$$\max\{\langle d^0|H|d^1\underline{p}\rangle\} = \max\{\langle d^0|H|d(t_{2g})^1\underline{L}(t_{2g})\rangle\},$$

[2]The other choice that $v_1 = u_1$ and $v_2 = -u_2$ also leads to the exactly same single-M cluster as in Fig. 3.2 (c). Since these two choices prove to be exactly equivalent even in the double-M cluster (periodic d_2p_2) case, it is conceivable that the conclusions in the present chapter do not drastically depend on the choice at all.

where $|d^1\underline{p}\rangle = \frac{1}{\sqrt{2}}\sum_\sigma d^\dagger_\sigma p_\sigma |d^0\rangle$. As suggested by Eq. (3.3), the left hand side is given by $\sqrt{2} \times 2v_1$, where $\sqrt{2}$ represents the contribution of spin degeneracy. The right hand side is given by $\sqrt{6}V(t_{2g})$, where $V(t_{2g})$ is the hybridization strength of a TiO_6 cluster model. Hence we have v_1=$\sqrt{3}V(t_{2g})/2$. Similarly, v_2 is estimated as v_2=$V(e_g)/\sqrt{2}$. For $V(e_g)$=3.0 and $V(t_{2g})$=-1.5 eV [49], we have v_1=u_1=1.3 and v_2=u_2=2.1 eV. Other parameters are chosen to be the same as Ref. [49]: Δ=4.0, $10Dq$=1.7, U_{d1}=U_{d2}=4.0 and U_{dc}=6.0 [eV].

Uozumi [109] and Taguchi [110] report nearly the same value of U_{dd}, U_{dc}, $10Dq$, and $V(e_g)$ as those of TiO_2 in their analyses on Ti $2p$-XPS of Ti_2O_3, so that we take the same parameter also for d^1 systems in this chapter [3].

In addition to the doubly-degenerate models, we use also nondegenerate models shown in Fig. 2.2 to discuss the role of orbital degeneracy. The value of the parameter set including d-p hopping energy v, CT energy Δ, on-site d-d Coulomb energy U_{dd}, and on-site core-d attractive interaction U_{dc} will be explained in the subsequent subsections.

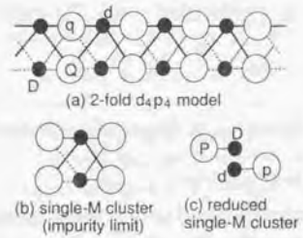

Figure 3.2: The *degenerate* d-p models used. (a) A topologically equivalent system of the doubly degenerate periodic d_4p_4 model. (b) The single-M cluster model with *open* boundary condition. (c) The reduced single-M cluster model, where d-D Coulomb interaction couples the two subsystems. For the definition of the orbitals P and p, see the text. In these figures, the black and white circles represent Ti $3d$ and oxygen $2p$ orbitals, respectively. The d-p transfer with positive sign is described with the solid lines, whereas transfer with negative sign is described with dashed lines. Note that local symmetries around the nonequivalent $3d$ orbitals (d and D) are not the same.

In the present model, X-ray absorption and emission processes at a metal site l are

[3]Reference [110] reports a large CT energy 6.5 eV. Note that this corresponds to $U_{dd} + \Delta - \frac{3}{5}10Dq$ in the notation of the present model, giving Δ=3.52 for U_{dd}=4.0 and $10Dq$=1.7.

described with the following operators:

$$T^{\rm a}(l) = \sum_{\sigma} (a_1 d^\dagger_{l\sigma} + a_2 D^\dagger_{l\sigma}) c_{l\sigma} \tag{3.5}$$

$$T^{\rm e}(l) = \sum_{\sigma} c^\dagger_{l\sigma} (b_1 d_{l\sigma} + b_2 D_{l\sigma}), \tag{3.6}$$

where $\{a_1, a_2\}$ and $\{b_1, b_2\}$ are numerical factors, representing polarization dependence of the RXES. All of them are taken to be unity unless any particular mention is made. The transition operator of RXES is defined in Eq. (2.8),

$$\sum_l T^{\rm e}(l) G_0(\Omega) T^{\rm a}(l).$$

It is worth noting that the point group symmetry of operators $d_{l\sigma} G_0 d^\dagger_{l\sigma}$ and $D_{l\sigma} G_0 D^\dagger_{l\sigma}$ is different from that of $d_{l\sigma} G_0 D^\dagger_{l\sigma}$ and $D_{l\sigma} G_0 d^\dagger_{l\sigma}$. The latter leads to final states with a different local point group symmetry from the ground state. As will be discussed, it brings about a class of nonbonding final states. The spectral function of the RXES process has been defined by Eq. (2.10). In this chapter, we use the same value Γ=0.4 eV as that in the preceding chapter.

3.3 Calculated Results I: Band Insulators

3.3.1 Nondegenerate d^0 system

To elucidate role of orbital degeneracy, we first recapitulate results of nondegenerate models as shown in Fig. 2.2, where the parameter set Δ=4.0, U_{dd}=4.0, U_{dc}=6.0, and v=$\sqrt{(2v_1)^2 + (2v_2)^2}/2$=3.5 eV are used. These are the same as those in the preceding chapter. For all XAS, RXES and NXES spectra in the present chapter, the momentum-transfer q is fixed to be zero, and calculated line spectra are convoluted with Lorentzian 1.0 eV (HWHM). Moreover, the z-component of the total spin S_z is taken to be zero except for single-M cluster calculations with d^1 filling.

Figure 3.3 (a) and (b) show the calculated spectra with nondegenerate single- and multi-M cluster models. Detailed discussions on the spectra have been given in the preceding chapter with special attention to the appearance of the fluorescence-like spectra in the multi-M cluster model. Let us briefly review the bonding-antibonding separation in the XAS and RXES spectra within the single-M cluster model. When photoexcited, there are only two states $\{|\underline{c}d^1\rangle, |\underline{c}d^2\underline{L}\rangle\}$ in the Hilbert space of the single-M cluster. Diagonalizing the 2×2 Hamiltonian matrix, we have the energy separation W_0' between the bonding and antibonding states as

$$W_0' = \sqrt{(\Delta + U_{dd} - U_{dc})^2 + 8v^2} \simeq 10.1 \text{ eV}.$$

Similarly, in the final state of RXES, the bonding-antibonding separation is roughly estimated within so-called two-configuration approximation,

$$W_0 = \sqrt{\Delta^2 + 16v^2} \simeq 14.6 \text{ eV}.$$

Note that matrix element $\langle d^1\underline{L}|H|d^0\rangle$ is $\sqrt{2}\times\sqrt{2}v$, where the first $\sqrt{2}$ originates from the spin degeneracy. These formulae will give a rough estimation on the bonding-antibonding separation in more elaborate models.

3.3.2 Degenerate d^0 system

Figure 3.4 (a) shows XAS, NXES and RXES spectra calculated with the degenerate single-M cluster model. In the XAS spectrum, we observe two strong peaks and a number of subpeaks in their high energy tail. Experimentally, four distinct peaks are observed in the main structure of Ti $2p$-$3d$ XAS of d^0 compounds such as TiO_2 and $FeTiO_3$ [46, 47]. Since our model does not include the spin-orbit interaction of the core level, the two experimental peaks with lower energies correspond to the calculated main structure.

We also see that the RXES spectra depend on incident photon energy Ω rather than the simple Raman component in the case of the nondegenerate single-M cluster. For lower Ω's such as 1 and 2, the single spectrum which linearly shifts as Ω increases is observed. This inelastic spectrum highlighted with blank bars survives for higher Ω's, whereas another spectrum highlighted with the shaded bar suddenly appears for 5 and 6. This kind of enhancement when Ω is targeted at a satellite peak of XAS is also observed in the nondegenerate case, as marked also with shaded bars in Fig. 3.3 (a). However, the nondegenerate results have no peaks corresponding to the series of peaks marked with blank bars in Fig. 3.4 (a). Hence, we conclude that this series of peaks originates from the orbital degeneracy. By the reason discussed below, we call these peaks nonbonding ones hereafter.

To understand the origin of the inelastic spectra, consider the case of isotropic limit that $10Dq \to 0$ and $v_1 \to v_2$, where the Hamiltonian recovers permutation symmetry between $\{d, p\}$ and $\{D, P\}$. Within the two-configuration approximation, the bonding and antibonding states in the final state of RXES are described with state vectors $|0_0\rangle \equiv |d^0\rangle$ and

$$|1_0\rangle = \frac{1}{2}\sum_\sigma (d^\dagger_\sigma p_\sigma + D^\dagger_\sigma P_\sigma)|d^0\rangle.$$

Note that these two states have the same permutation symmetry as well as local point group symmetry. With a matrix element $V_{\rm eff}(d^0) \equiv \langle 1_0|H|0_0\rangle = \sqrt{2[(2v_1)^2 + (2v_2)^2]}$, the bonding and antibonding separation is proven to be W_0, although calculated spectra

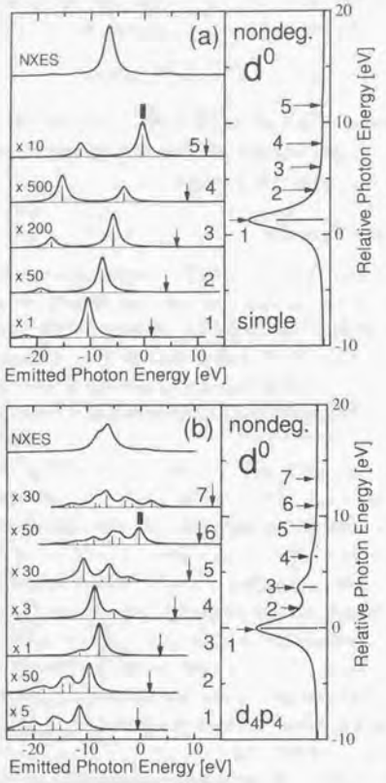

Figure 3.3: XAS, RXES and NXES spectra calculated with *nondegenerate* models under d^0 filling, (a) the single-M and (b) d_4p_4 periodic clusters. For each figure, the right and left panels show XAS and RXES spectra, respectively. There is also a NXES spectrum at the top of the array of the RXES curves in the left panel. The arrows in each XAS spectrum indicate the position of excitation energies, and the numbers in the XAS spectra correspond to those of RXES. The elastic scattering peaks are omitted from the figures, and they are replaced with the arrows. Each of original calculated RXES spectra is maguified by a rate indicated as "× 3".

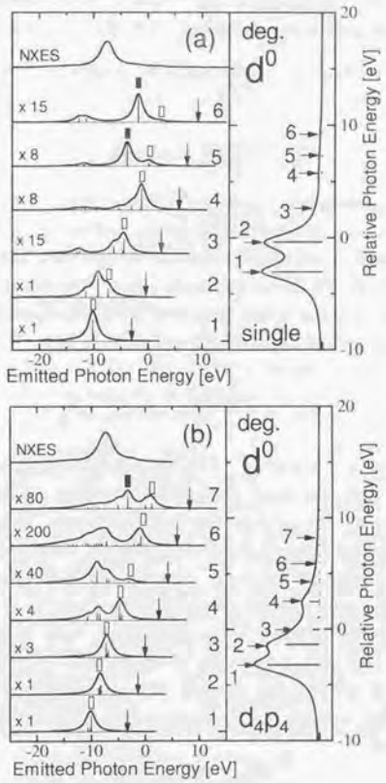

Figure 3.4: XAS, RXES and NXES spectra calculated with *degenerate* models under d^0 filling, (a) the single-M and (b) d_4p_4 periodic clusters. See the caption for Fig. 3.3.

exhibit somewhat smaller value than W_0 [4]. Similarly to the nondegenerate case, $|g\rangle$ is the bonding state with relatively large $|0_0\rangle$ weight, and the antibonding state has relatively large $|1_0\rangle$ weight. Since the transition operators are symmetric as to the permutation, all allowed intermediate states have the same symmetry as $|g\rangle$ in this case. In the two-configuration approximation, each of them is a linear combination of

$$|1_0'\rangle = \frac{1}{2}\sum_\sigma (d_\sigma^\dagger + D_\sigma^\dagger)c_\sigma|0_0\rangle$$

and

$$|2_0'\rangle \propto \sum_\sigma (d_\sigma^\dagger + D_\sigma^\dagger)c_\sigma|1_0\rangle,$$

giving bonding and antibonding intermediate states. Since $\Delta + U_{dd} - U_{dc} > 0$, the bonding intermediate state has mainly $|1_0'\rangle$ weight, and would have large overlap with $(d_\sigma^\dagger + D_\sigma^\dagger)c_\sigma|g\rangle$. Similarly, the antibonding intermediate state has large overlap with $(d_\sigma^\dagger + D_\sigma^\dagger)c_\sigma|\mathrm{AB}\rangle$, where $|\mathrm{AB}\rangle$ is the antibonding final state. Consequently, absorption intensity strongly concentrates at the main peak, and $|\mathrm{AB}\rangle$ is strongly enhanced when Ω is tuned at the satellite peak in the XAS spectra.

Note that a final state such as

$$|\mathrm{N1}_0\rangle \equiv \frac{1}{2}\sum_\sigma (d_\sigma^\dagger P_\sigma + D_\sigma^\dagger p_\sigma)|d^0\rangle$$

can contribute to inelastic scattering. This has the same permutation symmetry as that of the ground state, but local point group symmetry around the metal site is different. This fact encourages us to call it a nonbonding state. By the reason explained above, it is the elastic line (ground state) that the most strongly enhanced when Ω is tuned at the main absorption manifold. The elastic line is, however, omitted from the figures, so that the main inelastic spectra originate from the nonbonding states for that Ω. By definition, the existence of the nonbonding states is direct consequence of orbital degeneracy. The nonbonding state is energetically Δ higher than $|d^0\rangle$, being nearly independent of hybridization strength. Since the energy of the bonding state is estimated as $(\Delta - W_0)/2$ within the two-configuration approximation, the nonbonding state will be observed

$$W_{0\mathrm{N}} \equiv (\Delta + W_0)/2$$

distant from the elastic line. Note that this is always smaller than W_0, and therefore the nonbonding state is located in between the bonding and antibonding states in any case.

When a finite $10Dq$ is introduced, we have a finite energy difference between $\underline{c}d^1$- and $\underline{c}D^1$-dominant intermediate states due to $10Dq$, so that we observe the doubly-peaked

[4] From a quantitative point of view, the two-configuration approximation is poor one in the context of the large-N expansion theory [20, 111] because the number of degenerate orbitals is only two.

structure in the main manifold of the XAS spectrum. Similarly, the nonbonding lines split into several ones in a RXES spectrum. Since the Hamiltonian is not symmetric as to the permutation, an antisymmetric state

$$|\mathrm{N2}_0\rangle \equiv \frac{1}{2}\sum_\sigma (d_\sigma^\dagger p_\sigma - D_\sigma^\dagger P_\sigma)|d^0\rangle$$

appears as a nonbonding peak in the final state. This state has the same local point group symmetry as the ground state. Furthermore, $|\mathrm{N1}_0\rangle$ split into the following two states:

$$|\mathrm{N1}_0 1\rangle \equiv \frac{1}{\sqrt{2}}\sum_\sigma d_\sigma^\dagger P_\sigma|d^0\rangle$$

$$|\mathrm{N1}_0 2\rangle \equiv \frac{1}{\sqrt{2}}\sum_\sigma D_\sigma^\dagger p_\sigma|d^0\rangle,$$

with energy separation of order of $10Dq$. Thus, we observe three nonbonding lines in this case. Generally, anisotropy of v_1 and v_2 gives rise to energy shift of the nonbonding peaks. As a result, $\mathrm{N1}_0 1$- and $\mathrm{N2}_0$-dominat states are accidentally seen at nearly the same position in Fig. 3.4 (a). The transition processes in the single-M cluster is summarized in Fig. 3.5, where these three nonbonding states are represented with the shaded rectangle. Note that the nonbonding states are hardly perturbed with the metal-ligand hybridization.

These features of the degenerate single-M cluster calculation are substantially conserved in the multi-M cluster calculation. Apart from subpeaks such as 4, the main manifold of the XAS spectrum shown in Fig. 3.4 (b) is composed of two definite lines, and we can naturally attribute these lines to those states which have relatively large $\underline{c}d^1$ or $\underline{c}D^1$ weight in the photoexcited cluster. For RXES spectra, we see, firstly, that the nonbonding states give the main inelastic structure for the main peak resonance (spectrum 1 and 2). Secondly, the antibonding state marked with the shaded bar is strongly enhanced when Ω is tuned in the vicinity of the satellite peak (spectrum 7), although the satellite peak is greatly smeared out and does not give a clear structure.

Close inspection shows, however, certain modifications are observed in the spectra of local origin. Firstly, while the nonbonding states keep energy separation of order of $10Dq$ in the single-M cluster calculation, the separation in Fig. 3.4 (b) is considerably contracted because of the finite transfer between unit clusters. Whether or not this is the case in realistic three-dimensional systems is unclear because whether the separation between the nonbonding states get smaller or larger would greatly depend on a band structure. Secondly, the intensity ratio of the main XAS peaks is slightly changed. This is possibly associated with a change in character of the main absorption peaks, i.e. from the simple bonding state to a core-excitonic state.

The most conspicuous change in RXES spectra is occurrence of the fluorescence-like spectra. Figure 3.4 (b) exhibits the inelastic spectra whose position is almost the

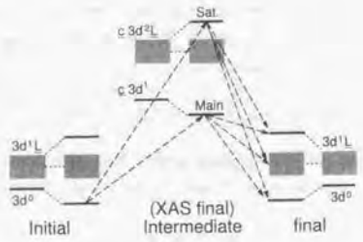

Figure 3.5: The energy scheme of $3d$-$2p$ RXES of d^0 compounds in the standard notation. In the initial and final states, the metal-ligand hybridization creates the bonding (represented with the lowest horizontal bar), antibonding (the highest bar) and nonbonding states (the shaded rectangle). These three kinds of states similarly exist in the intermediate state. While the d-p hybridization gives rise to the bonding-antibonding separation, the energy of nonbonding states is hardly perturbed with the hybridization.

same as that of NXES for almost all Ω's higher than 3. This is sharp contrast to the nonbonding-antibonding spectra explained above, which behave as if NXES spectrum has no relation with RXES. Similarly to the nondegenerate case, we confirm again that the origin of such spectra is itinerancy in the targeted intermediate state. The subpeaks in the high-energy tail of the main absorption peaks, such as 3, 4 and 5 in Fig. 3.4 (b), originate from a finite number of k-points, and highly itinerant according to the core exciton theory. In fact, a detailed analysis of the present author shows that a photoexcited electron in the intermediate state 3 is delocalized mainly through the d-p transfer path, and that a photoexcited electron in the intermediate states 4 and 5 is delocalized mainly through the D-P transfer path.

3.4 Calculated Results II: Mott-Hubbard Insulators

3.4.1 Nondegenerate d^1 system

Figure 3.6 shows calculated XAS, NXES and RXES spectra with nondegenerate models with d^1 filling, which simulates the t_{2g} bands of Ti_2O_3. The parameters are taken as v=2.0, Δ=2.0, U_{dd}=4.0 and U_{dc}=6.0 eV [109]. Because of $U_{dd}+\Delta > U_{dd}$, this system is in the MH regime in the Zaanen-Sawatzky-Allen diagram [22]. Note that the lowest charge excitation is made by inter-site d-d excitations in this case. Then it is interesting to study RXES spectra of MH systems in the context of the nonlocal (or large-cluster)

effects.

In the nondegenerate single-M cluster model with d^1 filling, the only possible configuration in the intermediate state is $\underline{c}d^2$, so that we have the only single peak in XAS spectra in Fig. 3.6 (a). On the other hand, two configurations of d^1 and $d^2\underline{L}$ are possible in the final state. Thus, we observe the only inelastic peak due to charge-transfer

$$W_1' = \sqrt{(\Delta + U_{dd})^2 + 8v^2} \simeq 8.2 \text{ eV}$$

distant from the elastic line, and the RXES spectra exhibit necessarily only Raman component.

In the NXES spectrum in Fig. 3.6 we see a strong peak at about -2 eV and a weak structure at about -10 eV. The former corresponds to a d^0-dominant state, and the latter to a $d^1\underline{L}$-dominant state.

In addition to the CT peak, the inter-site d-d excitation should take part in RXES spectra in the multi-M cluster model. There observed an inelastic peak approximately 4.4 eV distant from the elastic line in RXES spectra in Fig. 3.6 (b). While spectral weight of this peak is strong for lower Ω's up to 5, a structure about 10 eV distant from the elastic line is enhanced for Ω's higher than 5. To study these structures, we calculate valence photoemission spectra (PES) and Bremsstrahlung Isochromat spectra (BIS), whose spectral functions are written as

$$F_{\rm PES}(k,\omega) = \sum_f |\langle f|d_{k,\gamma}|g\rangle|^2 \delta(\omega + E_f - E_g) \tag{3.7}$$

$$F_{\rm BIS}(k,\omega) = \sum_f |\langle f|d^\dagger_{k,\gamma}|g\rangle|^2 \delta(\omega - E_f + E_g). \tag{3.8}$$

Figure 3.7 shows PES and BIS spectra, where we adopt a nondegenerate d_8p_8 cluster model with the same parameter to take more k-points. The figure clearly shows that the upper branch of the simple Bloch bands in the $U_{dd} \to 0$ limit (solid curves)

$$\varepsilon^{\pm}(k) - \varepsilon_0 = \frac{\Delta}{2}\left(1 \pm \sqrt{1 + (4v/\Delta)^2 \cos^2(k/2)}\right)$$

is substantially modified into the lower Hubbard band (LHB) and upper Hubbard band (UHB). Hence we attribute the aforementioned lower energy structure in RXES to a CT process, and the higher energy one to an inter-site d-d transfer, which rules the Mott-Hubbard gap. We call the former one "CT" and the latter "MH" hereafter. Furthermore, the intense peak at -4 eV in the NXES spectrum (Fig. 3.6 (b)) is attributed to a radiative transition from LHB, whereas a bump in its low energy tail to a radiative transition from the lowest valence band. The difference in intensity is naturally explained by difference in d-weight of these bands.

Although the MH structure in Fig. 3.6 (b) is composed of the single line, there should be generally energy dispersion in this structure. To confirm this, we show XAS

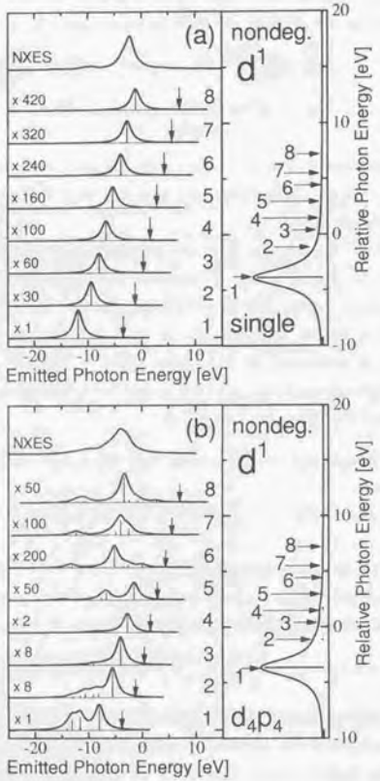

Figure 3.6: XAS, RXES and NXES spectra calculated with *nondegenerate* models under d^1 filling, (a) the single-M and (b) d_4p_4 periodic clusters. See the caption for Fig. 3.3.

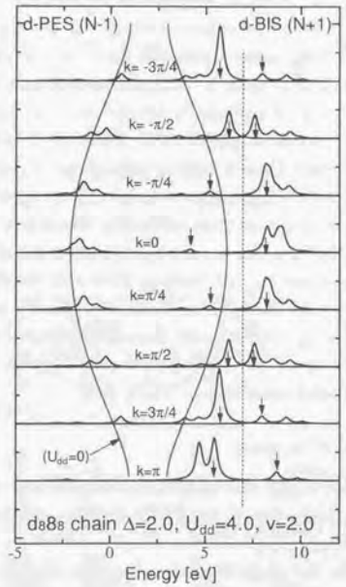

Figure 3.7: PES and BIS spectra calculated with the d_8p_8 *nondegenerate* chain. The calculated spikes are convoluted with Lorentzian 0.2 eV (HWHM). The solid curves show the Bloch bands in the $U_{dd} \to 0$ limit. The arrows show the upper and lower Hubbard bands. The Fermi level is represented with the dotted line. We take ε_0 as the origin of the energy.

and RXES spectra calculated with the d_8p_8 cluster in Fig. 3.8, where all RXES spectra are plotted as a function of Raman shift. The MH structure is clearly seen at about -3.5 eV, and the CT structure at about -9.5 eV. We observe energy dispersion of the MH structure for spectra 4 and 5. Corresponding to the fact that only $|\underline{c}d^2\rangle$ is possible in the single-M cluster limit, the XAS spectrum has the strong peak labeled with M, as in Fig. 3.6 (b). The additional peaks are also observed in its high energy tail. Their characters are depicted schematically in Fig. 3.9 (a), where each transition process between many-body states is mapped into a counterpart in the one-electron picture. In the states corresponding to the main peak M and the very weak satellite peak S, the core hole is mainly screened by the photoexcited electron itself. The peaks 4 and 5 correspond to the excitation to UHB. These are necessarily delocalized and poorly-screened. The peaks 2 and 3 have an intermediate character of the two states, and they are irrelevant to be depicted as a one-electron process.

Similarly, RXES final states are visualized in Fig. 3.9 (b) in terms of the one-electron density of states. The MH structure is related to one electron-hole pair creation between UHB and LHB, whereas the CT one between UHB and the filled ligand band. The dispersive Ω-dependence for the spectra 4 and 5 is directly associated with energy dispersion of UHB. Although this behavior is somewhat similar to the fluorescence-like spectra, its energy width is too narrow under the realistic parameter set for Ti oxides [5] to explain the experimental trend of, e.g., Ti_2O_3 [108].

3.4.2 Degenerate d^1 system

Figure 3.10 shows XAS, NXES and RXES spectra calculated with degenerate single-M cluster and d_4p_4 models with d^1 filling. We fixed S_z=1/2 for the single-M cluster calculation.

Let us first consider the single-M cluster case. We see that the main manifold of XAS spectra exhibits a doubly-peaked structure. This is consistent to the d^0 calculation, but the lower energy absorption peak is considerably suppressed because of larger occupation number in the lower energy d-orbital. We also see that the higher branch of the main manifold in Fig. 3.10 (a) is composed of a few peaks with extremely small energy separation. This is attributed to the contribution of spin multiplet. When Ω is tuned at these peaks, the resultant final state would have large D^1 weight. Thus a strong inelastic peak observed 2.5 eV distant from the elastic peak in RXES spectrum 2 is attributed to the intra-site d-d excitation, which has been shown in Fig. 1.8 (left). We denote this excitation by "d-d" hereafter. Note that the value 2.5 eV is the same order of $10Dq$, but from a quantitative point of view, it considerably deviates from

[5] This is still true also for the larger value of v=3.5 eV, which roughly simulates both e_g and t_{2g} orbitals.

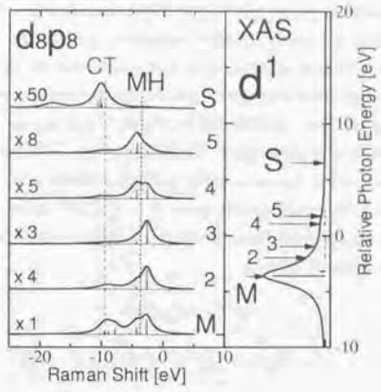

Figure 3.8: RXES and XAS spectra calculated with the d_8p_8 *nondegenerate* chain. Note that the abscissa is defined as Raman shift $\omega - \Omega$, which is the same as $E_g - E_f$. The elastic line, which should reside at zero, is omitted from the figure. The excitation energies and the numbers attached to the arrows in the XAS spectrum correspond to those in the RXES spectra.

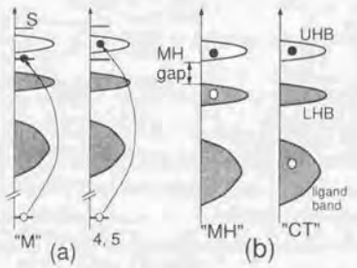

Figure 3.9: Schematic explanation of representative final states in XAS and RXES spectra. The shaded and blank areas show occupied and unoccupied densities of states, respectively. The closed and open circles represent an electron and hole, respectively. (a) In the intermediate (XAS final) state, a core electron is photoexcited to bound states (represented with bars) or UHB. The labels M, S, 4 and 5 correspond to those in Fig. 3.8. (b) An electron-hole pair is left in the final state.

$10Dq$ because of relatively large anisotropy of hybridization v_1 and v_2.

In addition to the d-d peak, another structure is observed about 10 eV distant from the elastic line. This is attributed to charge-transfer to the metal site from the neighboring ligand sites. To study the origin of inelastic peaks more clearly, we arrange the same RXES spectra with Raman shift in Fig. 3.11 (a), where one sees that the CT structure is distributed over about 4 eV. Unlike the d^0 case, the permutation symmetry does not rule the separation between antibonding and nonbonding states when a finite $10Dq$ works, because the unperturbed state $|1_l\rangle \equiv d^\dagger_\uparrow|d^0\rangle$ is not symmetric. Within the two-configuration approximation, there are two other state vectors, which have the same point group symmetry as $|1_l\rangle$,

$$|2_l1\rangle \equiv d^\dagger_\downarrow p_\downarrow|1_l\rangle$$

$$|2_l2\rangle \equiv \frac{1}{\sqrt{2}}\sum_\sigma D^\dagger_\sigma P_\sigma|1_l\rangle.$$

Both of them have a doubly-occupied metal site. Consider a linear combination of these vectors, $|2_l\rangle$, under condition such that $|\langle 2_l|H|1_l\rangle|$ is maximized. Following the effective hybridization theory, we have

$$|2_l\rangle = \frac{2}{V_{\rm eff}(d^1)}\left(v_1|2_l1\rangle + \sqrt{2}v_2|2_l2\rangle\right),$$

where

$$V_{\rm eff}(d^1) \equiv \sqrt{(2v_1)^2 + 2(2v_2)^2}.$$

Diagonalizing 2×2 Hamiltonian spanned by $\{|1_l\rangle, |2_l\rangle\}$, we have bonding-antibonding separation

$$W_1 \simeq \sqrt{(\Delta + U_{dd})^2 + 4V^2_{\rm eff}},$$

which is the same order of W_0. A peak at -12.6 eV labeled with "AB" in Fig. 3.11 (a) originates from this antibonding state, and it is strongly enhanced when Ω is tuned at the satellite structures 5 and 6, being consistent to the d^0 case. This is also described in Fig. 3.10 (a) with the shaded bars.

In this context, we consider the state orthogonal to $|2_l\rangle$ as the nonbonding state in the truncated Hilbert space,

$$|{\rm N}2_l\rangle = \frac{2}{V_{\rm eff}(d^1)}\left(-\sqrt{2}v_2|2_l1\rangle + v_1|2_l2\rangle\right).$$

This corresponds to a peak at -8.8 eV, which is strongly enhanced in the RXES spectrum 4. This fact suggests that the absorption spectra in the vicinity of the arrow labeled with 4 has also nonbonding character. In fact, it has relatively large weight in $|\underline{c}D^1; d^2\underline{p}\rangle$, which gives rise to relatively large $|2_l1\rangle$ weight after radiative transition of the D electron.

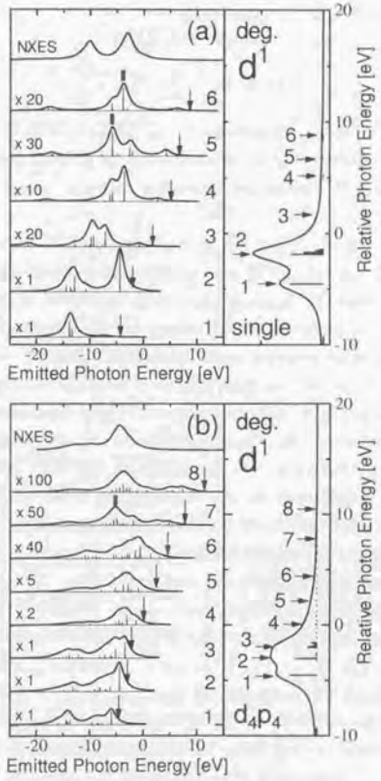

Figure 3.10: XAS, RXES and NXES spectra calculated with the *degenerate* models under d^1 filling, (a) the single-M and (b) d_4p_4 periodic clusters. See the caption for Fig. 3.3.

There is another class of nonbonding states, which has different point group symmetry from $|g\rangle$. When Ω is tuned at the main absorption peaks, it is this class of states that are the most strongly enhanced, as in the d^0 case. Corresponding to $|\mathrm{N1}_0 1\rangle$ and $|\mathrm{N1}_0 2\rangle$, state vectors such as

$$|\mathrm{N1}_1 1\rangle \equiv d_\downarrow^\dagger P_\downarrow |1_1\rangle$$

$$|\mathrm{N1}_1 2\rangle \equiv \frac{1}{\sqrt{2}} \sum_\sigma D_\sigma^\dagger p_\sigma |1_1\rangle$$

are of this kind. The former contributes to an inelastic peak at -9.3 eV when Ω is tuned at the peak 1, whereas the latter contributes an inelastic peak at -11.3 eV when Ω is tuned at the peak 2. The energy separation between them is naturally attributed to $10Dq$.

Apart from the d-d structure, the Ω dependence of RXES spectra has much in common with the d^0 spectra in Fig. 3.4 (a) rather than the nondegenerate calculation in Fig. 3.6 (a). The multi-M cluster (d_4p_4) results are shown in Figs. 3.10 (b) and 3.11 (b). In contrast to the single-M cluster results, we observe fluorescence-like behavior there. Note that the nondegenerate multi-M cluster calculation in Fig. 3.6 (b) exhibits no such behavior. Thus we conclude that it is essential for the appearance of the fluorescence-like spectra in d^1 systems to include orbital degeneracy.

The other large-cluster effect is inelastic peaks due to inter-site d-d excitations. Compare Fig. 3.11 (b) with Fig. 3.8. As explained, the latter model is regarded as a truncated model to include only the d-p transfer path of the former. We notice that a bump at about -4 eV in Fig. 3.11 (b) for RXES spectra 1, 2, 3 and 4. This is attributed to the inter-site d-d excitation, and labeled with "MH", as in Fig. 3.8. Although the MH structure is separated from the CT structure in Fig. 3.8, one observes that the center of the spectral weight moves to lower energy roughly proportional to Ω, from MH to CT structure and beyond, resulting in the fluorescence-like spectra in Fig. 3.11 (b).

On the other hand, we see that a structure at about -10 eV is enhanced for 1 and 2, and a structure at about -11.9 eV is enhanced for 3. This is explained by the enhancement of the nonbonding states which originate from $|\mathrm{N1}_1 1\rangle$, $|\mathrm{N1}_1 2\rangle$ and $|\mathrm{N2}_1\rangle$. We also observe an isolated peak at -1.4 due to the intra-site d-d excitation. The resonance enhancement of the antibonding peak is also observed for the spectrum 7, as expressed with the shaded bar in Fig. 3.10 (b). Figure 3.11 (b) is very intriguing in that these structures of local origin, which are successfully explained with single-M cluster model, coexist with the aforementioned structures due to inter-site effects.

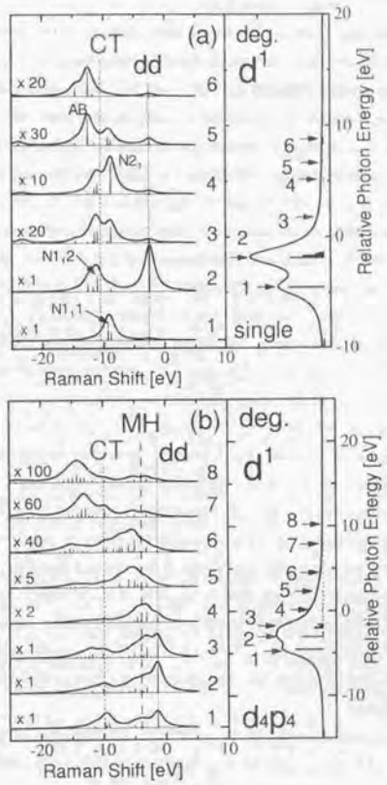

Figure 3.11: RXES and XAS spectra for d^1 filling calculated with (a) the degenerate single-M and (b) degenerate d_4p_4 cluster models. All a_i and b_i are set to be unity, and all excitation energies and the numbers attached to the arrows are the same as in Fig. 3.10. See the caption for Fig. 3.3.

3.5 Discussion

3.5.1 d^0 system

We defined a nonbonding state as that state which has no or little hybridization matrix element with the ground state. Mathematically, this definition may hold in realistic three-dimensional systems. Figures 3.4 (a) and (b) show slight Ω-dependence in the nonbonding structure, where the spectral weight moves from higher energy to lower energy branch of the nonbonding peaks in going from the spectrum 1 to 3. As discussed within the single-M cluster model, the energy separation between the two nonbonding states, which originate from $|\mathrm{N}1_0 1\rangle$ and $|\mathrm{N}1_0 2\rangle$, is attributed mainly to $10Dq$. While this kind of Ω-dependence is consistent to experimental feature [106], the calculated spectra show considerable cluster size dependence of the separation. This is an example that a feature of local origin is renormalized by multi-M cluster effects. Apart from this kind of slight dependence, the fact that Ω-dependence of the nonbonding structure is not very strong in experimental Ti 3d-2p RXES of TiO_2 [106] suggests that the nonbonding structure is composed of states with various symmetries, and these states are highly smeared out by O 2p band effects.

The latest experimental data on Ti 3d-2p RXES of TiO_2 [106] shows a strong resonance enhancement of a peak 14 eV distant from the elastic line when Ω is tuned at the satellite structure of the XAS spectrum under a polarized configuration. This enhancement is not observed in Fig. 1.6, where the depolarized configuration is adopted. This fact means that the CT excited state corresponding to the 14 eV peak is the same symmetry as $|g\rangle$, and we naturally attribute it to the antibonding state, whose origin is the higher energy eigenstate in the truncated Hilbert space spanned by $|0_0\rangle$ and $|1_0\rangle$. Despite of its simplicity, our model well explains the essential physics of the experimental 14 eV enhancement. Note that spinless exciton models [103] can not describe the CT satellite of XAS, and therefore by no means describe the experimental polarization dependence.

There had been a controversy on the origin of the satellite structure of Ti 2p-XPS or 2p-XAS of TiO_2 [49, 112]. Okada and Kotani conclusively demonstrated that it is the CT satellite by their theoretical analysis with a TiO_6 cluster model [49]. With this regard, the polarization dependence of RXES when Ω is tuned at the satellite structure is significant in that it dramatically proves its character as the CT satellite. Moreover, the large bonding-antibonding separation offers evidence that TiO_2 is in the strong hybridization regime. Thus, parameter estimations based on the atomic picture would be subtle in many cases.

Apart from the fluorescence-like behavior, the single-M cluster model well explained the Ω-dependence of RXES spectra calculated with the multi-M cluster model. This

means that the local transition picture as shown in Fig. 3.5 is at least partly applicable to the Raman component despite the translational symmetry of the system. This is a consequence of the special feature of RXES that reflects local as well as itinerant nature of the system.

We comment on the relative intensity of the structures of local origin, i.e. the antibonding and nonbonding structures. Comparing Fig. 3.3 with Fig. 3.4, we see that they are clearer in the latter than in the former. This suggests a trend that the more available internal degrees of freedom a unit cluster has, the more weight of spectra of local origin is observed. The reason is naturally related to the number of transition paths.

3.5.2 d^1 system

We demonstrated the appearance of the intra-site d-d excitation in RXES spectra for d^1 systems. Recently Higuchi *et al.* reported that intensity of a peak 2.3 eV distant from the elastic line increases with La doping for $SrTiO_3$ [113]. Since $La_xSr_{1-x}TiO_3$ has nominally d^x filling, their explanation that the 2.3 eV peak is caused by the intra-site $t_{2g} \rightarrow e_g$ transition (see Fig.1.8) seems to be natural. While they made estimation of the value of $10Dq$ simply as 2.3 eV, Fig. 3.11 shows considerable cluster size dependence of its energy separation from the elastic line. We have the value of 2.5 eV with the single-M cluster model, whereas 1.4 eV with the multi-M cluster model. Although the latter is fairly close to the actual value $10Dq$=1.7 eV, whether or not this is the case in realistic three-dimensional systems is unclear because whether it gets smaller or larger would greatly depend on a band structure. What we can say definitely is that the anisotropy between t_{2g} and e_g orbitals play a certain role.

Experimentally observed d-d peak in Ti 3d-2p RXES of Ti_2O_3 [108] is much weaker than other inelastic spectra even when Ω is tuned at the e_g peak in XAS. Figure 3.11 shows, however, a strong d-d structure. This discrepancy is partly attributed to larger probability for electrons to occupy a d (or t_{2g}) orbital in $|g\rangle$ [6]. In the weak hybridization limit, $|g\rangle$ is trivially $d^\dagger_\sigma|d^0\rangle$, which gives the probability of 1/2 to occupy up or down d orbital. In realistic Ti_2O_3, the probability is only 1/6, resulting in smaller amplitude of the transition from a t_{2g} to a core orbital. In this context, the maximum intensity of the d-d peak would get larger with increasing the occupation number of t_{2g} orbitals, i.e., $Ti_2O_3 < V_2O_3 < Cr_2O_3$, etc.

For the CT structure, Fig. 3.10 shows Ω-dependence similar to the results of the d^0 systems in Fig. 3.4. This is related to the fact that we can successfully define the antibonding state as explained in the preceding section. The lower symmetry of the unperturbed d^1 state, however, disturbs the resonance enhancement of the antibonding

[6] Polarization dependence is another possible reason.

peak as compared to d^0. Analogous to TiO_2, there is a broad satellite structure in experimental Ti $2p$-XAS of Ti_2O_3 [108]. Our results on d^1 systems predict that polarization dependence of the antibonding peak should be observed when Ω is tuned at the satellite structure.

For band insulators, we have confirmed that spatially extended states are in the high energy tail of the main manifold of XAS, and that these states maintain the one-electron character to great extent against the strong U_{dd} and U_{dc}. While we have some extended states also for MH insulators, they are quite unlike the simple one-electron states, but complicated many-electron states involving excitations in the Hubbard bands. It is not necessarily clear what kinds of extended states are created when orbital degeneracies are introduced in. What one can definitely say is that the orbital degrees of freedom relaxes the reduction effect due to the Paul principle, and therefore encourages the dissipation of a photoexcited electron. In any case, the existence of highly delocalized states that are densely distributed over finite width in an absorption threshold is a necessary condition to display the fluorescence-like component in RXES spectra.

3.6 Conclusions

We have discussed the role of orbital degeneracy in metal $3d$-$2p$ RXES with periodic multi-M cluster models under d^0 and d^1 fillings. We first investigated d^0 systems with a single-M cluster model. Calculated RXES spectra showed only Raman component, which is composed of antibonding and nonbonding states. The origin of the antibonding state comes from totally symmetric states as to the permutation of degenerate orbitals, whereas that of the nonbonding state comes from those states which have different symmetry from the unperturbed ground state $|d^0\rangle$. This mathematical definition well explains the Ω-dependence of RXES spectra, which is quantitatively consistent to the experimentally observed resonance enhancement of the antibonding state under a polarized configuration.

With a degenerate multi-M cluster model, we demonstrated that the above properties of local origin are substantially conserved in RXES spectra. Large-cluster effects, however, were observed, first, in the modulation of intensity ratio between two main absorption peaks, and second, in the reduction of the peak separation in the nonbonding structure. Moreover, third, we again confirmed the appearance of the fluorescence-like RXES spectra, which is completely missing in the single-M cluster results. Our result is the first calculation that demonstrates the *coexistence* of the fluorescence-like and Raman components with a periodic Anderson model.

Next we showed calculated results for d^1 systems. RXES spectra calculated with nondegenerate models exhibit only Raman component for both single- and even multi-

M cluster models, but the latter results show considerable Ω-dependence. While a structure due to inter-site d-d transition is enhanced for lower Ω, a structure due to CT is enhanced for higher Ω. Although energy dispersion of UHB slightly reflects on the Ω-dependence, it is too small to explain the occurrence of fluorescence-like spectra in realistic parameter set for Ti oxides.

The most remarkable effect of orbital degeneracy is the appearance of the fluorescence-like spectra in the multi-M cluster calculation, being qualitatively consistent to experimental spectra. The naive conjecture that effective hopping energy reduced by d-d on-site Coulomb interaction hinders the appearance of the fluorescence-like behavior does not hold when the orbital degeneracy is introduced. This result demonstrates the essential importance of the orbital degeneracy as well as the translational symmetry. The appearance of the fluorescence-like spectra seems to be *a general phenomenon that is observed wherever highly delocalized continuum states exist.*

In addition to the fluorescence-like spectra, the orbital degeneracy gives rise to, first, a peak due to the intra-site d-d excitation. The separation between this peak and the elastic line is of order of $10Dq$, but it considerably depends on cluster size. Second, nonbonding states as well as the antibonding state contribute to inelastic spectra. Despite the difference in symmetry of the ground state, the calculated results show Ω-dependence similar to the d^0 case, from which resonance enhancement of the antibonding peak is predicted when Ω is tuned at the XAS satellite structure under polarized configurations.

Chapter 4

Local and Nonlocal Excitations in Cu $4p$-$1s$ Resonant X-Ray Emission Spectra of Nd_2CuO_4

Theoretical study on Cu $4p$-$1s$ RXES of Nd_2CuO_4 is given in the context of local and nonlocal natures of electronic excitations. Detailed analyses with an impurity Anderson model and multi-Cu models are presented, based on the exact diagonalization technique. By investigating partial densities of states, substantial characters of each excited state are clarified. It is demonstrated that a disagreement with experimental data is unavoidable with the impurity model. The key concept to solve the difficulty is Zhang-Rice singlet formation in the intermediate state of RXES. We find that it survives in the final state of RXES as the lowest charge-transfer excitation. The limitation of the impurity model and the essential role of nonlocal excitations in RXES are stressed. [1]

4.1 Introduction

Nd_2CuO_4 is well known as a mother material of n-type superconductor, $Nd_{2-x}Ce_xCuO_{4-y}$ [114], which has attracted special attention in the context of appearance of the electron-hole symmetry [115], a character which single-band models should have. Nd_2CuO_4 has two-dimensional (2D) corner-shared CuO_2 planes with nominally d^9 configuration, which is believed to be essential for high-T_c superconductivity. Recently, Cu $4p$-$1s$ RXES of Nd_2CuO_4 has been measured by Hill and coworkers [116]. The Cu $4p$-$1s$ RXES process is schematically shown in Fig. 4.1. A completely localized $1s$ core electron is resonantly excited to an empty $4p$ conduction band by an incident photon ($\sim$ 9 keV), and then the excited $4p$ electron radiatively comes back to the $1s$ core orbital. In the intermediate state (Fig. 4.1 (b)), a valence hole on the core hole site is strongly scattered to move away to surrounding sites, so that the dynamics of the "dopant" hole such as Zhang-Rice (ZR) singlet formation [43] would be strongly reflected on the RXES spectra. It is interesting to see how the ZR singlet state decays or survives with going to the final states, and to examine what kind of state is created above the insulating gap through varying the incident photon energy.

[1] T. Idé and A. Kotani, J. Phys. Soc. Jpn. **68** (1999) 3100-3109.

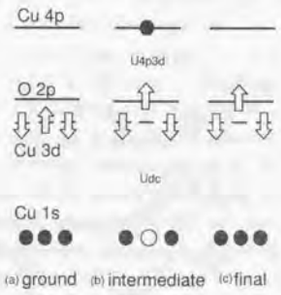

Figure 4.1: Schematic diagram of Cu $1s$-$4p$-$1s$ RXES process. The blank circle and blank arrows represent a $1s$ core hole and up- or down-spin valence holes, respectively. The shaded circles represent $1s$ or $4p$ electrons. (a) The ground state with antiferromagnetic order. (b) THe intermediate state, where a photon excited a $1s$-electron to an empty $4p$ level (the $4p$ band width is disregarded in this figure), creating a $1s$ core hole. The strong repulsive interaction U_{dc} between $3d$ and $1s$ holes gives rise to a charge-transfer (CT) excitation. There is also attractive interaction U_{4p3d} between $4p$ electron and $3d$ hole, but it can not completely compensate U_{dc}. (c) The final state with a CT excitation. The energy difference between the final and ground states is observed as energy loss of the X-ray.

Figure 4.2 shows the experimental data of the Cu $4p_\pi$-$1s$ RXES of Nd_2CuO_4 [116]. The abscissa is the energy loss of X-ray, which is the same as the energy difference between the initial and final electronic states, $E_f - E_g$ [2]. The incident photon energy is taken in the region of Cu $1s$-$4p_\pi$ XAS, which is shown in the upper panels of Fig. 4.3 with the open circles. The first (at 8984 eV) and second (at 8990 eV) features of the Cu $1s$-$4p_\pi$ XAS are denoted by a main peak and a satellite, respectively. It is seen in Fig. 4.2 that an inelastic structure at about 6 eV is observed for 8987.5, 8989 and

[2] It equals $-1\times$(Raman shift). Although the calculated RXES spectra will be arranged as a function of this quantity to compare with the experimental data, we hope that the readers do not confuse them.

8990 eV in addition to the extremely strong elastic peak at zero. The incident photon energy dependence of the 6 eV excitation is shown in the lower panels of Fig. 4.3 with the open circles. We recognize that the 6 eV intensity is strongly enhanced when the incident photon energy is tuned at the satellite of the XAS spectrum, but it indicates almost *no* enhancement at the main peak position.

The aim of this chapter is to give a theoretical interpretation for these experimental data. We will first analyze the experimental data with an impurity Anderson model. The calculated results will be in fair agreement with the experiment, but there exists a conspicuous difference between the theoretical and experimental results: The calculated 6 eV intensity shows a considerable enhancement at the main peak position. In order to remove this discrepancy, we will next use a multi-Cu cluster model. It will be shown that the 6 eV intensity is strongly suppressed at the main peak resonance because of the formation of a ZR singlet in the intermediate state.

The layout of the present chapter is as follows: In the next section, the models used are explained. Numerical analysis with the impurity Anderson model is described in § 4.3. We discuss in § 4.4 the role of the nonlocal screening effects with multi-Cu cluster models. In the last section a brief summary of the present study is given.

4.2 Formulation

We consider a 2D extended periodic Anderson model including Cu $1s$ and Cu $4p$ orbitals, as shown in Fig. 4.4. The explicit form of the Hamiltonian is as follows:

$$H = H_{dp} + H_{pp} + H_{\rm core} + H_{dc} + H_{4p} + H_{4pc} + H_{4p3d}, \tag{4.1}$$

where

$$\begin{aligned} H_{dp} &= -\Delta \sum_{\boldsymbol{R},\sigma} d^\dagger_{\sigma\boldsymbol{R}} d_{\sigma\boldsymbol{R}} + T_{pp} \sum_{\langle \boldsymbol{r},\boldsymbol{r}'\rangle,\sigma} (-1)^{\alpha_1} \left[p^\dagger_{\sigma\boldsymbol{r}} p_{\sigma\boldsymbol{r}'} + \text{H.c.} \right] \\ &+ T_{pd} \sum_{\langle \boldsymbol{R},\boldsymbol{r}\rangle,\sigma} (-1)^{\alpha_2} \left[d^\dagger_{\sigma\boldsymbol{R}} p_{\sigma\boldsymbol{r}} + \text{H.c.} \right] + U_{dd} \sum_{\boldsymbol{R}} d^\dagger_{\uparrow\boldsymbol{R}} d_{\uparrow\boldsymbol{R}} d^\dagger_{\downarrow\boldsymbol{R}} d_{\downarrow\boldsymbol{R}}, \end{aligned}$$

$$H_{pp} = U_{pp} \sum_{\boldsymbol{r}} p^\dagger_{\uparrow\boldsymbol{r}} p_{\uparrow\boldsymbol{r}} p^\dagger_{\downarrow\boldsymbol{r}} p_{\downarrow\boldsymbol{r}}, \tag{4.2}$$

$$H_{\rm core} = \varepsilon_{1s} \sum_{\boldsymbol{R}} S^\dagger_{\boldsymbol{R}} S_{\boldsymbol{R}}, \tag{4.3}$$

and

$$H_{dc} = U_{dc} \sum_{\boldsymbol{R}} \left[\sum_\sigma d^\dagger_{\sigma\boldsymbol{R}} d_{\sigma\boldsymbol{R}} \right] S_{\boldsymbol{R}} S^\dagger_{\boldsymbol{R}}. \tag{4.4}$$

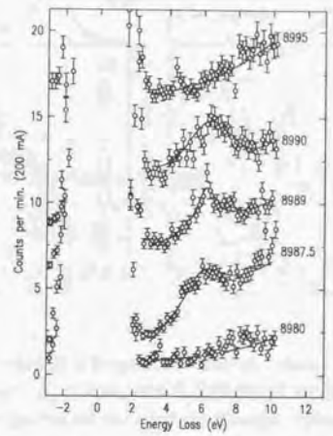

Figure 4.2: Cu $4p_\pi$-$1s$ RXES of Nd_2CuO_4 [116] as a function of energy loss. Incident photon energies are tuned in the range of $1s$-$4p_\pi$ absorption. The polarization vector of the incident X-ray has an angle 60° to the CuO_2 planes, and its momentum-transfer is perpendicular to those (see Fig. 5.2 (a)). The excitation energies are indicated in the upper panels of Fig. 4.3 with vertical bars.

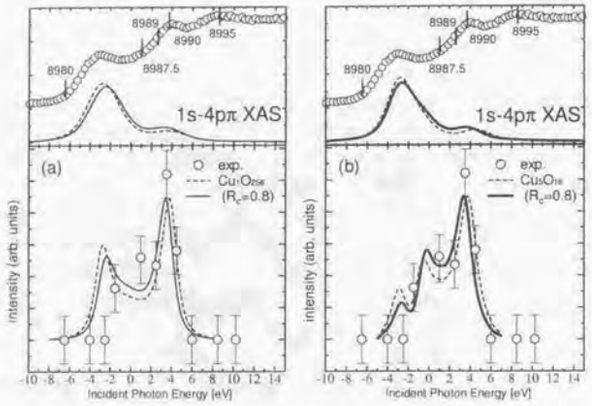

Figure 4.3: (a) *Lower panel*: The 6 eV intensity as a function of the incident photon energy in Cu $4p_\pi$-$1s$ RXES of Nd_2CuO_4. The open circles represent the experimental result by Hill *et al.* [116]. The solid and dashed curves represent calculated results with a Cu_1O_{256} cluster for $R_c = 0.8$ and 1.0, respectively. In accordance with the experimental resolution [116], all the calculations are convoluted with Gaussian $\Gamma_G = 0.95$ eV (HWHM) for the scattered photon, and $\Gamma_G = 0.3$ eV for the incident photon. *Upper panel*: The open circles represent experimental Cu K-XAS of Nd_2CuO_4 [117], where the polarization vector of the X-ray is 60° to the CuO_2 plane (see Fig. 5.2 (a)). The definition of the two curves are the same as the lower panel, although they are convoluted with Lorentzian $\Gamma_L = 0.8$ eV (HWHM) to take in lifetime effects, and further with $\Gamma_G = 0.8$ eV to reproduce the experimental line width. (b) The same as (a), but calculated curves are obtained with a Cu_5O_{16} cluster. The calculated XAS spectra are broadened with $\Gamma_L = 0.8$ eV and $\Gamma_G = 1.2$ eV.

In these equations, $d^\dagger_{\sigma \boldsymbol{R}}$ creates a Cu $d_{x^2-y^2}$ *hole* with σ spin at $\boldsymbol{R}$ site and $p^\dagger_{\sigma \boldsymbol{r}}$ creates a σ-bonded O $2p$ *hole* with σ spin at $\boldsymbol{r}$ site. Δ (> 0) is the charge-transfer (CT) energy between the p and d orbitals, and intersite hopping energy T_{pp} and T_{pd} are related with the Slater-Koster parameters [118] as $T_{pp} = [(pp\pi) - (pp\sigma)]/2$ and $T_{pd} = \sqrt{3}(pd\sigma)/2$. The signs of T_{pp} and T_{pd} are described by α_1 and α_2, which are 0 or 1, depending on the relative position of a nearest-neighbor O-O and Cu-Cu pair, respectively. $S^\dagger_{\boldsymbol{R}}$ creates a Cu $1s$ *electron* at $\boldsymbol{R}$ site. U_{dd} and U_{dc} are on-site Cu $3d$-$3d$ and Cu $3d$-$1s$ Coulomb repulsion energies, respectively.

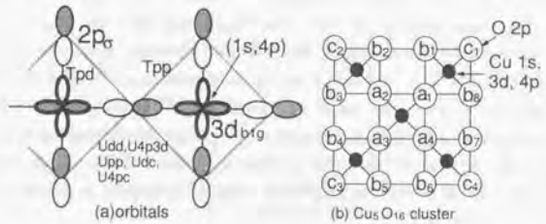

Figure 4.4: Geometry of the system. (a) Orbitals in the model. O $2p_\sigma$ and Cu $\{1s,\ 3d(b_{1g}),\ 4p_\pi\}$ orbitals are taken into account. The blank (shaded) area of the ellipses represents positive (negative) phase. (b) The Cu_5O_{16} cluster with open boundary condition. The oxygen sites are discriminated with $\{a_i, b_i, c_i\}$ to construct molecular orbitals in the next section.

Generally, Cu $4p$ states are split off into a_2 ($4p_\pi$) and e ($4p_\sigma$) symmetries in terms of the local D_{4h} irreducible representations. For $4p$-$1s$ RXES of Nd_2CuO_4, however, both contributions are separable because there is no overlap between the experimental $4p_\pi$ and $4p_\sigma$ absorption threshold. We only take into account the $1s$-$4p_\pi$-$1s$ transition process. The polarization dependence of Cu $4p$-$1s$ RXES will be discussed in the next chapter. Then H_{4p} is given by

$$H_{4p} = \varepsilon_{4p\pi} \sum_{\boldsymbol{R}} Q^\dagger_{\boldsymbol{R}} Q_{\boldsymbol{R}} + t_0 \sum_{\langle \boldsymbol{R}, \boldsymbol{R}' \rangle} Q^\dagger_{\boldsymbol{R}} Q_{\boldsymbol{R}'}, \tag{4.5}$$

where $Q^\dagger_{\boldsymbol{R}}$ creates a Cu $4p_\pi$ *electron* at $\boldsymbol{R}$ site, t_0 is $4p_\pi$-$4p_\pi$ nearest-neighbor hopping energy.

H_{4pc} and H_{4p3d} describe Cu $4p_\pi$-$1s$ and Cu $4p_\pi$-$3d$ intra-atomic interactions, re-

spectively. The explicit forms are

$$H_{4pc} = -U_{4pc} \sum_{\boldsymbol{R}} Q^\dagger_{\boldsymbol{R}} Q_{\boldsymbol{R}} S_{\boldsymbol{R}} S^\dagger_{\boldsymbol{R}} \tag{4.6}$$

and

$$H_{4p3d} = -U_{4p3d} \sum_{\boldsymbol{R}} Q^\dagger_{\boldsymbol{R}} Q_{\boldsymbol{R}} \sum_{\sigma} d^\dagger_{\sigma \boldsymbol{R}} d_{\sigma \boldsymbol{R}}. \tag{4.7}$$

In accordance with systematics of high-T_c compounds discussed by Ohta *et al.* [119] and with an *ab initio* calculation [120], we set the valence electron parameters for large-cluster calculations of Nd_2CuO_4 as $\Delta = 2.5$, $T_{pd} = 1.21$, $T_{pp} = 0.55$ and $U_{dd} = 2U_{pp} = 8.8$ [eV]. A band calculation for Nd_2CuO_4 [121] gave the $4p_\pi$ band width $W_\pi = 2.5$. Thereby we estimate $t_0 = 0.3$ eV, along with one-electron formula of the bandwidth $W_\pi = 8t_0$. U_{dc}, U_{4p3d} and U_{4pc} are set to be 7.5, 3.0 and 4.0 [eV].

In addition to the above model, we define an impurity Anderson model, which contains all O $2p$ and Cu $4p$ orbitals in H, as well as the central Cu $3d$ and $1s$ orbitals. Since the system we are interested in have nominally d^9 configuration in the electron picture, the impurity problem is necessarily a one-hole problem with one electron in the $1s$ orbital or the $4p$ orbitals. In order to keep the main-satellite energy separation of XAS to be the same as that of the large cluster model, a different parameter $\Delta = 1.5$ eV is used for this model [86].

As far as the $1s$-$4p_\pi$ absorption process is concerned, the absorption operator T_a is given by

$$T_a = \sum_{\boldsymbol{R}} \mathrm{e}^{-\mathrm{i}\boldsymbol{q}_1 \cdot \boldsymbol{R}} Q^\dagger_{\boldsymbol{R}} S_{\boldsymbol{R}}, \tag{4.8}$$

where $\boldsymbol{q}_1$ is the wave vector of the incident photon. The emission operator T_e is defined as $(T_a)^\dagger$ with the substitution of $\boldsymbol{q}_1$ with $\boldsymbol{q}_2$, which is the wave vector of the emitted photon. Then the transition operator of the $4p_\pi$-$1s$ RXES can be written as

$$T(\Omega) = \sum_{\boldsymbol{R}} S^\dagger_{\boldsymbol{R}} Q_{\boldsymbol{R}} G_0(\Omega) Q^\dagger_{\boldsymbol{R}} S_{\boldsymbol{R}}, \tag{4.9}$$

where $G_0(\Omega)$ is the resolvent operator defined as $G_0(\Omega) = (\Omega + E_g - H + \mathrm{i}\Gamma)^{-1}$. E_g and Ω are energies of the ground state and the incident photon, respectively. We set $\Gamma = 0.8$ eV in the present calculations, considering semi-empirical data of the Auger process [122], and another calculation of RXES for $3d$ systems [123]. In the above equation, we assume that $\boldsymbol{q} = \boldsymbol{q}_2 - \boldsymbol{q}_1$ is perpendicular to the CuO_2 plane in accordance with the experiment. The polarization dependence [117] and the $\boldsymbol{q}$ dependence [152] of RXES will be discussed in the next chapter. To make sure, the explicit forms of spectral functions of XAS and RXES are

$$F_{\mathrm{XAS}}(\Omega) = \sum_{\mu} |\langle \mu | T_a | g \rangle|^2 \delta(\Omega + E_\mu - E_g) \tag{4.10}$$

and

$$F_{\mathrm{RXES}}(\omega; \Omega) = \frac{1}{N} \sum_{f \neq g} |\langle f | T(\Omega) | g \rangle|^2 \delta(\omega - \Omega + E_f - E_g), \tag{4.11}$$

where E_μ (E_f) is a final state energy of XAS (RXES), and ω denotes the emitted photon energy. N is the number of the Cu atoms.

4.3 Analysis with Impurity Anderson Model

4.3.1 Properties of eigenstates

It is well-known that the eigenequation of the impurity Anderson model is exactly constructed as $x - \varepsilon_d = \Sigma_\star(x)$, where ε_d is unperturbed energy of the d orbital, and $\Sigma_\star(x)$ is the self-energy function [124]:

$$\Sigma_\star(x) = \frac{1}{N} \sum_{j\boldsymbol{k}} \frac{|V_{j\boldsymbol{k}}|^2}{x - \varepsilon_{j\boldsymbol{k}} - \mathrm{i}0}.$$

For the 2D periodic system with Cu-O distance a, there are two oxygen $2p$ bands:

$$\varepsilon_{j\boldsymbol{k}} = \begin{cases} 4T_{pp}\sin(k_x a)\sin(k_y a) & , j = 1 \\ -4T_{pp}\sin(k_x a)\sin(k_y a) & , j = 2 \end{cases}.$$

For each band, the d-p hybridization energy is

$$V_{j\boldsymbol{k}} = \begin{cases} -\sqrt{2}\mathrm{i}T_{pd}[-\sin k_x a + \sin k_y a] & , j = 1 \\ -\sqrt{2}\mathrm{i}T_{pd}[\sin k_x a + \sin k_y a] & , j = 2 \end{cases}.$$

The graphical representation of the eigenequation is depicted in Fig. 4.5. We see that a bound state exists at -4.3 eV. This is the ground state $|g\rangle$. The above equation still holds for the intermediate state under substitution of ε_d with $\varepsilon_d + U_{dc} - U_{4p3d}$, as far as the energy dispersion of the $4p$ electron is neglected. In this case we have two bound states M and S, as described in the figure.

In order to study properties of the eigenstates further, we calculate partial density of states (PDOS) which is defined as

$$\rho_\phi(\varepsilon) = \sum_n |\langle \phi | \varepsilon_n \rangle|^2 \delta(\varepsilon - \varepsilon_n) \tag{4.12}$$

for a ϕ orbital. $|\varepsilon_n\rangle$ is an eigenstate of the system. [3]

[3] Several authors have tried to decompose calculated spectra according to *different* point group symmetry, see *e.g.* Ref. [127]. We here define this function in order to investigate contribution of a set of state vectors with a *same* point group symmetry but different spatial extent.

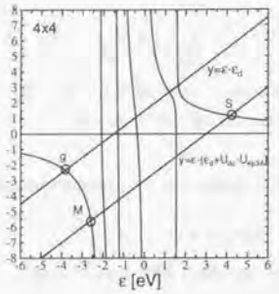

Figure 4.5: Graphical representation of the eigenquations of the 2D impurity Anderson model with 4×4 oxygen network.

By constructing molecular orbitals with b_{1g} symmetry around the impurity site, it can be easily shown that the impurity Anderson model is equivalent to the model shown in Fig. 4.6. A is the nearest-neighbor orbitals to the Cu site, which is defined by

$$A^\dagger = \frac{1}{2}(-a_1^\dagger + a_2^\dagger + a_3^\dagger - a_4^\dagger). \tag{4.13}$$

Starting with this, we come to more accurate description of the whole system by taking B, C, ... molecular orbitals, where B and C are defined by

$$B^\dagger = \frac{1}{\sqrt{8}}(b_1^\dagger - b_2^\dagger + b_3^\dagger + b_4^\dagger - b_5^\dagger + b_6^\dagger - b_7^\dagger - b_8^\dagger) \tag{4.14}$$

and

$$C^\dagger = \frac{1}{2}(-c_1^\dagger + c_2^\dagger + c_3^\dagger - c_4^\dagger), \tag{4.15}$$

respectively. Since they span the complete set, note that a sum rule $\sum_\phi \rho_\phi = \rho$ as well as $\int d\varepsilon \rho_\phi = 1$ holds, ρ representing the total density of states (TDOS).

Figure 4.7 (a) shows PDOS of $3d$ and the A, B and C orbitals as well as TDOS for RXES final state. We see that ρ_d and ρ_A have definite peaks at the ground state and at around 5.2 eV. The energy separation is approximately equal with the value obtained from the formula of the bonding-antibonding separation [86]

$$W = \sqrt{(-\Delta + 2T_{pp})^2 + 16T_{pd}^2}$$

in the simple CuO_4 cluster. This implies that the 5.2 eV peak corresponds to the antibonding state. Since these bonding and antibonding orbitals are just two ones in

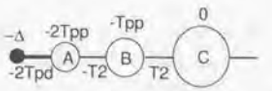

Figure 4.6: A equivalent model of the 2D impurity Anderson model. The closed and open circles represent the impurity $3d$ orbital and O $2p$ molecular orbitals, respectively. The diagonal elements of the equivalent Hamiltonian are described above each of the circles. The hybridization matrix elements are described below each bond, where $T_1 = \sqrt{2}T_{pp}$ and $T_2 = \sqrt{2}T_{pd}$. Note that there happen to be degeneracies in molecular orbitals beyond C.

the simple CuO_4 cluster, the 5.2 eV excitation is nearly local, i.e. the hole spend most of its time at the plaquette with the impurity [4].

On the other hand, we notice that the state at about 2 eV has little d and A weight. This means that it is a nearly pure p state, which has little amplitude at the impurity plaquette. In other words, it is a nonlocally excited state. This character makes a sharp contrast to the ground state and the 5.2 eV excited state, and it is directly reflected in the Ω dependence of RXES.

4.3.2 XAS

Figure 4.7 (b) shows calculated Cu $1s$-$4p$ XAS and PDOS for the intermediate (XAS final) state. The energy dispersion of the $4p$ electron is neglected in the calculation of PDOS for simplicity, but it is fully included in that of XAS. We observe a doubly-peaked structure in the calculated XAS spectrum, which has been plotted with the dashed curve also in Fig. 4.3 (a). The energy separation between the main and satellite peaks is consistent to that of the experimental $1s$-$4p_\pi$ XAS spectrum. If we subtract contribution of a steeply increasing background spectrum due to the secondary electron emission process [125, 126] from the experimental one, these two spectra would broadly agree.

We see that the major weight of the main peak of XAS, which is denoted by $|M\rangle$ hereafter, lies on the A orbital. This is consistent with the standard notation $\underline{c}d^{10}\underline{L}$ in the electron picture, but there are no little weights in both d and C orbitals. The satellite peak of XAS, which is denoted by $|S\rangle$ hereafter, is composed mainly of the d orbital and slightly of the A orbital, being consistent with the standard notation $\underline{c}d^9$.

[4] More exactly, this excitation energy, which corresponds to the experimental value 6 eV, depends on the model, and takes 5.2 eV for the impurity Anderson model, 5.5 eV for Cu_3O_{10} cluster model and 5.7 eV for Cu_5O_{16} cluster model.

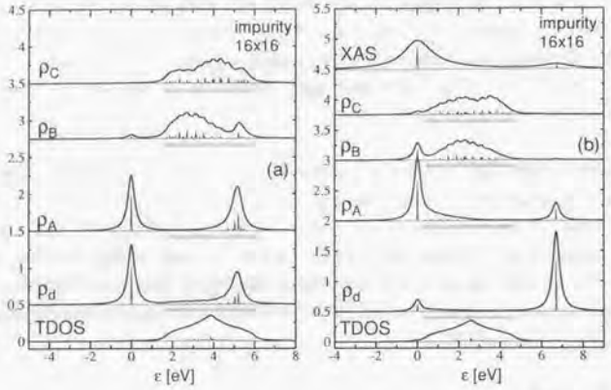

Figure 4.7: (a) Total and partial densities of states of the impurity $3d$ orbital and O $2p$ molecular orbitals (A, B and C) defined in the text. TDOS and PDOS's are calculated with the impurity Anderson model with $N = 16 \times 16$ oxygen network, and they are convoluted with Lorentzian $\Gamma_L = 0.2$ eV (HWHM). All densities are normalized so that the integrated areas are to be unity. The shaded bars are guide to eye to represent unperturbed O $2p$ band width. (b) Total and partial densities of states (PDOS) in the *intermediate* state. The energy dispersion of the $4p$ electrons is disregarded for simplicity to calculate PDOS, but it is fully included to calculate XAS. The Cu $1s$-$4p_\pi$ XAS spectrum is convoluted with $\Gamma_L = 0.8$ eV. For both (a) and (b), the origin of the abscissa is adjusted to the lowest eigenenergy.

As seen from Fig. 4.7 (a), $|g\rangle$ as the initial state of XAS consists of d and A orbitals approximately in the ratio of 5 : 5. Large weight in these orbitals is a necessary condition to have a strong intensity in XAS. Although $|M\rangle$ and $|S\rangle$ similarly fulfill the condition, Fig. 4.7 (b) shows that their XAS intensities are quite different. The reason comes from a phase cancellation mechanism. Both $|g\rangle$ and $|M\rangle$ are split-off states at lower energy side of the continuum, whereas $|S\rangle$ is the split-off one at the opposite side. Thus we have considerable phase cancellation in the process $|g\rangle \to |S\rangle$.

4.3.3 RXES

Calculated results of the Cu $4p_\pi$-$1s$ RXES are shown in Fig. 4.8, where CT excitations appear as inelastic spectra. The elastic peak is omitted from each spectrum.

Roughly speaking, we have broader spectra when Ω is tuned at M, whereas a single feature at around 5.2 eV appears for other Ω. As discussed in the preceding subsection, the value 5.2 eV is nearly the same as the bonding-antibonding separation in CuO_4 cluster. Within the present parameters, it is approximately given by $W \simeq 4T_{pd}$. The lowest position of the inelastic peak is estimated as the energy difference between the bottom of the p band and the bonding state in CuO_4 cluster:

$$-4T_{pp} - \frac{1}{2}(-\Delta - 2T_{pp} - W) \simeq \frac{\Delta}{2} + 2T_{pd} - 3T_{pp}.$$

This formula gives a rough estimation of the CT gap from the viewpoint of the impurity Anderson model. Since it is believed that $(\Delta - 2T_{pp})$ is the same order of T_{pd} for high-T_c compounds, note that a naive estimation $\varepsilon_{\rm gap} \simeq \Delta$ which comes from the simple limit of weak d-p hybridization does not hold.

We now discuss the Ω dependence of RXES. First we consider the case when Ω is at $|S\rangle$. This intermediate state is strongly localized in the impurity plaquette, as shown in Fig. 4.7 (b). Moreover, the phase of it matches the 5.2 eV excitation well by the aforementioned reason. Thus the main peak of RXES appears around 5.2 eV.

Second, $|M\rangle$ has not a little weight in extended orbitals such as B. Since $|M\rangle$ is much closer to the continuum than $|g\rangle$ in Fig. 4.5, it well hybridizes with p orbitals. The limit $U_{dc} \to \infty$ is helpful to illustrate the situation. The d hole is completely pushed out to the p bands in this case, naturally getting over the nearest-neighbor ligand orbital. In this sense, $|M\rangle$ as well as the 2 eV excitation has a nonlocal character, through which the transition from $|M\rangle$ to the states around 2 eV is caused. $|M\rangle$ has also large weight in A, so that the overlap with the 5.2 eV excitation is large, although there is no reason for the intensity enhancement by the phase matching in this case. This brings about the emission intensity around 5.2 eV, resulting in the broader spectra.

Finally, since the absorption intensity in the region between $|M\rangle$ and $|S\rangle$ is extremely small, spectral shapes of 2, 3 and 4 in Fig. 4.8 are substantially determined by

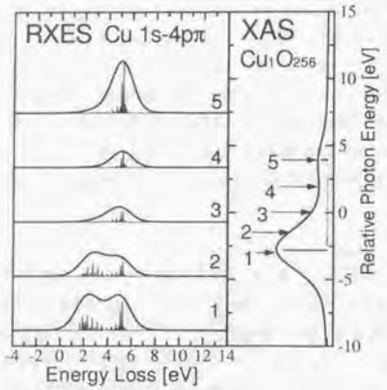

Figure 4.8: Calculated Cu $4p_\pi$-$1s$ RXES and XAS spectra for the Cu_1O_{256} cluster (impurity Anderson model). The arrows indicate the incident photon energies, and their numbers correspond to those in RXES.

virtual transition process, although the 2 eV excitation is slightly favorable for these intermediate states which have large extended p weight.

4.3.4 Excitation energy dependence of the 5.2 eV intensity

Let us consider the mechanism of the Ω-dependence of the inelastic peak intensity around 5.2 eV. For the CuO_4 cluster, there are only two states in the final states of RXES. The intermediate states are also spanned in two-dimensional Hilbert space as far as the energy dispersion of $4p$ electron is disregarded, so that $|M\rangle\langle M| + |S\rangle\langle S| = 1$ holds. Since the line width Γ is much smaller than the energy separation between S and M, we have the following identity between transition amplitudes $|g\rangle \to |5.2\rangle$ through M and S intermediate states:

$$\begin{aligned} &\langle 5.2|T_e|M\rangle \frac{1}{i\Gamma}\langle M|T_a|g\rangle + \langle 5.2|T_e|S\rangle \frac{1}{i\Gamma}\langle S|T_a|g\rangle \\ = \; &\frac{1}{i\Gamma}\langle 5.2|T_e T_a|g\rangle = \frac{1}{i\Gamma}\langle 5.2|g\rangle = 0, \end{aligned}$$

which demonstrates that the two amplitudes are the same except for their signs, and thus the Ω-scan of the 5.2 eV intensity takes a symmetric "U-shape". We then take its asymmetry as a measure of nonlocal nature of excitations.

The Ω-scan is plotted in Fig. 4.3 (a) with the dashed curve [5]. It shows that the scan takes almost the U-shape, and that the large-cluster effect with respect to O $2p$ band plays a minor role. It suggests that the transition process which gives the 5.2 eV excitation as a final state of RXES is mainly ruled by local orbitals such as d and A.

Recently Nakazawa *et al.* [94] pointed out the importance of configuration dependence [128] of cation-ligand hybridization in Ce $4f$-$3d$ RXES of CeO_2. In order to see the effect, we here introduce a parameter R_c, which renormalizes T_{pd} of the plaquette with the core hole as $R_c \times T_{pd}$ in the *intermediate* (XAS final) states.

The calculated results with $R_c = 0.8$ are also given in Fig. 4.3 (a) (solid curve). All calculated scans are normalized so that each height of the maximum peak is the same. We see that $R_c \neq 1$ suppresses the 5.2 eV intensity (although the suppression is too small to reproduce the experimental result) when Ω is tuned around $|M\rangle$, and strengthens its asymmetry. The limit of $R_c \to 0$ helps to make the situation clear. Since the main peak of XAS has no d weight in this case, and moreover the orbital A is not stabilized through d-p hybridization, the extra p weight contained in the extended $B, C, \ldots$ orbitals necessarily comes into the state to reduce the large A weight. Also for a finite R_c, it must work to increase the extended weight in $|M\rangle$. Thus overlap between $|M\rangle$ and the 5.2 eV excitation tends to be decreased by R_c in comparison with that of $|S\rangle$. This is the explanation of the asymmetric shape of the Ω-scan of the 5.2 eV intensity.

Although the calculated XAS with the impurity Anderson model well reproduces the experimental main-satellite separation, there are considerable discrepancies with experimental data in the Ω-scan of the 5.2 eV intensity. When Ω is tuned at the main peak of XAS, the 5.2 eV intensity always exhibits one of the two peaks of the U-shape as far as the impurity Anderson model is used. The observed suppression effect can not be reproduced at all. This is nothing but an indication of a nonlocal effect (which is brought about by Zhang-Rice singlet formation) in the intermediate states of multi-Cu clusters, beyond the simple O $2p$ band effects. It will be discussed in the next section in detail.

4.4 Analysis with Multi-Cu Models

4.4.1 Properties of eigenstates

Considering the results with the impurity Anderson model and the experimental fact that an antiferromagnetic order of d holes is realized in $|g\rangle$, we are led to an idea that

[5] The present result is essentially the same as that given in Ref. [116] with an impurity Anderson model, but quantitatively they are slightly different because of a slightly different O $2p$ band model and slightly different parameter values.

eigenstates of a multi-Cu cluster model are described as some superposition of those of each plaquette [129]. We expect that there are relatively local excitations around 5.2 eV, but somewhat new states should be created around 2 eV above $|g\rangle$ upon going from the impurity to the multi-Cu model.

In order to see the point in detail, we again calculate PDOS and TDOS for a Cu_3O_{10} cluster with Householder method [79], based on the fact that spectra of Cu_3O_{10} are essentially the same as that of Cu_5O_{16}. We choose

$$|\mathrm{AF}\rangle = d^\dagger_{1\uparrow} d^\dagger_{2\uparrow} d^\dagger_{0\downarrow} |\mathrm{vacuum}\rangle,$$

as a counterpart of $|d\rangle$ in the impurity model, and

$$|A'\rangle = L^\dagger_{0\downarrow} d_{0\downarrow} |\mathrm{AF}\rangle,$$

as a counterpart of $|A\rangle$, where the suffix 0 means the central site, and $L^\dagger_{0\downarrow}$ is the creation operator of its nearest-neighbor ligand orbital with local b_{1g} symmetry of the local D_{4h} group, just as eq. (4.13). The numbering rule is given in the inset of Fig. 4.9 (a).

In addition to these, we define also $|B'\rangle = B^\dagger_{0\downarrow} d_{0\downarrow} |\mathrm{AF}\rangle$ and $|C'\rangle = C^\dagger_{0\downarrow} d_{0\downarrow} |\mathrm{AF}\rangle$, where $B^\dagger_{0\sigma}$ and $C^\dagger_{0\sigma}$ are defined by

$$B^\dagger_{0\sigma} = \frac{1}{2}(b^\dagger_{1\sigma} - b^\dagger_{2\sigma} + b^\dagger_{3\sigma} - b^\dagger_{4\sigma}), \tag{4.16}$$

and

$$C^\dagger_{0\sigma} = \frac{1}{\sqrt{2}}(c^\dagger_{1\sigma} - c^\dagger_{2\sigma}), \tag{4.17}$$

respectively. The orbitals $L^\dagger_{0\sigma}$, $B^\dagger_{0\sigma}$ and $C^\dagger_{0\sigma}$ have a_g symmetry in terms of the D_{2h} irreducible representation of the Cu_3O_{10} cluster, so that all the above states have the same symmetry (B_{3u}) as the ground state.

The result of the final state is shown in Fig. 4.9 (a) within the energy range corresponding to the one-hole CT excitation ($E - E_g$ less than about 7 eV). We see that ρ_{AF} and $\rho_{A'}$ have definite structures at the ground state and at 5.5 eV. These features are similarly observed in Fig. 4.7. We thus conclude that the 5.5 eV excitation is nearly localized in each plaquette, i.e. "intra-plaquette" excitation.

There are also some structures in the energy region between $|g\rangle$ and the 5.5 eV excitation, which are not observed in Fig. 4.7. A detailed calculation shows that the peak g_1 has large overlap with states which have frustrated d-spin arrangements such as

$$\frac{1}{\sqrt{N_u}} \sum_{i=1}^{N_u} (-1)^{\alpha_i} d^\dagger_{i\downarrow} d_{i\uparrow} d^\dagger_{0\uparrow} d_{0\downarrow} |\mathrm{AF}\rangle,$$

where N_u is the number of up-spin hole, and α_i is determined so that the state is the B_{3u} representation of the overall symmetry group D_{2h}. Thus we conclude that the peak is due to spin excitations.

Figure 4.9 (a) also shows PDOS's and TDOS of $T_{pp} = 0$ with the dashed curves. It is observed that a few peaks between 2 and 3 eV survive with slight energy shifts. Since the impurity Anderson model is reduced to the CuO_4 cluster in this limit, we conclude that the existence of d-p network particular to multi-Cu models is their origin. In order to study the properties of these peaks we here define a new PDOS for

$$|Z\pm\rangle = \frac{1}{\sqrt{2}}(z^\dagger_{1\pm} d_{1\uparrow} + z^\dagger_{2\pm} d_{2\uparrow}) d_{0\downarrow} |\mathrm{AF}\rangle, \tag{4.18}$$

where the operator $z^\dagger_{i\pm}$ is defined by

$$z^\dagger_{i\pm} = \frac{1}{\sqrt{2}}(d^\dagger_{i\uparrow} L^\dagger_{i\downarrow} \pm d^\dagger_{i\downarrow} L^\dagger_{i\uparrow}). \tag{4.19}$$

$|Z-\rangle$ ($|Z+\rangle$) describes a state where a hole pushed out from the central plaquette forms a local singlet (triplet) at the nearest-neighboring plaquettes. The phase factor in eq. (4.18) was determined so that its global symmetry is in agreement with that of the ground state (B_{3u}).

According to the calculated result, ρ_{Z-} has clear structure (Z_1) between 2 and 3 eV, but little weight in ρ_{Z+}. Although the impurity Anderson model contains the nearly pure p states in this energy range, this result suggests that *the CT excitation in this energy range has ZR singlet like character*. Hence the CT gap may be defined by the energy to move a hole from the bonding orbital at a plaquette to the surroundings, where the local singlet is formed. If $2T_{pd} \ll \Delta$ held as Zhang and Rice originally discussed [43], the binding energy of the local singlet would be estimated by their formula $-8T^2_{pd}[1/\Delta^2 + 1/(U_{dd} - \Delta)^2]$. However, our parameter gives $2T_{pd} \simeq \Delta$. We hence obtain the conclusion again that the simple estimation that $\varepsilon_{\mathrm{gap}} \simeq \Delta$ does *not* hold. This point is made still clearer by studying Cu $4p$-$1s$ RXES of $CuGeO_3$, which has relatively larger Δ [130, 131]. In fact, our recent calculation shows that the charge gap is approximately half of Δ in $CuGeO_3$. The detailed discussion will be published elsewhere.

Except for this fact, PDOS's in Fig. 4.7 and 4.9 have much in common. For example, the 2 eV excitation has hardly AF weight, but has relatively large weight in $\rho_{B'}$ and $\rho_{C'}$.

Similar arguments are applicable to the intermediate state. The calculated results are given in Fig. 4.9 (b) for the system with a core hole at the central site. The energy dispersion of $4p$ electron is neglected to calculate PDOS. It is clearly shown that AF weight is transferred to about 6.6 eV higher than the lowest energy state, being denoted by "S". Naturally, the main structure in ρ_{AF} corresponds to $\underline{c}d^9$ in the standard notation of the impurity Anderson model.

In addition, first, we can assign the lowest energy feature "Z" to the state with the local singlet (*not* triplet). This is the direct evidence of appearance of the ZR

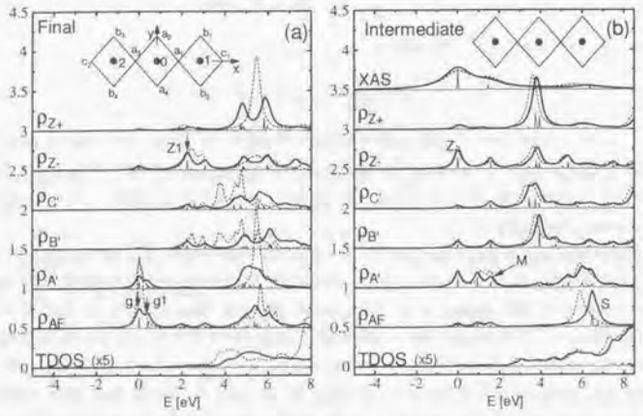

Figure 4.9: (a) Total and partial densities of states in RXES final state for Cu_3O_{10} cluster, whose structures are shown in the panel. The definition of the state |AF⟩ and so on is given in the text. The solid and dashed curves represent the results with $T_{pp} = 0.55$ and 0, respectively. (b) TDOS and PDOS in the intermediate (XAS final) state, and Cu $1s$-$4p_\pi$ XAS spectrum. The energy dispersion of the $4p$ electron is disregarded to calculate PDOS, but fully included to calculate XAS. The solid and dashed curves are obtained with $R_e = 1.0$ and 0.8, respectively. For both (a) and (b), the origin of the abscissa is adjusted to be the lowest eigenenergy, and all spectra are broadened with Lorentzian ($\Gamma_L = 0.2$ eV), whose integrated areas are normalized to be unity.

singlet in the intermediate state, also in the final state of $2p$-XPS first discussed by van Veenendaal *et al.* [41], i.e. a hole pushed out by the corehole potential moves to the neighboring plaquettes to form the local singlet. Second, structures about 1.5 eV above the ZR state is attributed to a charge-transferred state having a considerable weight in the nearest-neighbor orbital of the core hole site, corresponding to $|M\rangle$ of the impurity Anderson model.

Figure 4.9 (b) also shows Cu $1s$-$4p_\pi$ XAS. In contrast to the impurity Anderson model, there are three structures in XAS, which are the above discussed Z, M and S. This interpretation has close relationship with that of $2p$-XPS [86, 88].

4.4.2 RXES

Figure 4.10 shows XAS and RXES spectra with the Cu_5O_{16} cluster with open boundary condition. Calculated spike spectra of RXES are convoluted with Gaussian $\Gamma_G = 0.95$ eV (HWHM) in accordance with the experimental resolution [116]. XAS is also broadened with Lorentzian $\Gamma_L = 0.8$ to consider the lifetime effect and $\Gamma_G = 0.8$ eV to reproduce the experimental peak width. To avoid boundary effects, the core hole is fixed to the central site for both RXES and XAS. Effects of spatial coherence are discussed separately in the next chapter in the context of momentum-transfer dependence [152].

As is the case of the impurity Anderson model, RXES in Fig. 4.10 have two structures around 2 and 5.7 eV, which are hereafter symbolically denoted by $|2\rangle$ and $|5.7\rangle$, respectively. The latter value is somewhat larger than that of the impurity and Cu_3O_{10} models, but closer to the experimental value.

The 2 eV intensity is considerably enhanced when the incident photon energy Ω is tuned at the main peak "1" of XAS. This is observed in common with the case of the impurity Anderson model, but the enhancement is extremely intense in this case. The reason is that both 2 eV excitation and the main absorption peak have a ZR singlet, so that their overlap is very large. Because of the extremely strong elastic scattering, the 2 eV peak is hardly observed in Fig. 4.2. It is established from experimental [132] and theoretical results [133, 134] in the optical conductivity that the charge gap of undoped high-T_c cuprates is of order of 2 eV. A recent high-resolution experiment in Cu $4p$-$1s$ RXES of $Sr_2CuO_2Cl_2$ [135] successfully observes the 2 eV peak. For the relative intensity of the 2 eV peak as compared to the 5.7 eV one, the spatial coherence of the core orbitals seems to play some role. We have fixed the core hole to the central Cu site in the present calculation. Roughly speaking, this corresponds to that situation, where RXES spectra with all kinds of the momentum transfer $\boldsymbol{q}$ are mixed up. As will be suggested by a $\boldsymbol{q}$-dependent calculation in the next chapter [6], the 2 eV peak might be excessively highlighted under this situation, as compared to the experimental

[6] See Fig. 5.9.

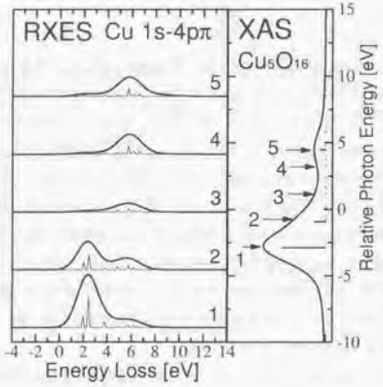

Figure 4.10: Calculated Cu $4p_\pi$-$1s$ RXES and XAS spectra with the Cu_5O_{16} cluster model. The core hole is fixed to the central site in order to avoid boundary effects. The arrows marked with numbers in XAS indicate incident photon energies, and the numbers in RXES represent the corresponding excitation energies.

data, where $\boldsymbol{q}$ is perpendicular to the CuO_2 plane. At any rate, one needs experimental studies with higher resolution and theoretical studies with larger clusters for detailed discussion on the 2 eV peak.

On the other hand, since $|5.7\rangle$ is the intra-plaquette excitation, corresponding to the 5.5 eV excitation of Cu_3O_{10} cluster discussed in the preceding subsection, the overlap with the ZR state is expected to be quite small. The ZR state contains a plaquette with almost no hole. As a result, the 5.7 eV intensity is suppressed when Ω is tuned at the XAS main peak. We believe that this is the fundamental mechanism of the experimental suppression effect. Note that this conclusion is hardly affected by the above-mentioned spatial coherence of the core orbitals, because of the intra-plaquette nature of $|5.7\rangle$.

Since the satellite peak "5" has the dominant weight in AF as shown in Fig.4.9 (b), it is likely for this state to have large overlap with $|5.7\rangle$, the state almost localized at each plaquette. This coupling would be preferred also from the phase matching point of view. In addition, it is expected to have little overlap with the 2 eV excitation containing the ZR singlet like state. Thus the RXES spectrum has an only structure around the 5.7 eV excitation.

When Ω is tuned at the shoulder "2", which was denoted by M in the preceding subsection, the situation is halfway. The dominant weight of M lies on $|A'\rangle$, but more extended orbitals have no negligible weight as shown in Fig.4.9 (b), so that the former gives rise to the intensity of the 5.7 eV excitation, and the latter causes the transition to the 2 eV excitation, resulting somewhat broader spectra.

4.4.3 Excitation energy dependence of the 5.7 eV intensity

The disagreement with the experimental data in the Ω-scan of the 5.2 eV intensity with the impurity Anderson model is essentially cleared up by considering the above multi-Cu effects. Calculated Ω-scans of the 6 eV (actually 5.7 eV) intensity in $4p_\pi$-$1s$ RXES of Nd_2CuO_4 are given in Fig. 4.3 (b), where the results with $R_c = 1$ and 0.8 are represented with the dashed and thick solid curves, respectively.

In contrast to the doubly-peaked shape of the impurity model calculation, the multi-Cu one gives a triply-peaked structure. Because of the suppression effect for Ω tuned at around -3 eV, it reproduces the experimental data much better than the impurity one.

Introducing R_c, we see that the 5.7 eV intensity is more suppressed when Ω is tuned at the main peak (Z), but enhanced when Ω is tuned at the shoulder (M), improving the agreement with the experiment. TDOS and PDOS's with $R_c = 0.8$ for Cu_3O_{10} cluster is shown in Fig. 4.9 (b) with the dashed curve. We see that, first, ρ_{Z-} is enhanced by $R_c \neq 1$ at the lowest state "Z". This means that the hole is pushed out from the core

hole plaquette more strongly, so that the overlap with the intra-plaquette excitation tends to be decreased. On the other hand, $\rho_{A'}$ is increased around the energy of the shoulder "M", being consistent with the discussion in the subsection 4.3.4. However $\rho_{B'}$ and $\rho_{C'}$ are decreased at this energy, so that the overlap with the intra-plaquette excitation tends to be increased. This means that the existence of the ZR singlet state reduces extended nature of the state M.

We finally give a few comments on the present study. There is slight discrepancy with the experimental data mainly due to the incompleteness of the suppression effect. We have performed the calculations with relatively small clusters such as Cu_3O_{10} or Cu_5O_{16}. All excitations necessarily have more or less local character as far as the system is finite. Moreover, it is impossible to avoid boundary effects perfectly. In order to make the point clear, detailed experimental and theoretical analysis is needed for one-dimensional systems [136], where one can extend the cluster size without facing the limitation of the memory size of computers.

4.5 Conclusions

We theoretically investigated the Cu $4p_\pi$-$1s$ RXES of Nd_2CuO_4 firstly with the impurity Anderson model. Utilizing PDOS functions, we found that excitations about 5.2 eV above the ground state have considerably localized character, and that excitations about 2 eV above the ground state are nearly pure p states, having less amplitude at the plaquette with the impurity.

In the large cluster calculations, however, the low energy excitations created by CT processes have ZR singlet like character in contrast to the result with the impurity Anderson model, although excitations about 5.7 eV above the ground state is similarly local ("intra-plaquette"). This difference is clearly reflected in the RXES spectra when the main absorption peak is resonated.

A conspicuous disagreement with the experimental 6 eV intensity as a function of the incident photon energy could not be removed with the impurity Anderson model. It was demonstrated that the difficulty is solved by considering Zhang-Rice singlet formation, using the multi-Cu model.

We finally discussed the role of the configuration dependence of the d-p transfer. The satisfactory agreement with the experimental data is obtained with the large cluster calculation with R_c.

Chapter 5

Polarization and Momentum Dependence of Charge Transfer Excitations in Nd_2CuO_4

Polarization and momentum-transfer dependence in Cu $4p_\sigma$-$1s$ resonant X-ray emission spectra (RXES) of Nd_2CuO_4 is theoretically studied. We explain the experimental polarization and angular dependence of the 5.7 eV excitation. Comparing results calculated with single- and multi-Cu models, we confirm again the essential contribution of the nonlocal screening effect in Cu $4p_\sigma$-$1s$. We predict considerable dependence of a CT excitation at about 2 eV on momentum transfer along the CuO_2 planes, and the 5.7 eV excitation has less dependence. [1]

5.1 Introduction

As explained in § 1.1, RXES occupies a unique position in that it offers rich information on electronic structures in terms of both local and translational selection rules. With well-polarized X-rays created by synchrotron light sources, several groups have reported angular and polarization dependence of RXES in these days [71, 97, 106, 137, 138], and derived significant information on electronic structures. Since specific resonance enhancement occurs at the corresponding absorption peak in general, it is of great use also in that it may give clear explanation on the origin of somewhat complicated structure of XAS spectra such as Cu K-XAS of La_2CuO_4 [139].

Most of theoretical studies on polarization dependence of RXES in d and f electron systems within the framework of the second-order optical process have been based on impurity Anderson models so far. As well as the dipole transition, more complicated an-

[1] T. Idé and A. Kotani, submitted. A part of this chapter will be published also in Ref. [117].

gular and polarization dependence of quadrupolar transition is recently discussed within an impurity Anderson model [140]. The applicability of impurity Anderson models to angle or polarization resolved RXES is mathematically understood from Eq. (1.37), where the scattering amplitude of whole crystal is expressed as Fourier transformation of the local scattering amplitude $M_{\boldsymbol{\epsilon}'\boldsymbol{\epsilon}}(\boldsymbol{R};\Omega)$ of angular and polarization dependence. Here we explicitly write Ω-dependence of this amplitude defined in Eq. (1.39). As far as Cu $4p$-$1s$ RXES of Nd_2CuO_4 is concerned, however, it is also apparent from these equations that the impurity limit disregards, first, the nonlocal screening effect due to the Zhang-Rice singlet formation, and second, the momentum transfer ($\boldsymbol{q}$) dependence of RXES.

In this chapter, we discuss the polarization dependence in Cu $4p$-$1s$ RXES of Nd_2CuO_4 together with the latest experimental data. While definite polarization dependence of Cu K-XAS in this material has been already reported by a number of authors [141, 142, 143], little has been known about polarization dependence of RXES. Since a $1s$ orbital has no orbital degeneracy, theoretical analysis on polarization dependence is much simpler than that of, *e.g.*, $3d$-$2p$ transition [107]. Furthermore, the absence of apex oxygen in Nd_2CuO_4 and no overlap between $4p_\pi$ and $4p_\sigma$ absorption edges make the situation clearer. Thus, comparison with experimental data offers us a plain confirmation on the theoretical framework of RXES.

In the preceding chapter, we considered the nonlocal screening mechanism for the absence of resonance enhancement when the main Cu K-absorption peak is targeted by an incident X-ray. Detailed character on spatial direction of $4p$ orbitals was not used to interpret the Cu $4p$-$1s$ RXES spectra. Hence what the experimental data with differently polarized photon are successfully interpreted with the same theory is the ideal justification of the theory. At the same time, it is interesting to investigate whether the anisotropy in $4p$ orbitals affects the screening process in the valence electronic state. We will show that the polarization dependence in RXES can be clearly understood in terms of the framework of the second-order optical process. We will also show that Cu $4p_\sigma$-$1s$ spectra essentially follows $4p_\pi$-$1s$ spectra discussed in the preceding chapter.

The other point that the impurity limit disregards is the $\boldsymbol{q}$-dependence of RXES. Momentum resolved RXES with hard X-rays is a complement to angle-resolved PES to examine entire Brillouin zone. Recently, the $\boldsymbol{q}$-dependence of RXES is measured for Mott-Hubbard systems [144, 145] and insulating cuprates [135]. Despite of their significance, there have been few theoretical studies on the $\boldsymbol{q}$-dependence so far. Very recently, Tsutsui *et al.* reported a numerical calculation on the $\boldsymbol{q}$-dependence of Cu $4p$-$1s$ RXES for the fist time [82]. Based on an effective 4×4 Hubbard model, they discussed the energy dispersion of the CuO_2 planes of insulating cuprates. Within one-dimensional (1D) systems, we will show a model calculation on the $\boldsymbol{q}$-dependence of Cu

$4p$-$1s$ RXES of cuprates, and derive valuable information in the context of local and nonlocal excitations in Nd_2CuO_4.

The layout of this chapter is as follows. In the next section formulae for angular dependent transition operators are given. In § 5.3 we explain experimental polarization dependence with those formulae. In § 5.4 the role of the nonlocal screening effect is briefly described. In § 5.5 we discuss intra- and inter-plaquette natures of CT excitations from a viewpoint of $\boldsymbol{q}$-dependence of RXES. In the final section a brief summary is given.

5.2 Formulation

5.2.1 Hamiltonian

The model adopted in this chapter is the same as that of the preceding chapter except for terms describing $4p$ electrons. Calculated results are obtained with the multi-Cu (Cu_5O_{16}) model or the single-Cu (Cu_1O_{256}) model (impurity Anderson model). To discuss the polarization dependence, we introduce $4p_\sigma$ Hamiltonians, $H_{4p\sigma}$, H_{4pc} and H_{4p3d}. The one-electron part $H_{4p\sigma}$ is defined by

$$\begin{aligned} H_{4p\sigma} &= \varepsilon_{4p\sigma}\sum_{\boldsymbol{R}}\sum_{\eta=x,y} Q^\dagger_{\eta\boldsymbol{R}}Q_{\eta\boldsymbol{R}} + t_1\sum_{\boldsymbol{R}}\left[Q^\dagger_{x\boldsymbol{R}}Q_{x,\boldsymbol{R}+a\hat{x}} + Q^\dagger_{y\boldsymbol{R}}Q_{y,\boldsymbol{R}+a\hat{y}} + \text{H.c.}\right] \\ &+ t_2\sum_{\boldsymbol{R}}\left[Q^\dagger_{x\boldsymbol{R}}Q_{x,\boldsymbol{R}+a\hat{y}} + Q^\dagger_{y\boldsymbol{R}}Q_{y,\boldsymbol{R}+a\hat{x}} + \text{H.c.}\right], \end{aligned}$$

where $Q^\dagger_{\eta\boldsymbol{R}}$ creates a Cu $4p_\eta$ ($\eta = x, y$) *electron* at $\boldsymbol{R}$ site, $\hat{x}$ and $\hat{y}$ are two unit vectors along Cu-O direction in the CuO_2 plane. a is the Cu-O distance. t_1 and t_2 are respectively ($pp\sigma$) and ($pp\pi$) of the $4p_\sigma$ orbitals in terms of the Slater-Koster parameters [118].

H_{4pc} and H_{4p3d} describe Cu $4p$-$1s$ and Cu $4p$-$3d$ intra-atomic interactions, respectively. The explicit forms are

$$H_{4pc} = -\sum_{\boldsymbol{R}}\left[\sum_\eta U_{4pc}Q^\dagger_{\eta\boldsymbol{R}}Q_{\eta\boldsymbol{R}}\right]S_{\boldsymbol{R}}S^\dagger_{\boldsymbol{R}} \tag{5.1}$$

and

$$H_{4p3d} = -\sum_{\boldsymbol{R}}\left[\sum_\eta U_{4p3d}Q^\dagger_{\eta\boldsymbol{R}}Q_{\eta\boldsymbol{R}}\sum_\sigma d^\dagger_{\sigma\boldsymbol{R}}d_{\sigma\boldsymbol{R}}\right]. \tag{5.2}$$

These are the same as those of in the preceding chapter except for $\eta \neq z$ and the numerical value of U_{4p3d}. Now total Hamiltonian is written as

$$H = H_{dp} + H_{pp} + H_{\text{core}} + H_{dc} + H_{4p\sigma} + H_{4pc} + H_{4p3d},$$

where the first four terms have been defined in the preceding chapter. All parameters are the same as those of the preceding chapter except for $t_1 = 0.24$ and $t_2 = -0.8$, and

U_{4p3d}=3.3 eV. For the $4p$-$4p$ transfer energy parameters t_1 and t_2, we consider a first principle band calculation [121]. The difference between $U_{4p3d}(\sigma)$ and $U_{4p3d}(\pi)$ due to multipole contribution of the Slater integrals is estimated as 0.34 eV with Cowan's numerical program [146] and the empirical reduction factor 0.85 [26], from which we take the value 3.3 for $U_{4p3d}(\sigma)$.

5.2.2 Angular-dependent transition operators

The general form of the X-ray absorption and emission operators has been given in Eq. (1.22). For $1s$ excitation, it is appropriate for $4p$ operators to be expressed under the Cartesian coordinates, $(4p_x, 4p_y, 4p_z)$. The definition of the coordinates, whose origin is fixed to a Cu site, is described in Fig. 5.1. We set unit vectors along the x, y and z axes to be $\hat{e}_x$, $\hat{e}_y$ and $\hat{e}_z$. In the atomic approximation, we immediately have the $1s$-$4p$ absorption operator as

$$T^{\rm a}_{\boldsymbol{\epsilon}}(\boldsymbol{R}) = \boldsymbol{\epsilon}\cdot\sum_{\zeta=x,y,z}\hat{e}_\zeta Q^\dagger_{\zeta\boldsymbol{R}}S_{\boldsymbol{R}},$$

where we dropped a trivial prefactor.

Let us define another set of unit vectors, $\hat{x}_1$ and $\hat{y}_1$, which are parallel and perpendicular to the scattering plane, respectively. Both are perpendicular to the incident wave vector $\boldsymbol{q}_1$. Experimentally, it is convenient to express the polarization vector in terms of these unit vectors,

$$\boldsymbol{\epsilon} = \sum_{\alpha=\hat{x}_1,\hat{y}_1}\epsilon_\alpha\hat{\alpha}.$$

Hence we obtain

$$T^{\rm a}_{\boldsymbol{\epsilon}}(\boldsymbol{R}) = \sum_{\zeta,\alpha}\epsilon_\alpha(\hat{\alpha}\cdot\hat{e}_\zeta)Q^\dagger_{\zeta\boldsymbol{R}}S_{\boldsymbol{R}}. \tag{5.3}$$

While this formula explicitly assigns the $1s\rightarrow 4p$ transition path, one can easily generalize $T^{\rm a}_{\boldsymbol{\epsilon}}(\boldsymbol{R})$ for a $(l_c,m_c)\rightarrow(l,m)$ transition under the atomic dipole approximation. Rewriting $(nlm|\boldsymbol{\epsilon}\cdot\boldsymbol{p}|n_cl_cm_c)$ in terms of spherical tensor operators, we have

$$T^{\rm a}_{\boldsymbol{\epsilon}}(\boldsymbol{R}) = \sum_{m,q,\hat{\alpha},\sigma}(lm|C^{(1)}_q|l_cm_c)A^{(\hat{\alpha})}_q(\theta_i,\phi_i)l^\dagger_{\boldsymbol{R}m\sigma}c_{\boldsymbol{R}m_c\sigma}\epsilon_\alpha, \tag{5.4}$$

where dipole geometrical function $A^{(\hat{\alpha})}_q(\theta_i,\phi_i)$ is defined by

$$A^{(\hat{x}_1)}_q(\theta_i,\phi_i) = \begin{cases} -\frac{1}{\sqrt{2}}q\cos\theta_i\,{\rm e}^{-{\rm i}q\phi_i} & ,q=\pm1 \\ -\sin\theta_i & ,q=0 \end{cases} \tag{5.5}$$

$$A^{(\hat{y}_1)}_q(\theta_i,\phi_i) = \frac{\rm i}{\sqrt{2}}|q|{\rm e}^{-{\rm i}q\phi_i} \qquad ,q=0,\pm1. \tag{5.6}$$

Table 5.1: Angular dependent function $D^\zeta_{\beta\hat{\alpha}}(\theta,\theta_i,\phi_i)$.

$(\hat{\beta},\hat{\alpha})$	x	y	z
$(\hat{x}_2,\hat{x}_1)$	$\cos(\theta_i+\theta)\cos\theta_i\cos^2\phi_i$	$\cos(\theta_i+\theta)\cos\theta_i\sin^2\phi_i$	$\sin(\theta_i+\theta)\sin\theta_i$
$(\hat{y}_2,\hat{x}_1)$	$-\cos\theta_i\sin\phi_i\cos\phi_i$	$\cos\theta_i\sin\phi_i\cos\phi_i$	0
$(\hat{x}_2,\hat{y}_1)$	$-\cos(\theta_i+\theta)\cos\phi_i\sin\phi_i$	$\cos(\theta_i+\theta)\cos\phi_i\sin\phi_i$	0
$(\hat{y}_2,\hat{y}_1)$	$\sin^2\phi_i$	$\cos^2\phi_i$	0

θ_i and ϕ_i designates the direction of $\boldsymbol{q}_1$ (see Fig. 5.1) [110]. It is straightforward to derive the general formula for the X-ray emission due to the dipole transition, and therefore that for RXES. This matter is, however, beyond the scope of this chapter.

On the analogy of $T^{\rm a}_{\boldsymbol{\epsilon}}(\boldsymbol{R})$, the $4p$-$1s$ X-ray emission operator is given by

$$T^{\rm e}_{\boldsymbol{\epsilon}'}(\boldsymbol{R}) = \sum_\zeta\sum_{\beta=\hat{x}_2,\hat{y}_2}\epsilon'_\beta(\hat{\beta}\cdot\hat{e}_\zeta)S^\dagger_{\boldsymbol{R}}Q_{\zeta\boldsymbol{R}}, \tag{5.7}$$

where $\hat{x}_2$ and $\hat{y}_2$ are unit vectors parallel and perpendicular to the scattering plane, respectively, defined for the emitted wave vector $\boldsymbol{q}_2$ (see Fig. 5.1). Hence we obtain the transition operator of RXES at $\boldsymbol{R}$,

$$T_{\boldsymbol{\epsilon}'\boldsymbol{\epsilon}}(\boldsymbol{R};\Omega) = \sum_{\alpha,\beta,\zeta}\epsilon'_\beta D^\zeta_{\beta\hat{\alpha}}(\theta,\theta_i,\phi_i)\epsilon_\alpha S^\dagger_{\boldsymbol{R}}Q_{\zeta\boldsymbol{R}}G_0(\Omega)Q^\dagger_{\zeta\boldsymbol{R}}S_{\boldsymbol{R}}, \tag{5.8}$$

where $D^\zeta_{\beta\hat{\alpha}}(\theta,\theta_i,\phi_i)\equiv(\hat{\beta}\cdot\hat{e}_\zeta)(\hat{e}_\zeta\cdot\hat{\alpha})$ is tabulated in table 5.1. $G_0(\Omega)$ is the resolvent operator defined by $(\Omega+E_g-H+{\rm i}\Gamma)^{-1}$. We take Γ=0.8 eV as in the preceding chapter. Eventually, the overall operator of RXES is given by

$$T_{\boldsymbol{\epsilon}'\boldsymbol{\epsilon}}(\Omega) = \sum_{\boldsymbol{R}}{\rm e}^{{\rm i}\boldsymbol{q}\cdot\boldsymbol{R}}T_{\boldsymbol{\epsilon}'\boldsymbol{\epsilon}}(\boldsymbol{R};\Omega),$$

where $\boldsymbol{q}=\boldsymbol{q}_2-\boldsymbol{q}_1$ is the momentum-transfer of the X-ray.

5.3 Polarization Dependence

5.3.1 Experimental data

Experimental data were measured for a single crystal of Nd_2CuO_4 under two geometries depicted in Fig. 5.2. In the geometry (a), both polarization vectors, $\boldsymbol{\epsilon}$ and $\boldsymbol{\epsilon}'$, are parallel to the scattering plane, and they take 30° to the z-axis (so-called c-axis). In the geometry (b), both polarization vectors are perpendicular to the scattering plane, being parallel to the ab-plane. Note that momentum transfer vector is common to both geometries.

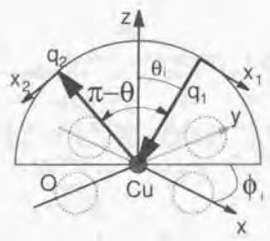

Figure 5.1: Geometrical configuration of RXES. The semicircle represents the scattering plane. The solid and open circles are Cu and O atoms, respectively. x and y axes are taken along two Cu-O directions. ϕ_i and θ_i designate the direction of the wave vector of the incident photon, $\boldsymbol{q}_1$. $\boldsymbol{q}_2$ is the wave vector of the emitted photon with a scattering angle θ. The polarization vector of the incident photon is described in terms of unit vectors $\hat{x}_1$ and $\hat{y}_1$. The former is parallel to the scattering plane, whereas the latter (not shown in the figure) is perpendicular to the scattering plane. These agree with each of the unit vectors of the x and y axes, respectively, in the limit ϕ_i, $\theta_i \to 0$. The polarization vector of the emitted photon is described with $\hat{x}_2$ and $\hat{y}_2$, which agree with $\hat{x}_1$ and $\hat{y}_1$, respectively, in the limit ϕ_i, θ_i and $\theta \to 0$.

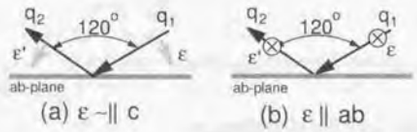

Figure 5.2: The experimental geometries. (a) Polarization vectors of the incident and emitted photons are parallel to the scattering plane ("$\boldsymbol{\epsilon} \sim \|c$"). (b) Polarization vectors of the incident and emitted photons are perpendicular to the scattering plane ("$\boldsymbol{\epsilon} \| ab$"). For both (a) and (b), the scattering angle is $\theta = 60°$, and the momentum transfer vector is perpendicular to the CuO_2 plane (so-called ab-plane).

The upper panel of Fig. 5.3 shows Cu K-XAS spectra for both geometries. We observe four distinct bumps from A to D for the geometry (a), which is denoted by "$\boldsymbol{\epsilon} \sim \|c$" in the figure, whereas only two structure C and D are observed for the geometry (b), which is denoted by "$\boldsymbol{\epsilon} \| ab$". The *first* question to be answered is this polarization dependence.

Analogous to Cu $4p_\pi$-1s RXES shown in Fig. 4.2, where the geometry (a) is adopted, a charge-transfer (CT) excitation is observed at about 5.7 eV energy loss also under the geometry (b). The Ω-dependence of the 5.7 eV intensity is plotted in the lower panel of Fig. 5.3 for both geometries. The experimental Ω-scan represented with the open circles is just the same data as in the lower panels in Fig. 4.3. As seen in the figure, strong resonance enhancement is observed only when Ω passes by the absorption peak B in the case of the geometry (a). On the other hand, strong enhancement occurs only when Ω passes by the absorption peak D in the case of the geometry (b). To confirm this, RXES spectra under the two geometries with Ω=$\Omega_{\rm B}$≡8990 eV (peak B) and $\Omega_{\rm D}$≡8999.5 eV (peak D) are shown in the lower and upper panels in Fig. 5.4, respectively. We see that an inelastic peak is observed at about 5.7 eV in both geometries. However, no enhancement occurs in the geometry (b) when Ω is tuned at B (lower panel). This is the *second* question. Conversely, no enhancement occurs in the geometry (a) when Ω is tuned at D (upper panel). This is the *third* question. Moreover, the maximum intensity of the 5.7 eV peak is considerably different in both cases. This is the *fourth* question.

5.3.2 Theoretical explanation

For theoretical description, we put an assumption, as the lowest nontrivial approximation, that difference between σ and π in U_{4pd}, U_{4pc} and 4p-4p transfers do not substantially change the valence states in the intermediate state. Let us first consider the angular dependence of K-XAS. We easily see from Eq. (5.3) that only $4p_\sigma$ absorption, i.e. excitation to a $4p_x$ or a $4p_y$ orbital, occurs when $\boldsymbol{\epsilon} = \hat{y}_1$ (the geometry (b)). This is the reason of the double-peak structure in the XAS spectrum in Fig. 5.3 (closed circles), and this fact certifies these peaks as a result of 1s-$4p_\sigma$ transition. When $\boldsymbol{\epsilon} = \hat{x}_1$, the formula immediately give the ratio of the absorption intensity as approximately

$$\sigma : \pi = \cos^2\theta_i : \sin^2\theta_i.$$

This result roughly explains the intensity ratio between the first and third features of the experimental XAS described in Fig. 5.3, where the ratio is found to be broadly consistent to $\sin^2 60° : \cos^2 60° = 3 : 1$ by considering a steeply increasing background spectrum. Now the first question has been answered.

The function $D^{\zeta}_{\beta\bar{\alpha}}$ rules angular dependence of RXES. When $(\boldsymbol{\epsilon}', \boldsymbol{\epsilon}) = (\hat{y}_2, \hat{y}_1)$ we see that there is no contribution of $4p_z$ ($4p_\pi$) orbitals because of $D^{z}_{\hat{y}_2,\hat{y}_1} = 0$. This fact

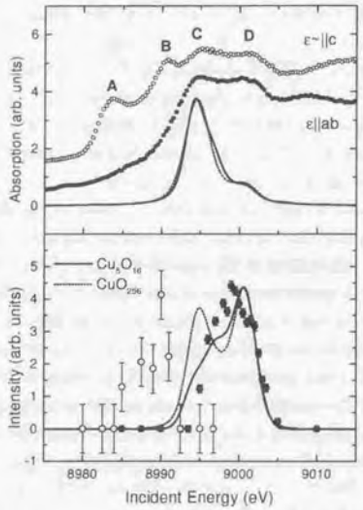

Figure 5.3: *Upper panel*: Cu K-XAS of Nd_2CuO_4 [117]. The open and closed circles represent experimental data under the geometries (a) and (b), respectively. The solid and dotted curves represent calculated Cu $1s \rightarrow 4p_\sigma$ absorption spectra under the geometry (b) with the multi-Cu and single-Cu models, respectively. Both curves are convoluted with Lorentzian $\Gamma_L = 0.8$ eV (HWHM) to consider lifetime of a $1s$ hole, and further convoluted with Gaussian $\Gamma_G = 0.8$ eV (HWHM) for the multi-Cu model, and with $\Gamma_G = 1.2$ eV (HWHM) for the single-Cu model to reproduce the experimental line width. *Lower panel*: the Ω-dependence of the 5.7 eV intensity [117]. The definition of the open and closed circles is the same as the upper panel. The solid and dotted curves represent the Ω-dependence of intensity of the 5.7 eV peak in Cu $4p_\sigma$-$1s$ RXES calculated under the geometry (b) with the multi-Cu and single-Cu models, respectively. Both curves are convoluted with $\Gamma_G = 1.10$ eV (HWHM) for the incident X-ray and with $\Gamma_G = 1.15$ eV (HWHM) for the emitted X-ray.

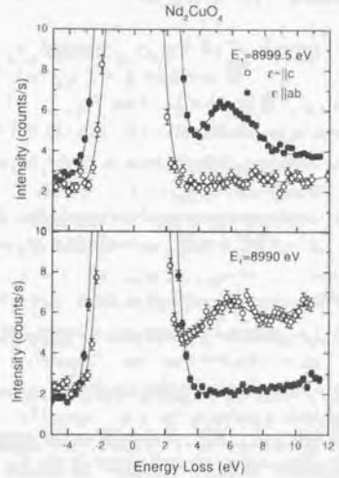

Figure 5.4: Experimental polarization dependence of Cu $4p$-$1s$ RXES [117]. The open and closed circles correspond to the geometries (a) and (b), respectively. In the upper panel Ω is tuned at the absorption peak D, and in the lower panel Ω is tuned at B. The definition of D and B are given in Fig. 5.3.

explains no enhancement over the $4p_\pi$ absorption threshold under the geometry (b). This is the answer to the second question.

Next we notice that $\hat{x}_1 \to \hat{y}_2$ and $\hat{y}_1 \to \hat{x}_2$ transitions are not allowed if the ground state $|g\rangle$ is not E representation of the D_{4h} group [2]. If it is the case,

$$\langle f|T_x(\Omega)|g\rangle = \langle f|T_y(\Omega)|g\rangle$$

follows for a final state $|f\rangle$ with the same symmetry as $|g\rangle$ because $T_x = C_4 T_y (C_4)^3$, C_4 being the rotation operator of $\pi/4$ around the z-axis at a Cu site $\boldsymbol{R}$. Here we defined $T_\zeta(\Omega)$ by

$$T_\zeta(\Omega) = \sum_{\boldsymbol{R}} e^{i\boldsymbol{q}\cdot\boldsymbol{R}} S^\dagger_{\boldsymbol{R}} Q_{\zeta\boldsymbol{R}} G_0(\Omega) Q^\dagger_{\zeta\boldsymbol{R}} S_{\boldsymbol{R}}$$

for $\zeta = x, y$ and z, with $\boldsymbol{q} \perp \boldsymbol{R}$ in this case. Thus $D^x_{\hat{y}_2\hat{x}_1} = -D^y_{\hat{y}_2\hat{x}_1}$ or $D^x_{\hat{x}_2\hat{y}_1} = -D^y_{\hat{x}_2\hat{y}_1}$ leads to the zero transition amplitude. Note that one can not suppress the elastic line by choosing $\boldsymbol{\epsilon}\cdot\boldsymbol{\epsilon}' = 0$ as far as $\boldsymbol{q} \perp \boldsymbol{R}$ holds, because elastic as well as inelastic scattering is not allowed in this case (see § 1.3.2).

Under the same assumption on the ground state, emission intensity under the geometry (b) is given as $I_2(\Omega) = |\langle f|T_x(\Omega)|g\rangle|^2$, and emission intensity under the geometry (a) as

$$I_1(\Omega) = |\langle f|T_x(\Omega)\cos(\theta_i+\theta)\cos\theta_i + T_z(\Omega)\sin(\theta_i+\theta)\sin\theta_i|g\rangle|^2 . \tag{5.9}$$

Thus we can estimate the intensity ratio between π- and σ-resonances under this geometry as

$$\sigma : \pi = \cos^2(\theta_i+\theta)\cos^2\theta_i : \sin^2(\theta_i+\theta)\sin^2\theta_i,$$

giving $\sigma : \pi = 1 : 9$ for $\theta_i = \theta = 60°$. This ratio partly answers the third question, i.e. the little resonance enhancement when Ω passes by the $4p_\sigma$ threshold under the geometry (a), although the relatively large error bars prevent us from further quantitative statement.

One can also roughly estimate the ratio of maximum intensity of the 5.7 eV peak for the two geometries. Since the maximum peak is realized at the $4p_\pi$ absorption threshold in the case of the geometry (a), we have $I_1 \sim \sin^2(\theta_i+\theta)\sin^2\theta_i |\langle f|T_z(\Omega_{\rm B})|g\rangle|^2$. If $|\langle f|T_z(\Omega_{\rm B})|g\rangle|$ can be regarded to be the same order as $|\langle f|T_x(\Omega_{\rm D})|g\rangle|$, the assumption that is exactly justified in the isotropic limit of $4p$ orbitals, we have the ratio as

$$I_1/I_2 \sim \sin^2(\theta_i+\theta)\sin^2\theta_i .$$

For $\theta_i = \theta = 60°$, this is approximately 0.56, which broadly explains the ratio of the 5.7 eV intensity in Fig. 5.4 (the answer to the fourth question).

[2] This assumption is numerically justified for undoped two-dimentional clusters, Cu_5O_{16} and Cu_4O_{12}.

We have studied Cu $4p$-$1s$ RXES under only the two geometries. Although the present calculation and experiment show no clear evidence that the assumption we put at the beginning of this subsection breaks down, it may be interesting to watch the angular and polarization dependence of RXES spectra in a class of materials. Ishihara and Maekawa recently emphasize the role of anisotropy between $U_{4p3d}(\pi)$ and $U_{4p3d}(\sigma)$ to explain anomalous elastic scattering in orbital ordered Mn compounds [147]. Analyzing angular and polarization dependence of also inelastic scattering, it is expected to obtain more detailed information on spatial direction of orbitals. This subject is left for the future study.

5.4 Incident Energy Dependence

5.4.1 Calculated results

We carried out numerical calculations for the geometry (b) again with the multi-Cu (Cu_5O_{16}) cluster and the single-Cu (Cu_1O_{256}) cluster models. Part of the results are shown in Fig. 5.3 with solid (multi-Cu) and dotted (single-Cu) curves for both panels. Corresponding to the experimental structures C and D in the XAS spectra, a doubly-peaked structure in the calculated absorption spectra is observed in the upper panel. For convolution width of the calculated spectra, see the figure caption. We hardly find discrepancy between the multi-Cu and single-Cu results, except for slight difference in the width of the main structure. The resonant behavior of the 5.7 eV peak shown in the lower panel is, however, quite different. The multi-Cu model presents a singly-peaked Ω-dependence, whereas the single-Cu model presents a doubly-peaked Ω-dependence. Note that somewhat larger convolution width of Gaussian $\Gamma_G = 1.1$ eV for the incident X-ray is used to reproduce the experimental resolution, as compared to Fig. 4.3. While the Ω-scan of the multi-Cu calculation reproduces much better than the single-Cu one, the experimental Ω-scan exhibits more definite suppression effect when Ω is tuned at the peak C.

To remove this discrepancy, we performed calculations including the reduction factor of the d-p transfer, R_c, whose definition has been given in the preceding chapter. Calculated XAS and RXES spectra with $R_c = 0.8$ are shown in Fig. 5.5. Despite the difference in the transition process, these figures are very similar to Figs. 4.8 and 4.10, where $R_c = 1$ calculations are given. The only remarkable difference is that the main absorption structure is more broadened than in Fig. 4.10. This result is consistent to the experimental difference in line width between the peak A (B) and C (D).

The Ω-scan of the 5.7 eV peak based on these improved calculations is plotted in the lower panel of Fig. 5.6. We see that agreement with the experimental data (closed circles) is considerably improved in the multi-Cu result (solid curve). Specifically,

the suppression effect when Ω is tuned at the main absorption peak is more clearly reproduced. While including R_c=0.8 also in the single-cluster case seems to give rise to more suppression as compared to that in Fig. 5.3, the overall line shape is still doubly-peaked, being utterly different from the experimental data.

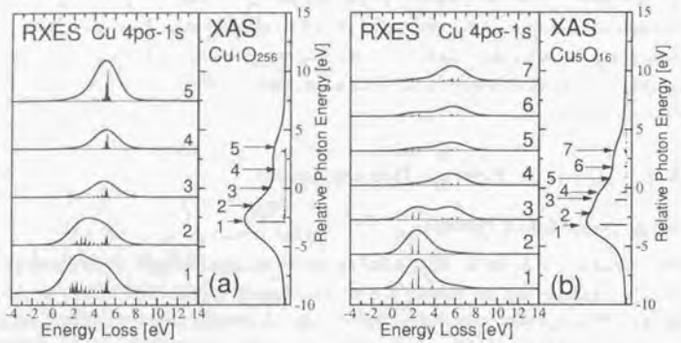

Figure 5.5: Cu K-XAS and $4p_\sigma$-$1s$ RXES with $R_c = 0.8$. (a) The impurity Anderson model (Cu_1O_{256} cluster). The XAS spectrum shown in the right panel is convoluted with Lorentzian $\Gamma_L = 0.8$ eV (HWHM) to consider lifetime of a $1s$ core hole, and further convoluted with Gaussian $\Gamma_G = 1.2$ eV (HWHM) to reproduce the experimental line width. The RXES spectrum shown in the left panel is also convoluted with $\Gamma_G = 1.15$ (HWHM) to reproduce the experimental resolution. (b) The multi-Cu model (Cu_5O_{16} cluster). The XAS spectrum shown in the right panel is convoluted with Lorentzian $\Gamma_L = 0.8$ eV (HWHM) to consider lifetime of a $1s$ core hole, and further convoluted with Gaussian $\Gamma_G = 0.8$ eV (HWHM) to reproduce the experimental line width. The RXES spectrum shown in the left panel is also convoluted with $\Gamma_G = 1.15$ (HWHM) to reproduce the experimental resolution. For (a) and (b), the elastic line, which should be located at zero, is omitted from the figure. The numbers attached to arrows in each XAS spectrum corresponds to those in RXES, representing the excitation energy.

5.4.2 Discussion

Because of the similarity between $4p_\pi$ and $4p_\sigma$ spectra, we naturally assign the main absorption peak calculated with the multi-Cu cluster to that state which has a Zhang-Rice (ZR) singlet at plaquettes neighboring to the photoexcited one. The shoulder (3 in Fig. 5.5 (b)) of the main structure is attributed to a well-screened $\underline{c}d^{10}\underline{L}$-like state, and

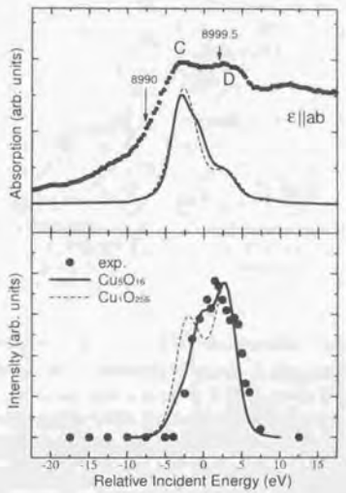

Figure 5.6: The improved calculations of Cu K-XAS and the Ω-scan of the 5.7 eV inelastic peak with $R_c = 0.8$. The closed circles represent again the experimental results measured under the geometry (b) for both panels. See the caption in Fig. 5.3.

the satellite peak (7 in Fig. 5.5 (b)) is attributed to a poorly-screened $\underline{c}d^9$-like state, where $\underline{c}$ and $\underline{L}$ represent core and ligand holes, respectively. The main and satellite absorption peaks in the single-Cu model are, on the other hand, mainly $\underline{c}d^{10}\underline{L}$ and $\underline{c}d^9$ states, respectively.

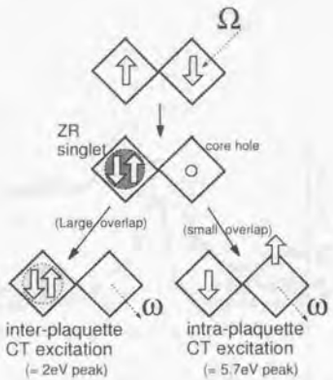

Figure 5.7: The essential contribution of the nonlocal screening effect in Cu 1s-4p-1s RXES when the incident photon energy Ω is tuned at the main peak of XAS.

Whichever model is used, there is a certain difference in spatial extent among these states, and this difference gives rise to the Ω-dependence of RXES spectra. As demonstrated in the preceding chapter, the ZR state has the most nonlocal character because a 3d hole is pushed out by the strong 1s-3d repulsive Coulomb interaction into neighboring plaquette, so that it has little overlap with intra-plaquette CT states. Although the 4p-3d correlation U_{4p3d} should more or less disturb the motion of the ZR singlet, it seems to act as only small perturbation. The final states are the same as those of $4p_\pi$-1s RXES because of the absence of 4p electron. As discussed, the 5.7 eV inelastic peak is a $d^{10}\underline{L}$-dominant anti-bonding state, and the 2 eV peak is attributed to an excitation of a 3d hole from the upper Hubbard band to the ZR singlet band.

The mechanism of the suppression effect of the 5.7 eV inelastic peak is summarized in Fig. 5.7. When Ω is tuned at the ZR intermediate state, the 5.7 eV final state is unfavorable because it is an intra-plaquette excitation. To the contrary, the 2 eV final state has large overlap with this intermediate state as suggested in the figure. The effect of R_c or detailed discussion on the Ω-dependence of RXES spectra substantially follows those in the preceding chapter, and we do not repeat it here.

5.5 Momentum Transfer Dependence

In the context of local and nonlocal excitations, it is interesting to measure the energy dispersion over k-space, because an excited state completely localized in a unit cluster should exhibit no energy dispersion. Figure 5.8 shows the experimental $\boldsymbol{q}$-dependence of RXES spectra [117], where $\boldsymbol{q}$ is taken perpendicular to the ab-planes. We find that there is no shift in the peak position. This result clearly suggests weak coupling between the CuO_2 layers.

The energy dispersion in a CuO_2 plane can be measured by sweeping the in-plane component of $\boldsymbol{q}$. We carried out numerical calculation on Cu 4p-1s RXES for a 1D periodic Cu_4O_{12} cluster for q=0, $\pi/2$ and π in the unit of $(2a)^{-1}$. The results are shown in Fig. 5.9, where we adopt the same parameter set as that in Fig. 5.5 (b) except for U_{dc}=8.0 [3]. Note that all core orbitals are taken into account here, whereas we have fixed a core hole to the central Cu site so far. Analogous to Figs.4.10 and 5.5 (b), the main absorption structure is composed of two peaks, and a satellite structure is observed about 7 eV distant from the main peak. Recent experimental and theoretical studies on high-resolution Cu 2p-XPS of various cuprates show that the nonlocally screening path gives rise to the main peak of Cu 2p-XPS in one-dimensional as well as two-dimensional cuprates, as far as the corner-shared structure is conserned [136, 148, 149, 150]. Although close inspection shows that each spectrum has slight difference according to difference in physical parameters and dimensionality, the character of the shoulder of the main peak or the satellite structure is also broadly common to both dimensions [151]. Hence we can utilize the calculated results to infer $\boldsymbol{q}$-dependence of the CT excitations in Nd_2CuO_4.

For the q-dependence of the RXES spectra, we find in Fig. 5.9 that the 2 eV peak exhibits considerable q-dependence in its intensity and position. Recently, Abbamonte *et al.* [135] successfully observed q-dependence of the 2 eV peak, which was hidden in the tale of the elastic line in Figs. 4.2, 5.4 and 5.8, in Cu 4p-1s RXES of a two-dimensional insulating cuprate, $Sr_2CuO_2Cl_2$. Moreover, their experimental data show that the CT structure at about 5 eV displays little q-dependence in its peak position [4]. This is qualitatively consistent to Fig. 5.9, and suggests the intra-plaquette nature of the 5.7 eV CT excited state in Nd_2CuO_4. On the contrary, the strong q-dependence of the 2 eV peak confirms the inter-plaquette (nonlocal) nature of the 2 eV CT excited state.

It is interesting to regard Fig. 5.9 as representing energy dispersion of a 1D system

[3] This value of U_{dc} is taken in order to keep the main-satellite separation in XAS spectrum the same as that in Fig. 5.5 (b).

[4] They assign the 5 eV structure to a "shakeup" scattering. However, it has been established from the analysis in the preceding chapter that this is the $d^{10}\underline{L}$-dominant anti-bonding state.

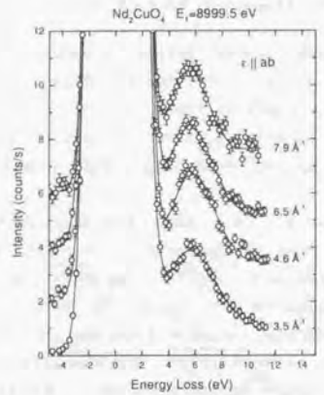

Figure 5.8: The experimental momentum transfer dependence when $\boldsymbol{q}$ is perpendicular to the CuO_2 planes [117]. The incident energy Ω is tuned at the D peak in the XAS spectrum.

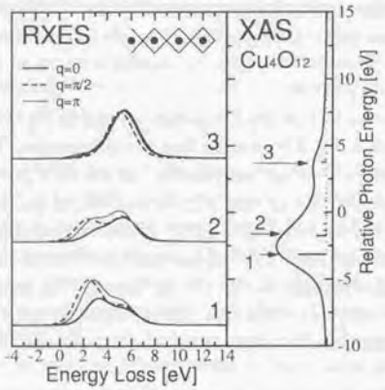

Figure 5.9: The q-dependence of Cu $4p_\sigma$-$1s$ REXS for a one-dimensional cluster as shown in the inset [152]. We see that the 2 eV CT excitation is strongly q-dependent, whereas the 5.7 eV peak has little q-dependence.

itself. Recently, angle-resolved PES measurements have been performed on (quasi) 1D cuprates, $SrCuO_2$ [153] and Sr_2CuO_3 [154], in the context of spin-charge separation [155, 156] due to photodoping. These experiments report that energy dispersion of a holon band, which is symmetric in each of halves of the first Brillouin zone ($k \geq 0$ or $k < 0$) with respect to the maximum at $|k|=\pi/2$, is much larger than that of $Sr_2CuO_2Cl_2$ [157]. Furthermore, they report that there is a spinon band over $-\pi/2 < k \leq \pi/2$ with smaller band width. While it has been established that the ZR singlet formation due to the "potential doping" (see § 1.4) in the intermediate state strongly contributes to Cu $4p$-$1s$ RXES spectra, the relation with these phenomena unique to 1D systems is unclear. This is a subject left in the future.

5.6 Conclusions

We have studied the polarization dependence of charge transfer excitations in Cu $4p$-$1s$ RXES of Nd_2CuO_4. Starting from the general formula introduced in Chap. 1, we derived a closed expression on angular and polarization dependence of RXES. The experimental polarization dependence is successfully explained with the formula, and the fact that the incident polarization dependence of the excitation process may be exploited to select the intermediate state of the resonance is shown.

Next, we confirmed the mechanism of the suppression of resonant inelastic scattering for nonlocally screened intermediate states. The difference between $4p_\pi$ and $4p_\sigma$ gave no drastic change in XAS and RXES spectra. Finally, we examined the q-dependence of the CT excitations in RXES spectra. The calculated spectra showed, first, that the 5.7 eV peak displays little q-dependence, and second, that the 2 eV peak considerably depends on q. These are interpreted in terms of intra- and inter-plaquette natures of the excitations, and are regarded as further support of the explanation of the suppression effect.

Chapter 6

Concluding Remarks

We have studied nonlocal effects in RXES with periodic Anderson models. The principal conclusions are twofold. First, the origin of the interplay between fluorescence-like and Raman components has been clarified. Second, the essential contribution of the nonlocal screening effect on Cu $4p$-$1s$ RXES spectra has been demonstrated. We recapitulate the conclusions of this thesis in what follows.

In Chap. 2, we studied the role of the translational symmetry on metal $3d$-$2p$ RXES of d^0 systems. The model used is a one-dimensional nondegenerate periodic Anderson model, which is a minimal model having explicit translational symmetry. It was shown that RXES depends more sensitively on the cluster size than XAS and XPS, so that RXES is a useful probe in studying the duality between itinerant and localized characters of $3d$ electrons. From results calculated by changing the cluster size, we proposed the NXES-like mechanism for the appearance of the fluorescence-like RXES spectra. It is summarized in Fig. 3.1. The essential point of our picture is the existence of extended states against the strong core hole potential in the intermediate state, although such extended states may have negligible weight in the XAS spectrum.

Regarding the $3d$ orbitals as Ce $4f$ ones, it was also explained why the experimental Ce $4f$-$3d$ RXES of CeO_2 is well reproduced by calculations with a single-cation impurity Anderson model.

In Chap. 3, the theory in the preceding chapter was extended to include explicit orbital degeneracy. We devised a doubly-degenerate one-dimensional model which contains two kinds of local point group symmetry, and associated them with e_g and t_{2g} orbitals in a crystal of O_h symmetry. First we study $3d$-$2p$ RXES spectra for d^0 systems. Within the single-metal-ion model, we mathematically defined antibonding and nonbonding states by utilizing the local point group symmetry or the permutation symmetry between the degenerate orbitals, and successfully explained the experimental polarization dependence of Ti $3d$-$2p$ RXES of TiO_2. In going from the single-metal-

ion model to multi-metal-ion model, the fluorescence-like component comes arise, and the calculated spectra clearly exhibit the interplay between the fluorescence-like and Raman components.

Next we showed calculated results for d^1 systems. The calculated RXES spectra displayed inelastic structures due to inter- or intra-site d-d excitation as well as nonbonding, antibonding and fluorescence-like structures. We found that the energy separation of the inelastic peaks due to the intra-site d-d excitation from the inelastic line considerably depends on cluster size. The polarization dependence similar to the d^0 system was predicted. The orbital degeneracy as well as the translational symmetry is essential to the appearance of the fluorescence-like spectra.

In Chap. 4, we theoretically investigated the Cu $4p_\pi$-$1s$ RXES of Nd_2CuO_4 with impurity Anderson and large-cluster models. While the former model failed to reproduce the experimentally observed suppression effect of resonance enhancement of the 5.7 eV inelastic peak, we obtained satisfactory agreement with the experimental data by using the large-cluster model. Utilizing PDOS functions, we found that the 2 eV structure is interpreted as an "inter-plaquette" excitation of a hole from a Cu site to other plaquettes to form a Zhang-Rice singlet, whereas the 5.7 eV excitation is attributed to the "intra-plaquette" CT excitation. This difference is clearly reflected on the excitation dependence of RXES spectra. The physical picture of the suppression effect is summarized in Fig. 5.7, which elucidates the essential contribution of the nonlocal screening effect on RXES.

In Chap. 5, first we studied the polarization dependence of charge transfer excitations in Cu $4p$-$1s$ RXES of Nd_2CuO_4. With a closed expression on angular and polarization dependence of RXES, the experimental polarization dependence is successfully explained. The calculated XAS and RXES spectra involving $4p_\sigma$ orbitals substantially followed those of the $4p_\pi$. We next examine the q-dependence of $4p_\sigma$-$1s$ RXES spectra. The calculated spectra show, first, that the 5.7 eV peak displays little q-dependence, and second, that the 2 eV peak considerably depends on q. These are interpreted in terms of intra- and inter-plaquette natures of the excitations, and are consistent to the interpretation in the preceding chapter.

To complete the investigation, some problems are left for us. First, for the NXES-like mechanism, we need to extend more the cluster size to obtain results that are more conclusive, and need to clarify the limitation and applicability of the present effective one-dimensional model. This is interesting also as a subject to examine new numerical algorithms such as DMRG. Within the exact diagonalization method, it is extremely difficult to demonstrate the NXES-like mechanism for realistic three-dimensional, possibly degenerate, models. However, one-dimensional systems themselves have attracted much attention in the context of spin-charge separation [153, 158]. It interesting to

study what kind of role RXES plays in such systems.

For cuprates, RXES would give significant information also in doped systems because RXES sensitively reflects electron dynamics associated with relaxation process due to a core hole creation. In fact, our (unpublished) calculation predicts considerable doping dependence of Cu $4p$-$1s$ RXES. Together with angle- or momentum-resolved RXES, detailed experimental and theoretical studies are left for the future problem. In this regard, one may investigate the network dependence in various cuprates.

We have obtained in Chap. 5 a negative answer to whether the anisotropy of $4p$ orbitals gives observable effects on the valence electronic system. It is of considerable interest to examine orbital ordering with angular- and polarization-resolved RXES.

Bibliography

[1] J. Hendry, *The Creation of Quantum Mechanics and the Bohr-Pauli Dialogue*, Kluwer Academic Publishers, Dordrecht, The Netherlands, 1984.

[2] G. Hertzberg, *Atomic Spectra and Atomic Structure*, Dover Publications, 1944.

[3] J. C. Slater, Phys. Rev. **34** (1929) 1293.

[4] G. Racah, Phys. Rev. **61** (1942) 186; **62** (1942) 438; **63** (1943) 367.

[5] K. Siegbahn, C. Nordling, A. Fahlman, R. Nordling, K. Hamrin, J. Hedman, G. Johansson, T. Bergmark, S.-E. Karlsson, I. Lindgren, and B. Lindberg, *Nova Acta Reg. Soc. Sci. Ups.*, **20** (1967) 1.

[6] S. Hüfner, *Photoelectron Spectroscopy*, Springer, 1994, Chap. 1.

[7] M. R. Norman, M. Randeria, H. Ding, and J. C. Campuzano, Phys. Rev. B **59** (1999) 11191-11192.

[8] G. Materlik, C. J. Sparks, and K. Fisher, ed., *Resonant Anomalous X-Ray Scattering*, North-Holland, 1994.

[9] D. Pines and P. Nozières, *The Theory of Quantum Liquid*, Addison Wesley, 1966.

[10] P. W. Anderson, Phys. Rev. **124** (1961) 41.

[11] J. R. Schrieffer and P. A. Wolff, Phys. Rev. **149** (1966) 491.

[12] J. Kondo, Prog. Theor. Phys. **32** (1964) 37.

[13] K. Ohtaka and Y. Tanabe, Rev. Mod. Phys. **62** (1990) 929.

[14] P. Nozières and C. T. de Dominicis, Phys. Rev. **178** (1969) 1097.

[15] G. D. Mahan, *Many-Particle Physics*, Plenum Press, New York, 1990, Chap. 8.

[16] A. Kotani and Y. Toyozawa, J. Phys. Soc. Jpn. **35** (1973) 1073; **35** (1973) 1082.

[17] A. Kotani and Y. Toyozawa, J. Phys. Soc. Jpn. **37** (1974) 912.

[18] L. N. Oliveila and J. W. Wilkins, Phys. Rev. B **32** (1985) 696.

[19] T. Ogawa, A. Furusaki, and N. Nagaosa, Phys. Rev. Lett. **68** (1992) 3638.

[20] O. Gunnarson and K. Schönhammer, Phys. Rev. B **28** (1983) 4315.

[21] A. Fujimori and F. Minami, Phys. Rev. B **30** (1984) 957.

[22] J. Zaanen, G. A. Sawatzky, and J. W. Allen, Phys. Rev. Lett. **55** (1985) 418.

[23] Sir N. F. Mott, *Metal-Insulator Transitions*, Taylor & Francis, 1990.

[24] N. F. Mott, Proc. Phys. Soc. A **62** (1949) 416; Can. J. Phys. **34** (1956) 1356; Phil. Mag. **6** (1961) 287.

[25] J. Hubbard, Proc. Roy. Soc. A **276** (1963) 238; A **277** (1964) 237; A **281** (1964) 401.

[26] T. Uozumi, *Thesis*, Department of Physics, Faculty of Science, The Unversity of Tokyo, 1994 [*in Japanese*].

[27] T. Uozumi, A. Kotani, Y. Tezuka, S. Shin, K. Okada, R. Zimmermann, P. Steiner, and S. Hüfner, J. Electron Spectrosc. Relat. Phenom. **83** (1997) 9-20.

[28] A. E. Bocquet, T. Mizokawa, K. Morikawa, A. Fujimori, S. R. Barman, K. Maiti, D. D. Sarma, Y. Tokura, and M. Onoda, Phys. Rev. B **53** (1996) 1161-1170.

[29] J. B. Bednorz and K. A. Müller, Z. Phys. B **64** (1986) 189.

[30] J. Bardeen, L. N. Cooper, and J. R. Schriefer, Phys. Rev. **108** (1957) 1175.

[31] A. Fujimori, E. Takayama-Muromachi, Y. Uchida, and B. Okai, Phys. Rev. B **35** (1987) 8814-8817.

[32] For a review, see, E. Dagotto, Rev. Mod. Phys. **66** (1994) 763.

[33] See, for example, P. Kuiper, G. Kruizinga, J. Ghijsen, M. Grioni, P. J. W. Weijs, F. M. F. de Groot, G. A. Sawatzky, H. Verweij, L. F. Feiner, and H. Petersen, Phys. Rev. **38** (1988) 6483.

[34] D. D. Sarma, O. Strebel, C. T. Simmons, U. Neukirch, G. Kaindl, R. Hoppe, and H. P. Müller, Phys. Rev. B **37** (1988) 9784.

[35] A. Bianconi, M. De Santis, A. Di Cicco, A. M. Flank, A. Fontaine, P. Lagarde, H. Katayama-Yoshida, A. Kotani, and A. Marcelli, Phys. Rev. B **38** (1988) 7196.

[36] M. A. van Veenendaal and G. A. Sawatzky, Phys. Rev. B **50** (1994) 11326-11331.

[37] P. W. Anderson, Phys. Rev. **115** (1959) 2.

[38] J. Zaanen and G. A. Sawatzky, Can. J. Phys. **65** (1987) 1262.

[39] D. Alders, J. Vogel, C. Levelut, S. D. Peacor, T. Hibma, M. Sacchi, L. H. Tjeng, C. T. Chen, G. van der Laan, B. T. Thole, and G. A. Sawatzky, Europhys. Lett. **32** (1995) 259-265.

[40] M. A. van Veenendaal, D. Alders, and G. A. Sawatzky, Phys. Rev. B **51** (1995) 13966-13971.

[41] M. van Veenendaal and G. A. Sawatzky, Phys. Rev. Lett. **70** (1993) 2459.

[42] St. Uhlenbrock, Chr. Scharfschwerdt, M. Neumann, G. Illing, and H.-J. Freund, J. Phys. C **4** (1992) 7973.

[43] F. C. Zhang and T. M. Rice, Phys. Rev. B **37** (1988) 3578.

[44] A. Tanaka and T. Jo, J. Phys. Soc. Jpn. **65** (1996) 912.

[45] M. Imada, A. Fujimori, and Y. Tokura, Rev. Mod. Phys. **70** (1998) 1039-1264.

[46] Y. Tezuka, S. Shin, A. Agui, M. Fujisawa, and T. Ishii, J. Phys. Soc. Jpn. **65** (1996) 312.

[47] S. M. Butorin, J. -H. Guo, M. Magnuson, and J. Nordgren, Phys. Rev. B **55** (1997) 4242.

[48] S. M. Butorin, J. -H. Guo, M. Magnuson, P. Kuiper, and J. Nordgren, Phys. Rev. B **54** (1997) 4405.

[49] K. Okada and A. Kotani, J. Electron Spectrosc. Relat. Phenom. **62** (1993) 131.

[50] J. J. Sakurai, *Advanced Quantum Mechanics*, Addison Wesley, 1967.

[51] H. Goldstein, *Classical Mechanis*, 2nd. ed., Addison-Wesley, 1980.

[52] H. Haken, *Quantum Field Theory of Solids*, North-Holland, 1976.

[53] N. L. Saini, A. Lanzara, A. Bianconi, and H. Oyanagi, Phys. Rev. B **58** (1998) 11768-11773.

[54] W. A. Caliebe, C.-C. Kao, J. B. Hastings, M. Taguchi, A. Kotani, T. Uozumi, and F. M. F. de Groot, Phys. Rev. B **58** (1998) 13452-13458.

[55] K. Hämäläinen, C.-C. Kao, J. B. Hastings, D. P. Siddons, L. E. Berman, V. Stojanoff, and S. P. Cramer, Phys. Rev. B **46** (1992) 14274-14277.

[56] B. A. Lippmann and J. Swhinger, Phys. Rev. **79** (1950) 469-480.

[57] J. J. Sakurai, *Modern Quantum Mechanics*, The Benjamin/Cummings Publishing Company, Inc., 1985.

[58] S. Sunakawa, *Sanran no Ryoushi-Ron* (Quantum Theory of Scattering), Iwanami Shoten, 1976 [*in Japanese*].

[59] R. D. Mattuck, *A Guide to Feynman Diagrams in the Many-Body Problem*, Second ed., Dover Publications, 1992.

[60] A. L. Fetter and J. D. Walecka, *Quantum Theory of Many-Particle Systems*, McGraw-Hill, 1971.

[61] K. Okada, A. Kotani, H. Ogasawara, Y. Seino, and B. T. Thole, Phys. Rev. B **47** (1993) 6203-6206.

[62] H. Ogasawara, A. Kotani, and B. T. Thole, Phys. Rev. B **50** (1994) 12332-12341.

[63] Y. Ma, Phys. Rev. B **49** (1994) 5799.

[64] C. Kittel, *Introdution to Solid State Physics*, Sixth ed., John Willey & Sons, Inc., Chap. 2.

[65] See, for example, J. D. Jackson, *Classical Electrodynamics*, John Wiley & Sons, Second ed., Sec. 9.7.

[66] T. Inui, Y. Tanabe, and Y. Onodera, *Group Theory and Its Applications in Physics*, Springer-Verlag, 1996.

[67] IDÉ Tsuyoshi, *Master Thesis*, Department of Physics, Faculty of Science, The University of Tokyo, 1997 [*in Japanese*].

[68] J.Jiménez-Mier, J. van Ek, D. L. Ederer, T. A. Callcott, J. J. Jia, J. Carlisle, L. Terminello, A. Afsaw, and R. C. Perera, Phys. Rev. B **59** (1999) 2649.

[69] S. Tanaka and A. Kotani, J. Phys. Soc. Jpn. **62** (1993) 464.

[70] For reviews of theoretical attempts in early days, see, A. Kotani, Proceedings of the 9th International Conference on X-ray Absorption Fine Structure, Grenoble, 1996; S. Tanaka and A. Kotani, Kotai Butsuri (*Solid State Physics*), **30** (1995) 907 [*in Japanese*].

[71] P. Kuiper, J.-H. Guo, C. Säthe, L.-C. Duda, J. Nordgren, J. J. M. Pothuizen, F. M. F. de Groot, and G. A. Sawatzky, Phys. Rev. Lett. **80** (1998) 5204-5207.

[72] M. Suzuki ed.,*Quantum Monte Carlo Methods in Condensed Matter Physics*, World Scientific, Singapore, 1993.

[73] S. R. White, Phys. Rev. Lett. **69** (1992) 2963; Phys. Rev. B **48** (1993) 10345.

[74] For a review of so-called finite-T DMRG, see, N. Shibata and K. Ueda, J. Phys. Condens. Matter **11** (1999) R1-R30 [Erratum: **11** (1999) 4289-4290].

[75] T. D. Kühner and S. R. White, Phys. Rev. B **60** (1999) 335-343.

[76] A. Tanaka, J. Phys. Soc. Jpn. **68** (1999) 3493-3496.

[77] R. Barrett, M. Berry, T. F. Chan, J. Demmel, J. Donato, J. Dongarra, V. Eijkhout, R. Pozo, C. Romine, and H. van der Vorst, *Templates for the Solution of Linear Systems: Building Blocks for Iterative Methods*, Society for Industrial and Applied Mathematics, 1994, Sec. 4.3.

[78] T. Tohyama and S. Maekawa, Kotai Butsuri (*Solid State Physics*), **31** (1996) 607 [*in Japanese*].

[79] W. H. Press, B. P. Flannery, S. A. Teukolsky, and W. T. Vetterling, *Numerical Recipes*, Cambridge University Press, 1989, Chap. 11.

[80] J. J. Dongarra, I. S. Duff, D. C. Sorensen, H. A. van der Vorst, *Solving Linear Systems on Vector and Shared Memory Computers*, Society for Industrial and Applied Mathematics, 1991, Chap. 7.

[81] G. Fano, F. Ortolani, and A. Parola, Phys. Rev. B **46** (1992) 1048.

[82] K. Tsutsui, T. Tohyama, and S. Maekawa, Phys. Rev. Lett. **83** (1999) 3705.

[83] T. Idé and A. Kotani, J. Phys. Soc. Jpn. **67** (1998) 3621-3629; A. Kotani and T. Idé, J. Synchrotron Rad. **6** (1999) 308-309.

[84] T. Idé and A. Kotani, J. Phys. Soc. Jpn. **68** (1999) 3100-3109.

[85] See, for example, F. M. F. de Groot, J. Electron Spectrosc. Relat. Phenom. **67** (1994) 529.

[86] M. A. van Veenendaal, H. Eskes, and G. A. Sawatzky, Phys. Rev. B **47** (1993) 11462.

[87] M. van Veenendaal and G. A. Sawatzky, Phys. Rev. B **49** (1994) 3473.

[88] K. Okada and A. Kotani, Phys. Rev. B **52** (1995) 4794.

[89] J. A. Carlisle, Eric L. Shirley, E. A. Hudson, L. J. Terminello, T. A. Callcott, J. J. Jia, D. L. Ederer, R. C. C. Perera, and F. J. Himpsel, Phys. Rev. Lett. **74** (1995) 1234.

[90] J. -E. Rubensson, D. Mueller, R. Shuker, D. L. Ederer, C. H. Zhang, J. Jia, and T. A. Callcott, Phys. Rev. Lett. **64** (1990) 1047.

[91] Y. Ma, N. Wassdahl, P. Skytt, J. Guo, J. Nordgren, P. D. Johnson, J-E. Rubensson, T. Böske, W. Eberhardt, and S. D. Kevan, Phys. Rev. Lett. **69** (1992) 2598.

[92] M. van Veenendaal and P. Carra, Phys. Rev. Lett. **78** (1997) 2839.

[93] C. F. Hague, M. Tronc, F. M. F. de Groot, H. Ogasawara, A. Kotani, J. H. Guo, and C. Såthe, *Advanced Light Source Compendium of User Abstracts and Technical Reports*, 1997; C. F. Hague, M. Tronc, Y. Yanagida, A. Kotani, J. H. Guo, and C. Såthe, unpublished.

[94] M. Nakazawa, S. Tanaka, T. Uozumi, and A. Kotani, J. Phys. Soc. Jpn. **65** (1996) 2303.

[95] S. M. Butorin, D. C. Mancini, J. -H. Guo, N. Wassadahl, and J. Nordgren, J. Alloys Compounds, **225** (1995) 230.

[96] T. Jo and A. Kotani, J. Phys. Soc. Jpn. **55** (1986) 2457.

[97] F. M. F. de Groot, M. Nakazawa, A. Kotani, M. H. Krish, and F. Sette, Phys. Rev. B **56** (1997) 7285.

[98] K. E. Miyano, D. L. Ederer, T. A. Callcott, W. L. O'Brien, J. J. Jia, L. Zhou, Q. -Y. Dong, Y. Ma, J. C. Woicik, and D. R. Mueller, Phys. Rev. B **48** (1993) 1918.

[99] H. Tsunetsugu, M. Sigrist, and K. Ueda, Rev. Mod. Phys. **69** (1997) 809, Sec. I.

[100] R. J. Elliott, Phys. Rev. **108** (1957) 1384, and references therein.

[101] E. Wuilloud, B. Delley, W.-D. Schneider, and Y. Baer, Phys. Rev. Lett. **53** (1984) 202.

[102] T. Minami and K. Nasu, Phys. Rev. B **57** (1998) 12084; T. Minami and K. Nasu, J. Electron Spectrosc. Relat. Phenom. **92** (1998) 213-218.

[103] T. Minami, J. Phys. Soc. Jpn. **67** (1998) 3958; T. Minami and K. Nasu, J. Electron Spectrosc. Relat. Phenom. **92** (1998) 231-235.

[104] C. C. Kao, W. A. L. Caliebe, J. B. Hastings, and J. -M. Gillet, Phys. Rev. B **54** (1996) 16361.

[105] Y. Ma, P. Skytt, N. Wassdahl, P. Glans, D. C. Mancini, J. Guo, and J. Nordgren, Phys. Rev. Lett. **71** (1993) 3725.

[106] Y. Harada, M. Matsubara, A. Kotani, T. Kinugasa, R. Eguchi, and S. Shin, unpublished.

[107] M. Matsubara, T. Uozumi, A. Kotani, Y. Harada, and S. Shin, unpublished.

[108] Y. Tezuka *et al.*, private communication.

[109] T. Uozumi, K. Okada, A. Kotani, Y. Tezuka, and S. Shin, J. Phys. Soc. Jpn. **65** (1996) 1150.

[110] M. Taguchi, *Thesis*, Department of Physics, Faculty of Science, The University of Tokyo, 1998 [*in Japanese*].

[111] N. E. Bickers, Rev. Mod. Phys. **59** (1987) 845.

[112] G. van der Laan, Phys. Rev. B **41** (1990) 12366.

[113] T. Higuchi, T. Tsukamoto, M. Watanabe, M. M. Grush, T. A. Callcott, P. C. Perera, D. L. Ederer, Y. Tokura, Y. Harada, Y. Tezuka, and S. Shin, Phys. Rev. B **60** (1999) 7711.

[114] Y. Tokura, H. Takagi, and S. Uchida, Nature (London) **337** (1989) 345; H. Takagi, S. Uchida, and Y. Tokura, Phys. Rev. Lett. **62** (1989) 1197.

[115] R. J. Gooding, K. J. E. Vos, and P. W. Leung, Phys. Rev. B **50** (1994) 12866.

[116] J. P. Hill, C.-C. Kao, W. A. L. Caliebe, M. Matsubara, A. Kotani, J. L. Peng, and R. L. Greene, Phys. Rev. Lett. **80** (1998) 4967-4970.

[117] K. Hämäläinen, J. P. Hill, S. Huotari, C.-C. Kao, L. E. Berman, A. Kotani, T. Idé, J. L. Peng, and R. L. Greene, Phys. Rev. B. **61** (2000) 1836-1840.

[118] J. C. Slater and G. F. Koster, Phys. Rev. **94** (1954) 1498; Walter A. Harrison, *Electronic Structure and the Properties of Solids*, Dover Publications, 1989, p.481.

[119] Y. Ohta, T. Tohyama, and S. Maekawa, Phys. Rev. B **43** (1991) 2968.

[120] A. K. McMahan, R. M. Martin, and S. Satpathy, Phys. Rev. B **38** (1988) 6650.

[121] S. Matsuno and H. Kamimura, J. Superconductivity **7** (1994) 517.

[122] M. O. Krause and J. H. Oliver, J. Phys. Chem. Ref. Data, **8** (1979) 329.

[123] M. Taguchi, T. Uozumi, and A. Koatni, J. Phys. Soc. Jpn. **66** (1996) 247.

[124] Chap. 4 in Ref. [15].

[125] D. A. Shirley, Phys. Rev. B **12** (1972) 4709.

[126] S. Tougaard and P. Sigmund, Phys. Rev. B **25** (1982) 4452.

[127] S. Tanaka, K. Okada, and A. Kotani, J. Phys. Soc. Jpn. **60** (1991) 3893.

[128] O. Gunnarsson and O. Jepsen, Phys. Rev. B **38** (1988) 3568.

[129] J. H. Jefferson, H. Eskes, and L. F. Feiner, Phys. Rev. B **45** (1992) 7959.

[130] F. Parmigiani, L. Sangaletti, A. Goldnoi, U. del Pennino, C. Kim, Z.-X. Shen, A. Revcolevschi, and G. Dhalènne, Phys. Rev. B **55** (1997) 1459.

[131] Y. Mizuno, T. Tohyama, S. Maekawa, T. Osafune, N. Motoyama, H. Eisaki, and S. Uchida, Phys. Rev. B **57** (1998) 5326.

[132] Y. Tokura, S. Koshihara, T. Arima, H. Takagi, S. Ishibashi, T. Ido, and S. Uchida, Phys. Rev. B **41** (1990) 11657-11660.

[133] T. Tohyama and S. Maekawa, J. Phys. Soc. Jpn. **60** (1991) 53.

[134] K. Okada and A. Kotani, J. Phys. Soc. Jpn. **66** (1997) 341.

[135] P. Abbamonte, C. A. Burnes, D. D. Issacs, P. M. Platzman, L. L. Miller, S. W. Cheong, and M. V. Klein, Phys. Rev. Lett. **83** (1999) 860.

[136] K. Okada, A. Kotani, K. Maiti, and D. D. Sarma, J. Phys. Soc. Jpn. **65** (1996) 1844.

[137] M. Pompa, A. M. Flank, P. Lagarde, J. C. Rife, I. Stekhin, M. Nakazawa, H. Ogasawara, and A. Kotani, Phys. Rev. B **56** (1997) 2267-2272.

[138] L. C. Duda, G. Dräger, S. Tanaka, A. Kotani, J. Guo, D. Heumann, S. Bocharov, N. Wassdahl, and J. Nordgren, J. Phys. Soc. Jpn. **67** (1998) 416.

[139] H. Tolentino, M. Medarde, A. Fontaine, F. Baudelet, E. Dartyge, D. Guay, and G. Tourillon, Phys. Rev. B **45** (1992) 8091.

[140] M. Taguchi, J. C. Parlebas, T. Uozumi, A. Kotani, and C.-C. Kao, Phys. Rev. B **61** (2000) 2553-2560.

[141] Z. Tan, J. I. Budnick, C. E. Bouldin, J. C. Woicik, S-W. Cheong, A. S. Cooper, G. P. Espinosa, and Z. Fisk, Phys. Rev. B. **42** (1990) 1037.

[142] H. Oyanagi, Y. Yokoyama, H. Yamaguchi, Y. Kuwahara, T. Katayama, and Y. Nishihara, Phys. Rev. B **42** (1990) 10136.

[143] J. M. Tranquada, S. M. Heald, W. Kunnmann, A. R. Moodenbaugh, S. L. Qiu, Y. Xu, and P.K. Davies, Phys. Rev. B **44** (1991) 5176.

[144] E. D. Isaacs, P. M. Platzman, P. Metcalf, and J. M. Honig, Phys. Rev. Lett. **76** (1996) 4211.

[145] P. M. Platzman and E. D. Isaacs, Phys. Rev. B **57** (1998) 11107.

[146] R. D. Cowan, *The Theory of Atomic Structure and Spectra*, University of California Press, Berkeley, 1981. Cowan's code is now released in the World Wide Web, http://gluon.fi.uib.no/AMOS/COWAN/.

[147] S. Ishihara and S. Maekawa, Phys. Rev. B **58** (1998) 13442-13451.

[148] K. Okada and A. Kotani, Physica B: Condensed Matter, **237-238** (1997) 383-384.

[149] T. Böske, K. Maiti, O. Knauff, K. Ruck, M. S. Golden, G. Krabbes, J. Fink, T. Osafune, N. Motoyama, H. Eisaki, and S. Uchida, Phys. Rev. B **57** (1998) 138.

[150] K. Karlsson, O. Gunnarsson, and O. Jepsen, Phys. Rev. Lett. **82** (1999) 3528.

[151] K. Okada and A. Kotani, J. Electron Spectrosc. Relat. Phenom. **86** (1997) 119-126.

[152] T. Idé and A. Kotani, in preparation; Meeting abstracts of the Physical Society of Japan **54** (1999) Issue 1, Pt. 2, p. 191.

[153] C. Kim, A. Y. Matsuura, Z.-X. Shen, N. Motoyama, H. Eisaki, S. Uchida, T. Tohyama, and S. Maekawa, Phys. Rev. Lett. **77** (1996) 4054-4057; C. Kim, Z.-X. Shen, N. Motoyama, H. Eisaki, S. Uchida, T. Tohyama, and S. Maekawa, Phys. Rev. B **56** (1997) 15589-15595.

[154] H. Fujisawa, T. Yokoya, T. Takahashi, S. Miyasaka, M. Kibune, and H. Takagi, Solid State Commun. **106** (1998) 543; Phys. Rev. B **59** (1999) 7358-7361.

[155] S. Tomonaga, Prog. Theor. Phys. **5** (1950) 349.

[156] V. J. Emery, *Highly Conducting One-Dimensional Solids*, J. T. Devreese ed., Plenum Press, 1979, p.247ff.

[157] B. O. Wells, Z.-X. Shen, A. Matsuura, D. M. King, M. A. Kastner, M. Greven, and R. J. Birgeneau, Phys. Rev. Lett. **74** (1995) 964-967.

[158] H. Suzuura and N. Nagaosa, Phys. Rev. B **56** (1997) 3548.

Acknowledgements

The present thesis is a result of fruitful discussion with the supervisor Professor Akio Kotani. The author heartily thanks Prof. Kotani for careful reading the manuscript and for the relevant remarks.

The latest experimental data on RXES spectra of Ti oxides measured by Prof. S. Shin, Prof. Y. Tezuka and Mr. Y. Harada were indispensable for the theoretical investigation in Chaps. 2 and 3. The author would like to thank them for providing their experimental data prior to publications. The author also thanks Mr. M. Matsubara for valuable discussion on group theoretical aspects of the transition operator. Mr. Matsubara's theoretical results with an impurity Anderson model motivated the large-cluster calculations on Cu 4*p*-1*s* RXES of Nd_2CuO_4 in Chap. 4. The author owes the theoretical analysis in Chaps. 4 and 5 to the experimental data measured by Dr. J. P. Hill, Dr. C.-C. Kao and Dr. K. Hämäläinen. Useful discussions with Prof. K. Okada and Prof. S. Tanaka encouraged the present study.

論文の内容の要旨

第1章：序論

内殻準位に対する分光法は，物質科学における有用な研究手段として認知されている。内殻軌道は強く局在しているため，d または f 電子系に対しいわゆる不純物アンダーソン模型による解析が理論研究の主たる地位を占めてきたのは自然なことであった。しかしながら，1993年に van Veenendaal らが NiO の Ni 2p 光電子スペクトル（XPS）に強い「非局所遮蔽効果」を見出して以来，内殻準位分光スペクトルにおける非局所効果の寄与に，すなわち不純物模型では記述できない現象の寄与に興味が持たれている。

近年の高輝度光源の進歩によって共鳴 X 線発光分光法（RXES）の実験データがここ数年数多く報告されている。1996 年，手塚らは，TiO_2 の Ti 3d-2p RXES において，2 系統の異なった入射光エネルギー依存性を持つスペクトルの存在を報告した。ひとつは，わずかに入射光エネルギーにスペクトル形状が依存しつつ，入射光エネルギーが上がるにつれ，なめらかに非共鳴の X 線発光スペクトル（NXES）に移行する成分である。これを「蛍光成分」と名付ける。もうひとつは，入射光エネルギーに比例して射出 X 線のエネルギーが変化してゆく成分である。これを「ラマン成分」と名付ける。

RXES は他の分光法にない種々の特徴を持ち，今後の発展が期待される実験手法であるが，その基礎的理解はまだ十分ではない。とりわけ，多くの遷移金属酸化物で共通に観察される上記 2 成分の分離の起源については，何らの合意も形成されていない。また，van Veenendaal らの見出した非局所効果が RXES へ及ぼす寄与についても，それを実証した研究はいまだ存在していない。

本論文の動機の第一は，遷移金属酸化物における上記の特異な入射光エネルギー依存性の起源を理論的に解明することにある。第二は，光電子分光スペクトルの研究で発見された種類の非局所効果が，RXES のスペクトルにいかなる寄与をするか調べることである。第三は，RXES の偏光・角度依存性，および移行運動量依存性の理論的研究を通して，新実験手法としての RXES に理論的視座を与えることである。

第2章：RXES に対するクラスターサイズ依存性

d^0 電子配置の下，$(dp)^N$ 型の構造を持つ 1 次元の非縮退周期アンダーソン模型で X 線吸収スペクトル（XAS）および XPS，NXES，RXES の計算を行い，スペクトルの N 依存性を調べた。有効混成エネルギーにより軌道縮退が取り込まれていると考えれば，この模型は，並進対称性を備えた TiO_2 の有効模型のうち最も単純なものと見なせる。

TiO_2 を模した計算結果によれば，RXES の蛍光成分は，中間状態において，内殻から励起された電子が，内殻正孔のあるサイトからそれ以外のサイトに逃げ出すことで生じる。一旦内殻正孔の束縛から逃れれば，その後生ずる輻射遷移は必然的に NXES に似る。Ti 系に対する現実的なパラメターの範囲内では，3d 電子間，あるいは内殻と 3d 電子の間の強い相互作用が実験に見られる蛍光成分を説明するのに必要であることがわかった。

f^0 電子配置を持つ CeO_2 に対しては，不純物アンダーソン模型が，XAS，XPS に加え，RXES スペクトルもよく再現するという事実が知られている。パラメターを CeO_2 に対応したものに選び直すことにより，この模型で CeO_2 の RXES スペクトルについても議論した。その結果，TiO_2 に対応する計算結果と対照的に，並進対称性の結果はスペクトルに本質的な影響を与えないことが示された。

第3章：縮退のある d^0 および d^1 系におけるラマン成分と蛍光成分の共存

前章の模型では軌道縮退を無視したため，いわゆる非結合性の状態が原理的に存在せず，特に吸収の主ピークに入射光が共鳴した時に，実験と計算の対応がうまくつかないという憾みがあった。本章では局所的に二種類の対称性を持つ 2 重縮退周期的アンダーソン模型を提案し，RXES における軌道縮退と並進対称性の効果を議論した。

まず d^0 配置については，不純物模型の範囲内で，非結合性の状態がラマン成分を与えること，また，吸収の副ピークに共鳴した時には反結合性の状態が強く共鳴増大を起こすことが示された。大きなクラスターでは，これらに加えて蛍光成分がスペクトルに重なり，実験スペクトルに見える蛍光成分とラマン成分の共存が非常によく再現される。

d^1 配置を持つモット-ハバード型絶縁体については上記 3 種の構造のほか，原子内，および原子間の d-d 遷移がスペクトルに寄与する。電荷ギャップの由来の相違にかかわらず蛍光成分の存在が示されたことは，前章において提案した蛍光成分出現機構に支持を与える。本章の結果は，電子相関を正しく取りいれた模型に基づいて蛍光成分とラマン成分の共存を実証した初めての研究である。

第4章：Nd_2CuO_4 の Cu 4p-1s RXES における局所励起と非局所励起

高温超伝導体の母物質においては，Cu 2p-XPS の研究から，非ドープ系においても，Zhang-Rice 1 重項（ZRs）形成に由来するピークがスペクトルに強く現れることが示されている。Cu 4p(π)-1s RXES の中間状態においても，2p-XPS の終状態と同様な，強い内殻正孔ポテンシャルの効果による ZRs 形成が期待され，コヒーレントな二次光学過程を通して，その動態が RXES スペクトルに現れることが予想される。実験によれば，XAS の主ピークに入射光エネルギーをあわせた時，吸収強度の大きさにもかかわらず 5.7 eV 近傍の非弾性ピークが共鳴増大を示さない。むしろ吸収の副ピークにおいて強い共鳴増大が観察される。

この実験結果を説明するため，初めに不純物アンダーソン模型で Cu K-XAS および RXES を調べた。RXES スペクトルには，2 eV および 5.7 eV 近傍に非弾性散乱の構造が現れる。これらの強度は入射光エネルギーに依存して大きく変化する。その依存性は，中間状態および終状態の電荷移動励起の空間的広がりの大小を強く反映していることが示される。励起状態の空間的広がりは，ある種の部分状態密度を計算することで直接見ることができる。計算結果はおおむね実験を説明するものの，不純物模型によっては 5.7 eV ピークの入射光依存性について

の実験データを説明することができないことが確認された。

上記の結果と対比しつつ，大きなクラスター模型（Cu_5O_{16} クラスター）による計算結果を議論した。まず，不純物模型による結果と異なり，K 吸収端の主ピークが ZRs による構造であることが，部分状態密度計算により直接証明された。ZRs は本質的に非局所効果であるため，この吸収ピークに共鳴した時の RXES の終状態では，局所的電荷移動に伴う励起状態の強度が弱い。すなわち，実験で観測された 5.7 eV ピークの抑制効果は，中間状態における ZRs 形成の直接の帰結である。また計算によれば，吸収の主ピークに共鳴した時には 2 eV 近傍の非弾性ピークが強い共鳴増大を示すが，これは，電荷ギャップを与える状態が，ZRs バンドと上部ハバードバンドの間の電子正孔対生成と解釈できることを示唆する。以上の結果は，XPS の研究で見出された非局所遮蔽効果が，RXES においても顕著な効果を与えることを定量的に示した初めての研究である。さらに，強相関絶縁体の電荷ギャップの構造を調べる手段としての RXES の有用性を示したものと言える。

第 5 章：Nd_2CuO_4 の電荷移動励起における偏光および運動量依存性

RXES は系の局所的な対称性と並進対称性を同時にスペクトルに表現するという著しい特徴を持っている。RXES の偏光ないし角度依存性は前者に支配され，移行運動量依存性は後者に関係する。いずれも新世代の放射光光源を用いた新実験手法として興味が持たれる。

まず，コヒーレントな二次光学過程の式から RXES の偏光に依存する遷移演算子を導いた。1s 軌道は軌道縮退を持たないため，理論解析が極めて単純になる。これをもとに，最新の実験結果における Cu 4p-1s RXES の偏光依存性を解析的に検討した。実験によれば 5.7 eV 励起が最大の共鳴増大を示す入射光エネルギーが，偏光により約 10 eV も異なる。非弾性散乱の強度においてもかなりの違いが観測される。これらの顕著な偏光依存性は，遷移演算子の偏光依存性から数学的によく説明された。これは端的に二次光学過程としての RXES の定式化に支持を与えている。

次に再び不純物アンダーソン模型と Cu_5O_{16} クラスターを用いて RXES スペクトルの入射光依存性を調べた。中間状態における $4p\pi$ と $4p\sigma$ 電子の違いは，RXES の終状態には顕著な効果を及ぼさず，後者の RXES スペクトルの入射光エネルギー依存性は，基本的に前者を再現する。

最後に X 線の移行運動量（q）が Cu 4p-1s RXES スペクトルに与える影響について調べた。CuO_2 面同士の結合は弱いので，面に垂直な方向への q に対しては RXES スペクトルはほとんど依存しない。一方，1 次元のクラスター模型の範囲内で面内の q に対するスペクトルの変化を計算したところ，2 eV 付近の電荷移動励起には強い q 依存性があり，5.7 eV 付近の励起の q 依存性は弱いことが見出された。これから 2 eV 励起の遍歴的性格と，5.7 eV 励起の局在的性格が示唆される。この結果は，前章の電荷移動励起の空間的広がりに関する議論と一貫している。